

Editor-in-Chief B.E.Paton

Editorial board:

Yu. S. Borisov	V. F. Grabin
A. Ya. Ishchenko	V. F. Khorunov
B. V. Khitrovskaya	I. V. Krivtsun
S. I. Kuchuk	Yatsenko
Yu. N. Lankin	V. K. Lebedev
V. N. Lipodaev	L. M. Lobanov
V. I. Makhnenko	A. A. Mazur
O. K. Nazarenko	I. K. Pokhodnya
I. A. Ryabtsev	Yu. A. Sterenbogen
N. M. Voropai	K. A. Yushchenko
A. T. Zelnichenko	

International editorial council:

N. P. Alyoshin	(Russia)
U. Diltey	(Germany)
Guan Qiao	(China)
D. von Hofe	(Germany)
V. I. Lysak	(Russia)
N. I. Nikiforov	(Russia)
B. E. Paton	(Ukraine)
Ya. Pilarczyk	(Poland)
P. Seyffarth	(Germany)
G. A. Turichin	(Russia)
Zhang Yanmin	(China)
A. S. Zubchenko	(Russia)

Promotion group:

V. N. Lipodaev, V. I. Lokteva
A. T. Zelnichenko (exec. director)

Translators:

I. N. Kutianova, V. F. Orets,
T. K. Vasilenko, N. V. Yalanskaya

Editor

N. A. Dmitrieva
Electron galley:
I. S. Batasheva, T. Yu. Snegiryova

Address:

E.O. Paton Electric Welding Institute,
International Association «Welding»,
11, Bozhenko str., 03680, Kyiv, Ukraine
Tel.: (38044) 287 67 57
Fax: (38044) 528 04 86
E-mail: journal@paton.kiev.ua
http://www.nas.gov.ua/pwj

State Registration Certificate
KV 4790 of 09.01.2001

Subscriptions:

\$324, 12 issues per year,
postage and packaging included.
Back issues available.

All rights reserved.

This publication and each of the articles
contained herein are protected by copyright.
Permission to reproduce material contained in
this journal must be obtained in writing from
the Publisher.

Copies of individual articles may be obtained
from the Publisher.

CONTENTS

SCIENTIFIC AND TECHNICAL

Lobanov L.M., Pashchin N.A., Loginov V.P., Taranova T.G., Kostin V.A. and Chajka A.A. Influence of electrodynamic treatment on the features of fracture micromechanism of welded joints on aluminum alloy AMg6 2

Ishchenko A. Ya., Fedorchuk V.E., Poklyatsky A.G. and Yavorskaya M.R. Hot cracking resistance of Al-Zn-Mg-Cu system alloys in argon-arc welding 7

Labur T.M., Taranova T.G., Kostin V.A., Ishchenko A. Ya., Grigorenko G.M. and Chajka A.A. Nature of fracture of B96 alloy depending on heating conditions in welding 9

Kisilevsky F.N. and Dolinenko V.V. Mathematical modeling and development of MIG welding monitoring controller 16

Shvachko V.I. and Ignatenko A.V. Model of transportation of hydrogen with dislocations 24

Borisov Yu.S., Borisova A.L., Golnik V.F. and Ipatova Z.G. Corrosion resistance of thermal spray coatings of quasi-crystalline phase-containing AlCuFe base alloys 27

INDUSTRIAL

Rimsky S.T. Peculiarities of outflow of two gas flows from nozzles of welding torches in automatic consumable electrode welding 32

Kirian V.I., Kajdalov A.A., Novikova D.P., Bogajchuk I.L. and Kesners M. Improvement of welded joint structure under the impact of wideband ultrasonic vibrations during welding 38

Shonin V.A. and Nedej T.N. Strength properties of laser-arc butt welded joints in thin-sheet alloy AMg6 41

BRIEF INFORMATION

Chigarev V.V., Zarechensky D.A. and Belik A.G. Peculiarities of melting of flux-cored strips with exothermic mixtures contained in their filler 46

News 48

Ryzhov R.N. Influence of pulse electromagnetic actions on formation and solidification of welds 49

Thesis for a scientific degree 51

NEWS

Jubilee Conference «Welding days 2006» in Germany 52

Conference «Rapidly-quenched materials and coatings» 53

Our congratulations 55

Developed at PWI 45



INFLUENCE OF ELECTRODYNAMIC TREATMENT ON THE FEATURES OF FRACTURE MICROMECHANISM OF WELDED JOINTS ON ALUMINIUM ALLOY AMg6

L.M. LOBANOV, N.A. PASHCHIN, V.P. LOGINOV, T.G. TARANOVA, V.A. KOSTIN and A.A. CHAJKA

E.O. Paton Electric Welding Institute, NASU, Kiev, Ukraine

On the basis of fractographic analysis the peculiarities of the mechanisms of stressed state relaxation and microfracture of base metal samples and welded joints of AMg6 alloy were studied under the conditions of electrodynamic treatment (EDT) of the material by current pulses. It was determined that at EDT of butt welded joint HAZ the amount of the ductile fracture component increases. At the same time, a non-conservative plastic slip deformation is observed in the treated material that results in strain hardening of AMg6 alloy butt welded joint structure by 35–40 % compared with untreated material.

Keywords: electrodynamic treatment, aluminium alloys, welded joints, current pulses, stress-strain state, toughness, ductility, brittleness, microhardness, fractographic studies, fracture micromechanism, plastic deformations, slip planes, torsional slip

One of the promising ways to extend the service life of welded structures is treatment of weld metal and HAZ by current pulses of different duration and configuration, as well as impact of electromagnetic fields on structural materials [1]. One of the new methods of current impact on metals and alloys is electrodynamic treatment (EDT) based on initiation of electrodynamic forces in the materials arising at transient processes which accompany a current discharge passing in the material [2]. At summation of electrodynamic forces with external static loading applied to the welded structure, it may develop plastic deformations positively influencing the service life of the item.

The effectiveness of EDT of aluminium alloy welded joints was evaluated using the fractographic method of examination of the broken sample fractures [3]. Studying the fracture surface and description of their relief allows comparing the mechanisms of fracture of the material pre-treated by current pulses with those of the metal not treated by EDT.

The purpose of this work is investigation of the influence of EDT on the features of micromechanism of fracture of AMg6 aluminium alloy 4 mm thick and

its butt welded joints, which were treated under the conditions of single-step static loading of the material.

«Spade» type flat samples were treated in order to evaluate the influence of EDT on the change of material structure as a result of stimulation of the electrodynamic effect. When single current pulses were passed through the metal, a capacitor-type laboratory unit was used, the operating principle of which is described in [4]. Figure 1 gives the schematic of sample treatment. EDT was conducted both on the base metal (without the weld), preloaded by a longitudinal uniaxial tension in the region of elastic deformation, and on welded joints. Testing was conducted in a tensile-testing machine TsDM-10 with maximum tensile force of 10 t at deformation rate of 6 mm/min. A sample fastened in the testing machine grips was stretched up to the specified value and a discharge was applied with recording of the deforming force drop by an automatic recorder.

Characteristics of sample deformation resistance lowering were studied in the following EDT mode: electrode voltage U_{el} and current I_{el} were $U_{el} = 450$ V and $I_{el} = 3500$ A, respectively; duration of current impact $t_{pulse} = 0.5$ μ s; capacitance of capacitor bank $C_{cap} = 2800$ μ F.

Samples of butt joints from AMg6 alloy 4 mm thick, similar to those used for the base metal, were treated to evaluate the features of EDT of welded structures (see Figure 1). Prior to that, plates of $500 \times 250 \times 4$ mm size were welded in one pass by nonconsumable-electrode automatic argon-arc welding in ASTV-2M unit in the following mode: $U_w = 18$ V; $I_w = 220$ A, $v_w = 14$ m/h, filler material was SvAMg6 wire of 2.0 mm diameter.

Electronic fractography method was used to examine the fracture surfaces of materials treated by current pulses and of their welded joints on the microlevel. Fractographic evaluations were performed for fractures obtained at uniaxial tension to fracture of flat samples of the base metal and welded joints (see Figure 1) both those treated by series of successive

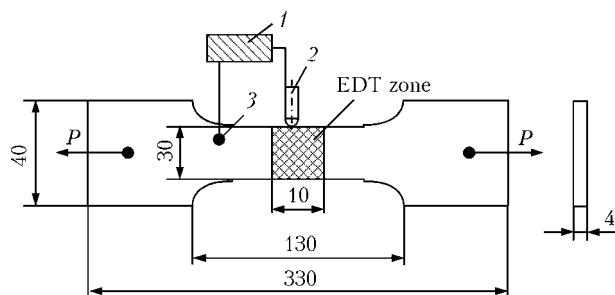


Figure 1. Schematic of EDT of samples for testing the base metal and welded joints by uniaxial tension: 1 — capacitor-type machine; 2 — electrode; 3 — fastening of the elements of electric circuit to the sample; P — tensile force



Tensile loading force on samples of AMg6 alloy base metal and welded joints at EDT

Material	n , discharge	σ_{pr} , MPa	σ_n , MPa	$\Delta\sigma_n$, MPa	$\Delta\sigma\%$, %	$\Sigma\Delta\sigma\%$, %
Base metal	–	116.7	–	–	–	~ 50
	1		88.34	28.36	24.3	
	2		77.5	10.84	9.3	
	3		70.0	7.5	6.43	
	4		62.9	7.1	6.1	
	5		59.5	3.4	3.0	
Welded joint	–	100.0	–	–	–	~ 57
	1		70.0	30.0	30.0	
	2		56.67	13.33	13.33	
	3		50.0	6.67	6.67	
	4		45.4	4.6	4.6	
	5		43.5	1.9	1.9	

Note. n --- sequence of discharges in the treatment cycle; σ_{pr} --- preliminary tensile stress in the sample; σ_n --- current value of tensile stresses after each current discharge; $\Delta\sigma_n = \sigma_n - \sigma_{n+1}$ --- current drop of tensile stresses after each discharge; $\Delta\sigma\% = (\Delta\sigma_n / \sigma_{pr}) \cdot 100\%$ --- current relative drop of tensile force after each discharge; $\Sigma\Delta\sigma\%$ --- total relative drop of tensile force after EDT cycle.

current pulses, and not subjected to EDT. Evaluation of the characteristic features of the relief allowed determination of the metal volume involved into plastic deformation to fracture stimulated by current pulses.

When studying the fracture fractograph, zones of plastic deformation localization in microvolumes of treated and untreated material were singled out, this predetermining the possibility of improvement of the metal structure toughness under the impact of electrodynamic forces.

Nature of the change of the loading force at tension of AMg6 alloy as a result of applying a series of sequential pulses is given in the Table. Analyzing the Table data leads to the conclusion that treatment of AMg6 alloy tensioned below the proportionality limit $\sigma_{p.1} = 130$ MPa, causes a drop of the elastic preloading force in the metal. Analyzed was $\Delta\sigma\%$ parameter (see the Table), which expresses the current change of the value of a unit jump of the deforming force at EDT in each test series. According to the given data, a regularity is observed, which indicates that at sample treatment the maximum drop of the tensile forces in the cycle (50 % of the total drop $\Sigma\Delta\sigma\%$) occurs at the first impact of current on the material. At the second and subsequent discharges a lowering of EDT effectiveness was observed, that, according to [5], is attributable to redistribution of the material dislocation structure at its loading.

Change of the loading mode of welded samples under the impact of EDT is shown in the Table. Here the value of the preliminary elastic force σ_{pr} (100 MPa) was selected to be close to the value of the maximum transverse component σ_y of residual welding stresses in alloys of Al-Mg system. Analysis of the tabulated data leads to the conclusion that the conditions of pre-loading of the welded joints are close to those accepted for the base metal. If we compare the tabulated values of $\Delta\sigma\%$ for the two types of samples, the relaxation processes associated with the drop of the preliminary deforming force, are more pronounced in the welded joints. Thus, $\Delta\sigma\%$ lowering

equal to the total value $\Sigma\Delta\sigma\%$ in base metal samples, is achieved in them during the first three current pulses. When comparing the $\Delta\sigma\%$ values in the base metal and the welded joint it is seen that they are higher in the latter (up to 10 %), which is, probably, associated with a higher ductility of the HAZ metal compared to the base metal, which is due to softening as a result of welding heating.

To study the influence of EDT on the change of the material structure, comparative evaluation was performed of the macrorelief topography of a fracture obtained as a result of uniaxial tension of the base metal of AMg6 alloy in the initial condition and with EDT application. Fractographs of the samples of treated and untreated material are given in Figure 2. It can be seen from the Figure that the fractures have a predominantly fibrous structure with coarse ridges formed in the mixed fracture mode [6]. Samples with one-sided treatment of the material were taken to study the alloy fracture relief after electrodynamic action. Compared to Figure 2, a, the fracture in Figure 2, b has a more pronounced fibrous structure with the depth of fibre penetration down to 2/3 of sample thickness from the treated side. The found features lead to the conclusion that EDT of AMg6 alloy provides a volume and not a surface impact on the material.

Microscopic evaluation of the fracture mechanism of AMg6 alloy in the initial condition is indicative of its transcrystalline nature. In this case, a pit-like structure of the fracture determined by shallow tear pits of an oval shape and mean diameter of 5–15 μm was observed across the entire thickness of the material. Unidirectional ridges of bridge tear and developed quasicleavage facets (zone B in Figure 2, c) of up to 2500–3000 μm^2 area are observed in the studied relief. Fracture topography is characterized by structural inhomogeneity, where the tear ridges alternate with cleavage fragments and pit sections. Pit relief and tear ridges are more pronounced at material fracture after treatment. Fractographic pattern of the middle part of sample fracture (zone B) was compared in the initial condition (Figure 2, c) and after EDT (Figure 2, d),

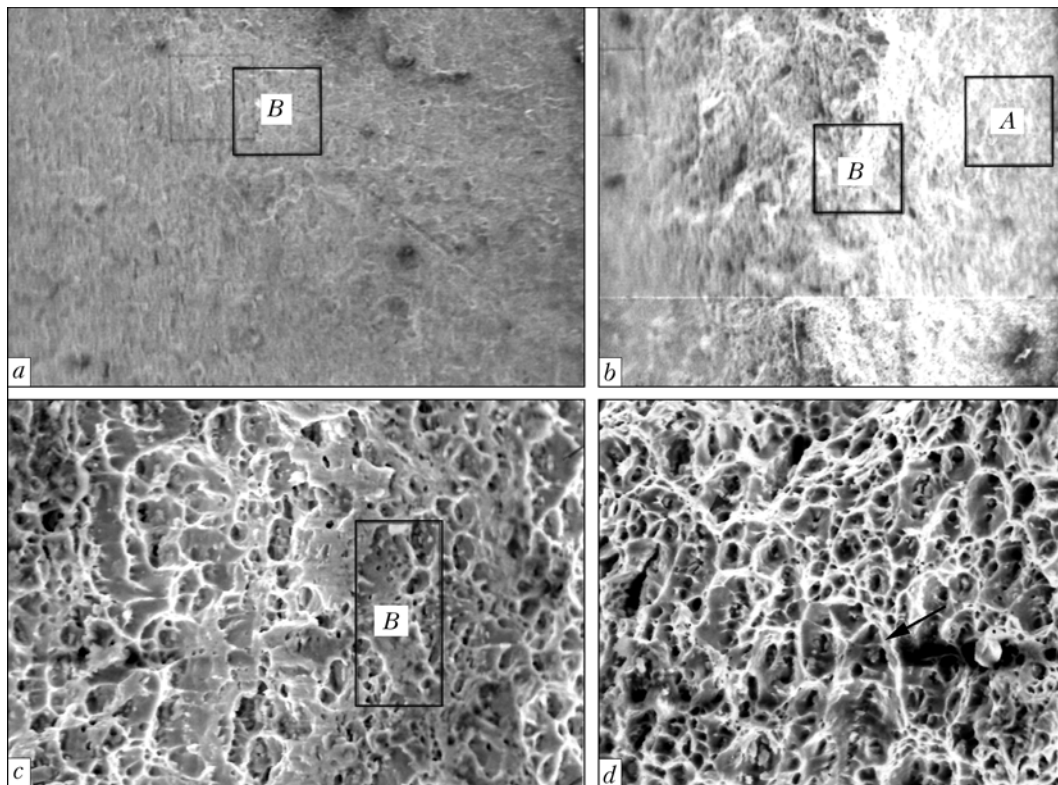


Figure 2. Appearance (*a, b*) and fractographic pattern (*c, d*) of fractures of AMg6 alloy: *a, c* — initial condition; *b, d* — after EDT; zone A — fracture section near sample surface; B — middle of fracture surface (*a, b* — $\times 33$; *c, d* — $\times 500$)

with a greater depth and equiaxiality of the pits being observed after EDT in the relief of AMg6 alloy fractures. While flat pits and ridges of one orientation are found on untreated metal, in fracture of samples after current impact quasicleavage facets are absent, and finer deep equiaxed pits of the average diameter of 5–10 μm and thick ridges of bridge tear of different orientation prevail (arrow in Figure 2, *d*). Average thickness of ridges in the initial material and after EDT is equal to 2 and 5 μm , respectively. Whereas in untreated AMg6 alloy the ridge lines are parallel to each other, after current impact mostly their perpendicularity to each other is observed. Analysis of the data in Figure 2 leads to the conclusion that EDT creates prerequisites for formation of volume zones of microtoughness in the material which increase the overall level of plastic deformations of the sample.

To determine the features of fracture micromechanism of Al–Mg aluminium alloy welded joints compared to the base metal, fractographic evaluation of the fractures of butt welds on AMg6 alloy treated (untreated) by current pulses was performed.

Welded samples of AMg6 alloy, which were made and subjected to one-sided EDT by the above procedure, were selected for investigations. Fractographs of butt joint fractures in the initial condition and after EDT are given in Figure 3. Fracture relief surface along the fusion line of untreated samples has a multi-site fracture structure (arrows in Figure 3, *a*), uniformly distributed over the entire fracture surface. Topography of the treated joint fracture is somewhat different with the fracture sites being concentrated in the subsurface region (zone A in Figure 3, *b*) from

the side of sample surface, exposed to current impact. Propagation occurs in parallel to the surface being treated (arrows in Figure 3, *b*). Such a relief, propagating in depth of the material up to 2/3 of sample thickness, similar to investigation of base metal fractures (see Figure 2, *b*), can be indicative of EDT impact through the material thickness.

Fracture relief of an untreated welded joint considered at a great magnification (Figure 3, *c*) is characterized by a fine-cellular structure with partially melted pits of normal tear, non-uniformly alternating with developed ridges of bridge tear and extended quasicleavage sections. Particularly pronounced is the non-uniformity of the structure of untreated sections at the welded sample surface, where the quasicleavage sections take up 70 % of fracture surface. Much more ordered is the fracture relief of the subsurface region of the HAZ metal (Figure 3, *b*, zone A) from the treated side, which is shown in Figure 3, *d*. It is characterized by quasicleavage facets of a short length and uniform distribution of uniaxial fine pits and ridges of tear, where the tear thickness does not exceed 5–10 μm . The structure of the fracture mid-surface is also close in terms of geometry (Figure 3, *b*, zone B), being the boundary of treatment impact characterized by «stringer» arrangement of the ridges.

On the whole it may be noted that after EDT the metal has a more developed surface of microtough fracture with a lower content of cleavage structures. Obtained results coincide with the opinion of the author of [5] in that by creating higher toughness areas in the metal, it is possible to control the ductility properties and, therefore, the processes of relaxation of its stress-strain state.

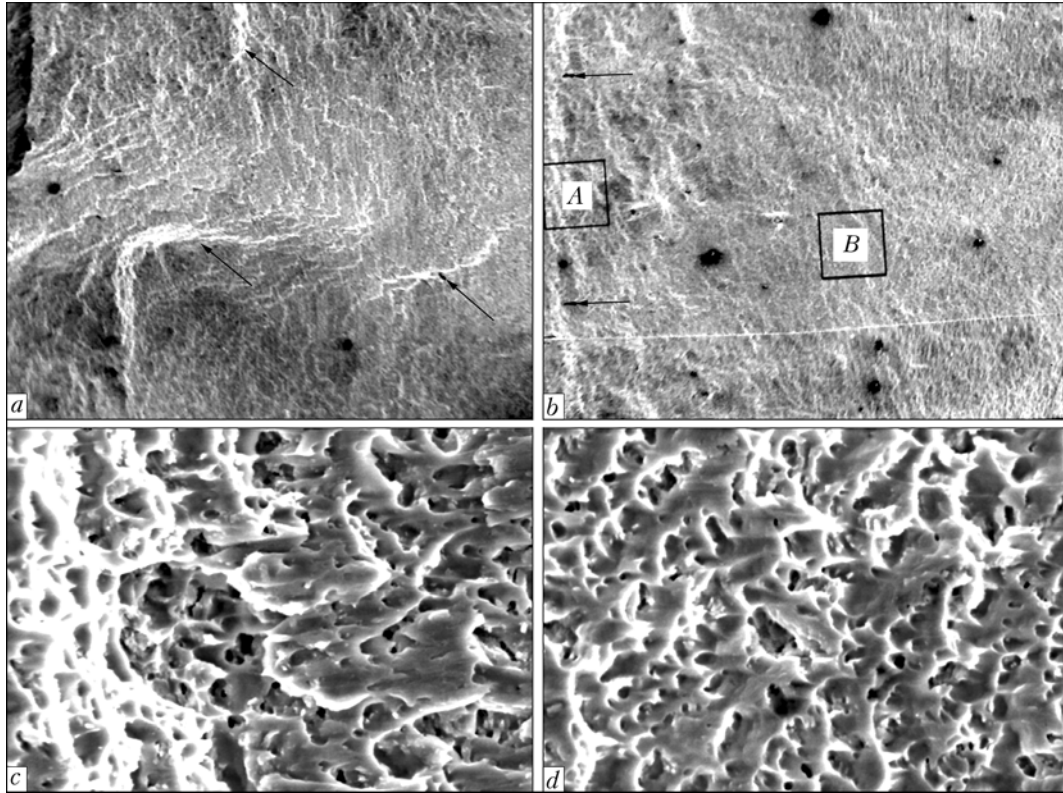


Figure 3. Appearance (a, b) and fractographic pattern (c, d) of fractures in welded joints of AMg6 alloy after sample fracture: a, c — without EDT; b, d — after EDT (a, b — $\times 18$; c, d — $\times 1000$)

The authors have conducted metallographic examination of the microstructure along the fusion line of AMg6 alloy welded joints treated and untreated by current pulses (Figure 4). Structure of the alloy untreated by current pulses mainly consists of dispersed precipitates of Al_3Mg_2 β -phase with MgSi magnesium

silicide fringe. β -phase has a large area and a lighter tint, surrounded by dark lines and point inclusions of magnesium silicide (Figure 4, a, b). The structure of the central zone of the treated alloy also has a similar composition (Figure 4, c).

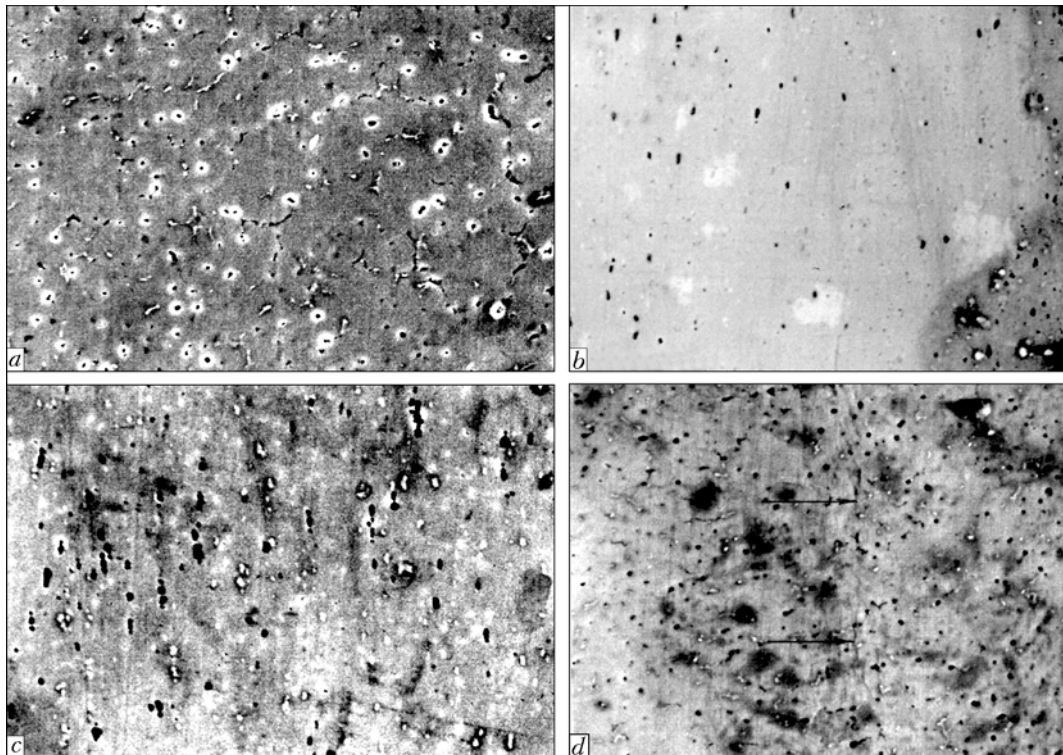


Figure 4. Microstructure of the HAZ of welded joint of AMg6 alloy made by argon-arc welding without EDT (a, b) and after EDT (c, d): a-c — central zone; b-d — zone near sample surface ($\times 500$)

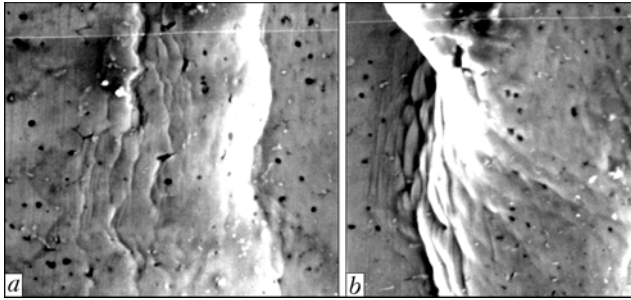


Figure 5. Microstructure of welded joints of AMg6 alloy after EDT: a --- plane slip; b --- torsional slip ($\times 1000$)

When studying the subsurface layer of AMg6 alloy after EDT (Figure 4, d) extended and developed groups of slip lines (arrows in Figure 4, d) were observed near the treated surface, which is indicative of volume plastic deformation of the material [7] at current pulse impact. Predominant orientation of the lines coincides with the plane of sample surface subjected to current impact. The sliding direction is the most favourably oriented relative to the plane of application of the external tensile load σ_{pr} . When comparing the macrostructure of the subsurface layer of the fracture of a treated welded joint of AMg6 alloy (arrows in Figure 3, b) with its microstructure (arrows in Figure 4, d) coincidence of the geometrical characteristics of the fracture and slip lines, is observed. When studying the slip mechanism at the subsurface layer of the treated welded joints at a greater magnification, it is seen (Figure 5) that the isolated slip lines (arrows in Figure 4, d) are combined into unidirectional groups (Figure 5, a) of slip lines. The observed configuration of the lines is indicative of the process of intensive plastic flow of the material at EDT. By the data of [7], such an effect is related to such processes as creating barriers for free propagation of plastic shear, influence of near-boundary volumes, intergranular structural stresses, as well as transition from sliding through one plane system to another.

When studying the slip lines, their configuration characteristic for a developed plastic flow was observed, namely slipping with torsional elements, when deformation of the polycrystalline structure runs along two and more directions. Torsion, by the data of [7], leads to considerable volume distortions of AMg6 alloy structure, which in this work is indicated by the nature of the relief variation directly at the treated surface. A plane slip type (Figure 6, a), torsional slip (Figure 6, b), as well as their superposition, were observed. The established features confirm the fact of intensive plastic flow in the subsurface layers of the material at its treatment by current pulses, which may lead to strain hardening. According to [7], this fact can be explained by that combined slipping leads to a complicated change of the crystal shape caused not only by shear, but also by superposition of the torsional component. This is accompanied by significant changes of the crystal inner structure related to shifting of the atomic planes.

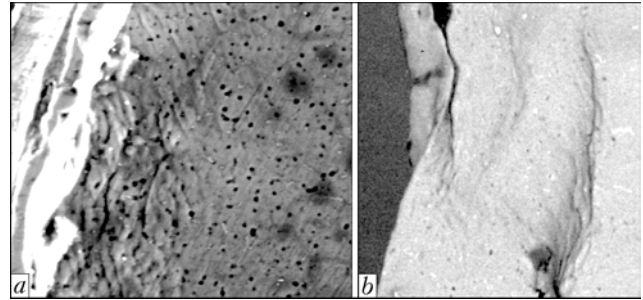


Figure 6. Microstructure of the surface of samples of AMg6 alloy welded joints after EDT: a --- plane slip; b --- torsional slip ($\times 1000$)

Increase of the density of distorted sections of the crystalline structure leads to strain hardening. To confirm its mechanism, *HV* microhardness was measured on sections of treated and untreated welded joints of AMg6 alloy. Measurements were conducted in the LECO instrument PMT-3 at 10 g load. *HV* values both for untreated material (see Figure 3, a), and for remote regions of the treated section (see Figure 3, b, zone B), were equal to *HV* 82.4. Maximum values of microhardness *HV* 129–131 were observed in the zone of the plane fracture site (see Figure 3, b, arrow in zone A), where torsional slip was found in addition to plane slip bands, and somewhat lower values of *HV* 119–121 were found directly at the treated surface (see Figure 4, d, right edge). Conducted measurements showed that treatment by current pulses of the HAZ of AMg6 alloy welded joint, causes strain hardening of the material by 35–40 % compared to the untreated one.

CONCLUSIONS

1. An experimental procedure was proposed for studying the mechanism of relaxation of the stress-strain state in rectangular samples of AMg6 alloy and its welded joints at electrodynamic impact on the material.
2. Based on fractographic investigations of fractures of AMg6 samples it was established that EDT increases the share of microtough fracture of the material manifested in increase of the area of pit structure and reduction of quasicleavage facets.
3. Based on metallographic examination of AMg6 alloy microsections, it was established that EDT creates local plastic flow zones in the material characterized by slip bands of different orientation, which results in strain hardening of the treated material by 35–40 %.

1. Lobanov, L.M., Pashchin, N.A., Loginov, V.P. (2005) Application of electric pulse treatment of structural elements to extend their service life (Review). *The Paton Welding J.*, **11**, 19–23.
2. Aleksandrov, G.N., Borisov, V.V., Ivanov, V.L. et al. (1985) *Theory of electric apparatuses*. Moscow: Vysshaya Shkola.
3. (1982) *Fractography and atlas of fractographs*: Refer. Book. Ed. by J. Fellouz. Moscow: Metallurgiya.
4. Lobanov, L.M., Pashchin, N.A., Skulsky, V.Yu. et al. (2006) Influence of electrodynamic treatment on the stress-strain state of heat-resistant steels. *The Paton Welding J.*, **5**, 8–11.
5. (1989) *Deformation and fracture mechanics of structural materials*. Ed. by R.V. Khartsberg. Moscow: Metallurgiya.
6. Kishkina, S.M., Bratashev, V.L., Guk, N.V. et al. (1988) *Fracture of aluminium alloys. Atlas of fractographs*. Moscow: VIAM.
7. Bernshtejn, M.L., Zajmovsky, V.A. (1978) *Mechanical properties of metals*. Moscow: Metallurgiya.



HOT CRACKING RESISTANCE OF Al-Zn-Mg-Cu SYSTEM ALLOYS IN ARGON-ARC WELDING

A.Ya. ISHCENKO, V.E. FEDORCHUK, A.G. POKLYATSKY and M.R. YAVORSKAYA
E.O. Paton Electric Welding Institute, NASU, Kiev, Ukraine

Resistance of high-strength alloys of Al-Zn-Mg-Cu system to high-temperature cracking in argon-arc welding was studied, depending on the total amount and ratio of the base alloying elements (zinc, magnesium, copper) in them, and also on the presence of scandium additives in the base and filler materials. It is shown that increase of the total amount of base alloying elements in the alloys and addition of 0.3 % Sc to the weld metal allow considerably increasing the hot cracking resistance of welded joints.

Keywords: argon-arc welding, high-strength aluminium alloys, alloying, scandium, weld metal, hot brittleness

In the wide range of aluminium alloys the highest strength alloys are of Al-Zn-Mg-Cu system. So, for instance, tensile strength σ_t of batch-produced alloy V96ts is equal to 650 MPa, and at the change of the proportion of the main alloying elements (zinc, magnesium, copper) and of their total content this value may reach 750 MPa [1], which allows widely using this alloy as structural material in different industries. Alloys of this system are characterized by a good adaptability to fabrication in manufacture of semi-finished products. However, it is rather difficult to use them for welded structure fabrication in view of their higher susceptibility to hot cracking in welding.

The work performed on improvement of weldability of alloys of Al-Zn-Mg ternary system by microalloying with scandium additives [2-4] showed the possibility of an essential improvement of the level of strength of the base and welded joint metal, and reducing their susceptibility to hot cracking in welding. As regards the alloys of Al-Zn-Mg-Cu system, the researchers are divided in their opinions on the rationality of their scandium alloying. Some of them [5] state that scandium alloying of high-copper alloys leads to formation of a complex compound --- W-phase ($Al_xCu_ySc_z$), as a result of which scandium cannot

participate in the solid solution strengthening or promote refining of the alloy structure. Therefore, further research is required for a more precise determination of scandium influence on weldability of high-alloyed aluminium alloys containing copper.

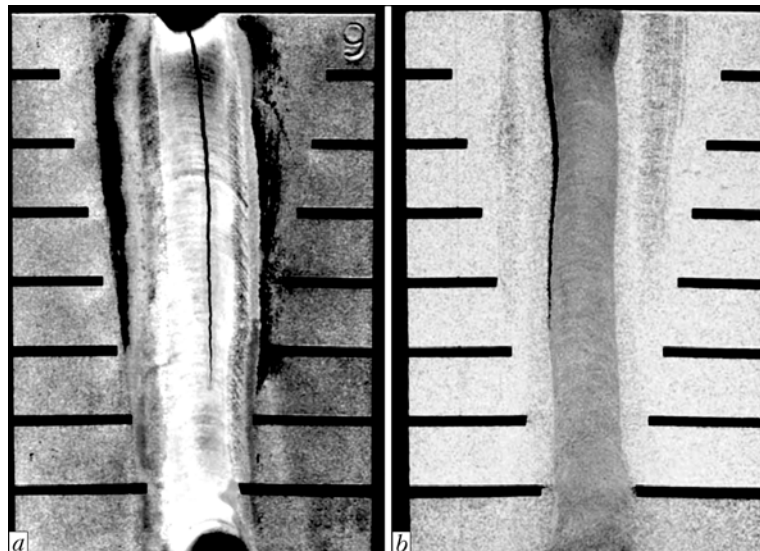
This paper presents the results of the conducted testing of sheets of Al-Zn-Mg-Cu system alloys 3 mm thick, the composition of which is given in Table 1. The sheets were subjected to heat treatment before welding. Depending on the degree of alloying, the alloys without scandium had the ultimate tensile strength from 510 to 655 MPa, and with scandium --- 520-720 MPa. Automatic argon-arc welding was performed by nonconsumable tungsten electrode in the following mode: welding current $I_w = 205-210$ A; welding speed $v_w = 14$ m/h; wire feed rate $v_f = 115$ m/h. Hot cracking susceptibility of the alloys was evaluated in welding of Houldcroft samples [6].

The Figure shows the typical appearance of cracks developing in argon-arc welding. In welding without the filler wire, hot cracks form predominantly in the weld central part. From the data given in Table 2 it is seen that in welding without the filler wire the hot crack length depends on the total quantity of the main alloying elements in the alloy. In samples of alloys without scandium the crack length decreases from 64 to 50 % at increase of the total content of zinc, copper and magnesium. The same tendency is found in scan-

Table 1. Composition of high-strength alloys of Al-Zn-Mg-Cu system

Alloy No.	Elemental composition, wt.%*						$\Sigma(\text{Zn} + \text{Mg} + \text{Cu}),$ wt. %	$\sigma_t,$ MPa
	Zn	Mg	Cu	Mn	Zr	Sc		
1	5.0	2.6	1.3	0.6	--	--	8.9	510
2	7.9	2.1	2.0	0.3	0.1	--	12.0	600
3	9.0	3.0	2.3	0.3	0.1	--	14.3	655
4	5.8	2.1	1.9	--	--	0.3	9.8	520
5	8.5	2.6	2.3	0.3	0.1	0.3	13.4	675
6	9.0	3.0	2.3	0.3	0.1	0.3	14.3	720

* Al is base.



Nature of cracking of Houldcroft samples of Al-Zn-Mg-Cu system alloys after welding without filler wire (a) and samples with scandium (b)

dium-modified alloys. At increase of the total content of the main alloying elements from 9.8 to 14.3 wt.% the index of metal hot brittleness A drops from 52 to 38 %. Scandium influence becomes stronger with increase of the total content of the main alloying elements.

Testing for the effectiveness of application of various fillers was conducted, considering the need for further lowering of the hot brittleness index and improvement of the mechanical properties of welded

Table 2. Alloy susceptibility to hot cracking in welding without filler wire

Alloy No.	$\Sigma(\text{Zn}+\text{Mg}+\text{Cu})$, wt. %	A, %*
1	8.9	64
2	12.0	60
3	14.3	50
4	9.8	52
5	13.4	46
6	14.3	38

* Here and furtheron data obtained by the results of testing 5-7 Houldcroft samples are given.

Table 3. Hot cracking susceptibility of alloys of Al-Zn-Mg-Cu system in welding with different filler wires

Alloy No.	$\Sigma(\text{Zn} + \text{Mg} + \text{Cu})$, wt. %	Filler wire composition	Scandium content in weld, wt. %	A, %
1	8.9	Al-6.2Mg-0.2Zr Al-6.2Mg-0.2Zr-0.5Sc	--	66
			0.17	64
2	12.0	Al-6.2Mg-0.2Zr Al-6.2Mg-0.2Zr-0.5Sc	--	60
			0.17	59
3	14.3	Al-6.2Mg-0.2Zr Al-6.2Mg-0.2Zr-0.5Sc	--	51
			0.17	49

joint. In alloys without scandium additives A values remained on the same level (Table 3). This is related to the fact that use of filler wire leads to crack propagation from the weld central part into the fusion zone (see the Figure), which has clusters of lower melting eutectic phases in the form of intergranular interlayers. Scandium present in the filler wire, has a modifying influence only on the weld metal. In the zone of weld fusion with the base metal its influence turns out to be insufficient in view of a low concentration, which results in only a slight lowering of hot brittleness values (by 1-2 %).

Simultaneous addition of scandium to the metal being welded and the filler wire (Table 4) allows ensuring the content of this element on the level of 0.33-0.37 wt.% in the weld metal. Its resistance to hot cracking in welding increases. It is found that increase of the total content of the main alloying elements in the alloys from 9.8 to 14.3 wt.% leads to

Table 4. Susceptibility of alloys of Al-Zn-Mg-Cu-Sc system to hot cracking in welding with Al-6.2Mg-0.2Zr-0.5Sc filler wire

Alloy No.	$\Sigma(\text{Zn}+\text{Mg}+\text{Cu})$, wt. %	Scandium content in weld, wt. %	A, %
4	9.8	0.33	46
5	13.4	0.37	40
6	14.3	0.37	29

Table 5. Susceptibility of Al-Zn-Mg-Cu system alloys to hot cracking in welding with filler wire of different composition

Alloy No.	$\Sigma(\text{Zn}+\text{Mg}+\text{Cu})$, wt. %	Filler wire composition	A, %
1	8.9	Al-6.2Mg-0.2Zr	66
		Al-8.6Mg-0.1Zr	49
6	14.3	Al-6.2Mg-0.2Zr-0.5Sc	29
		Al-10Mg-0.5Sc	15



lowering of the hot brittleness value from 46 to 29 %. Comparison of alloys of compositions 3 and 6 (see Table 1) showed that addition of 0.3 % Sc to the base metal allows reducing the hot crack length almost 2 times (Table 3, alloy 3; Table 5, alloy 6). Results of metallographic examination lead to the conclusion that scandium has an influence on the process of weld metal solidification. In particular, continuous low-melting eutectics along the crystallite grain boundaries become intermittent, this leading to increase of weld metal resistance to solidification cracking.

Influence of magnesium content in the filler wire on hot cracking susceptibility in welding was also studied. From the data given in Table 5 it is seen that the index of welded joint hot brittleness decreases with increase of the filler wire alloying level in alloy of the same composition.

Conducted studies confirmed the rationality of using scandium as a modifying additive to filler wire of AMg6 type and alloys of Al-Zn-Mg-Cu system to improve their hot cracking resistance in argon-arc welding.

CONCLUSIONS

1. Hot cracking resistance of alloys of Al-Zn-Mg-Cu system in argon-arc welding without the filler wire

depends on the total content of the main alloying elements in the alloys: at their increase from 8.9 to 14.3 % crack length decreases from 64 to 50 %.

2. Addition of 0.3 % Sc to the base metal and use of filler wire alloyed by 0.5 % Sc lower the hot brittleness index of welded joints by 20–35 %, compared to alloys without scandium additives.

3. Increase of the total content of alloying elements in the base metal to 14.3 wt.% and in the filler wire to 10 wt.%, as well as scandium presence in them, allow lowering the hot cracking susceptibility of the alloy to 15 %.

1. Fridlyander, I.N. (2003) High-strength aluminium alloys with zinc, magnesium and copper. *Metallovedenie i Term. Obrab. Metallov*, **9**, 11–13.
2. Khan, G.M., Nikiforov, A.O., Zakharov, V.V. et al. (1993) Influence of scandium content on structure and superplasticity factors of aluminium alloys of system Al-Zn-Mg-Sc-Zr. *Tsvet. Metally*, **11**, 55–58.
3. Davydov, V.G., Elagin, V.I., Zakharov, V.V. et al. (1996) On scandium and zirconium addition to aluminium alloys. *Ibid.*, **8**, 25–30.
4. Ishchenko, A.Ya. (2003) Aluminium high-strength alloys for welded structures. In: *Advanced materials and technologies*. Vol. 1. Kyiv: Akadempriodika.
5. Zakharov, V.V., Rostova, T.D. (1995) Scandium addition to aluminium copper-containing alloys. *Metallovedenie i Term. Obrab. Metallov*, **2**, 23–27.
6. Rabkin, D.M. (1986) *Metallurgy of fusion welding of aluminium and its alloys*. Kiev: Naukova Dumka.

NATURE OF FRACTURE OF B96 ALLOY DEPENDING ON HEATING CONDITIONS IN WELDING

T.M. LABUR, T.G. TARANOVA, V.A. KOSTIN, A.Ya. ISHCHEENKO, G.M. GRIGORENKO and A.A. CHAJKA
E.O. Paton Electric Welding Institute, NASU, Kiev, Ukraine

Fracture surface relief peculiarities of samples cut out from different segments of the HAZ of welded joints in high-strength aluminium alloy B96 were studied by fractography analysis method. General laws of crack initiation and propagation at eccentric tension were determined. The reasons for initiation of centers of crack concentration and microcrack formation on grain boundaries were established.

Keywords: fractographic analysis, high-strength aluminium alloy, thermophysical conditions of welding, failure mode, fracture relief, avalanche crack

Fracture of a real solid body is a complex process, including a multitude of genetically interrelated or mutually complementary phenomena. As a rule, fracture of samples, machine parts or structural elements proceeds in several parallel or successively running modes. Available data on the nature of fracture of ductile materials, including aluminium alloys [1–3], indicate that lowering of material resistance to crack initiation and propagation, is due to transition from the intragranular fracture to intergranular fracture mode, and depends on various factors of inner and outer impact. All the failure modes have one common indication of the fracture process, namely the work required for realization of the processes of crack in-

itiation and propagation. Brittle failure modes require small work of fracture, and tough ones require greater energy consumption. It should be noted that the fracture energy level in itself is not an indication of the fracture type, which can be established only through investigation of the nature of fracture energy change at variation of some structural and mechanical factors. Such factors include the welding modes and processes, postweld heat or thermomechanical treatment, as well as conditions of welded structure service.

It is known that the structure and properties of welded joints in high-strength aluminium alloys depend on the welding process and mode [1]. Metal overheating leads to segregation of alloying elements and impurities in the structure. This results in development of a non-uniformity of the their content and formation of intergranular interlayers consisting of



oversaturated phases, which lead to increase of stress concentration in the metal and have an essential influence on the service properties of welded joints.

Nature of processes running in the HAZ is usually determined by hardness measurement. In this case, however, just one aspect of the problem is revealed, namely lowering of strength at welding heating. Investigation of its influence on the resistance to crack initiation and propagation in the joints involves certain difficulties, which are due to the physical and structural inhomogeneity of the HAZ metal.

The purpose of this work is studying the features of variation of the HAZ metal structure under the impact of the thermal cycle of welding and influence of the latter on the joint failure mode, proceeding from the results of fractographic studies.

To achieve the above goal, fractograms of fractured samples of B96 alloy of Al-Zn-Mg-Cu alloying system in fusion welding were analyzed. The conditions of heating and cooling at the thermal cycle of welding were modeled on individual samples. This investigation procedure is described in detail in [3]. Topography of the fracture surface, its dependence on the kind of the stressed state of welded joint metal, and its structural inhomogeneity by composition were studied by the method of scanning electron microscopy. Nature and features of microdeformation and the concurrent structural changes running in the welded joint metal under static loading, were studied using a scanning electron microscope JSM-840 with Link 860/500 microanalyzer system at accelerating voltage of 15, 25 and 30 kV, respectively. Interaction of the electron beam of the scanning electron microscope with the structural components, containing alloying elements, including magnesium, copper, zirconium and scan-

dium, and present in the composition of the studied alloys, creates a certain contrast of the image. This allows conducting a qualitative evaluation of the change of the shape and dimensions of individual fragments of the alloy structure under different thermo-physical conditions, which are in place during the thermal cycle of welding in each of the studied HAZ sections.

As shown by investigations of the sample fracture surface by the method of fractographic analysis, metal fracture, which simulates the overheated condition in the zone of weld fusion with the base metal, runs in parallel to the axis of the applied load. Metal overheating in welding under the conditions of non-equilibrium solidus temperature leads to surface melting of the grains along their boundaries, which is exactly what is observed in the fracture surface relief of B96 alloy sample (Figure 1). In arc welding processes the fusion zone metal structure develops a thickening of grain boundaries, triple junctions and a considerable amount of eutectics are observed, and in electron beam welding mostly a polyhedral structure is formed. Less eutectics form in this case, which is positive for the metal hardness level [3].

The fracture section relief of the notch fracture surface is non-uniform and features a mixed mode, if the stressed state, loading sequence and microstructure promote simultaneous running of two fracture modes, namely the tough and brittle one (Figure 1, a). Fracture occurs both as a result of the manifestation of intercrystalline mode on the surface-melted grains (Figure 1, b), and of cleavage across the grain body (Figure 1, c). Orientation of the planes, along which the cracks propagate, in this case coincides with crystallographic orientation of the lattice. It is as-

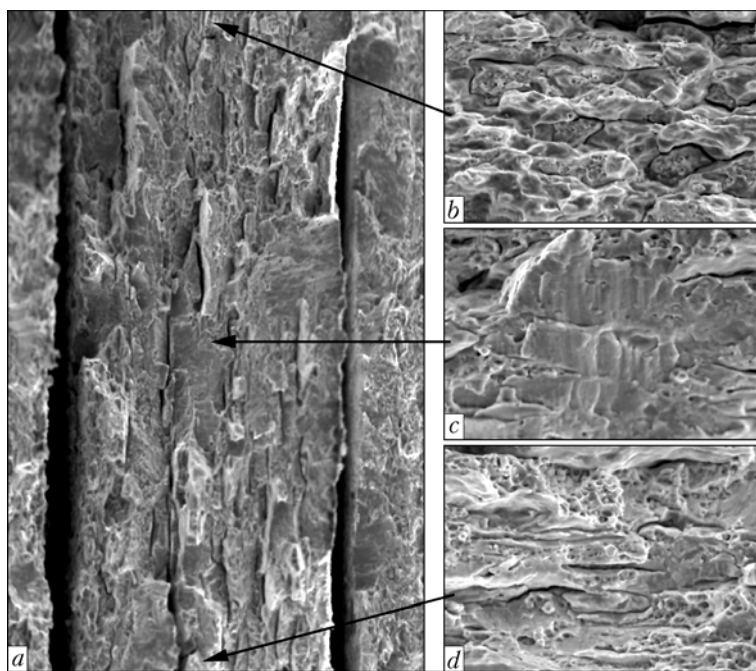


Figure 1. Fracture surface of a sample of B96 alloy after overheating at $T = (550 \pm 2) ^\circ\text{C}$ for 3 s, simulating the condition of the metal in the fusion zone: a — general view of the fracture ($\times 100$); b-d — sections under the notch, fracture and avalanche crack arresting, respectively ($\times 500$)

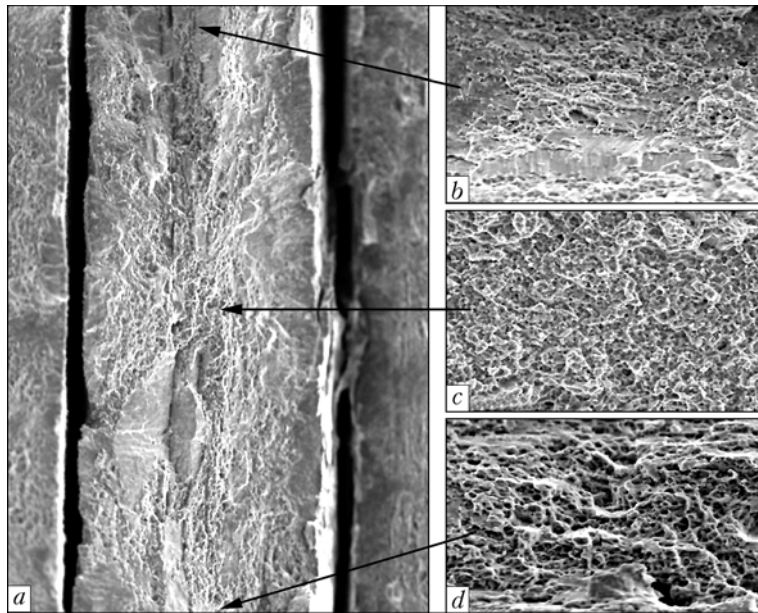


Figure 2. Fracture surface of a sample of B96 alloy after hardening at $T = (460 \pm 2) ^\circ\text{C}$ for 1 h and cooling in water: a–d — here and further on see Figure 1

sumed that the cause for this fracture mode, in addition to structural transformations, is decohesion of grain boundaries, resulting from their surface melting and precipitation of low-melting phase inclusions in the intergranular space under the conditions of high heating temperature ($550 ^\circ\text{C}$). Tensile stresses arising at metal cooling, lead to non-uniformity of microplastic deformation of the grains and stress concentration on their boundaries, particularly near the surface-melted grains, where microvoids form as a result of heating in welding, causing crack initiation in the fusion zone alongside phase inclusion formation.

Stressed state is induced in the HAZ metal as a result of a high diffusion mobility of alloying elements (zinc, magnesium, copper) and impurities moving from the grain bulk to their boundary. Formation of the eutectic interlayer and increase of stress concentration lead to conditions for an easier initiation of microcracks along the grain boundaries by the quasi-cleavage mechanism. This is indicated by stone-like relief of the fracture, usually typical for the mixed mode of crack initiation, when brittle structural components develop cracks, and tough fracture of the matrix runs in the shear mode.

A transcrystalline fracture type is found in the sample middle part, in which crack initiation occurs in brittle inclusions located along the grain boundaries (Figure 1, d). Where inclusions are absent, tough (intragranular) fracture mode is found. Difference in the dimensions of phase particles precipitating at heating, and distances between them result in a non-uniform nature of pit arrangement on the fracture relief. They are predominantly fine, and, therefore, the energy consumption for their formation at fracture is small. Tough relief fragments prevail in the fracture section, where the avalanche crack is arrested. Their presence points to microcrack initiation in the plane of contact of the matrix and inclusion due to decohe-

sion running in the alloy during segregation of the alloying elements at heating in welding.

Mode of avalanche crack development in samples heated up to the quenching temperature ($460 ^\circ\text{C}$, 1 h) with subsequent cooling in water (this simulating the thermal cycle of electron beam welding), is essentially different from crack propagation in the fractures after overheating. As is seen from Figure 2, a, there are more «tough» fragments and fewer cracks here. The crack initiation sites are clusters of phases precipitating in the case of heating in welding, as well as presence of intermetallics inclusions. After fracture they do not participate in formation of facets at tear under the impact of normal stresses, and, therefore, are on their bottom (Figure 2, b, c).

Individual cleavage sections against the background of a tough relief and numerous fine facets are observed in the vicinity of coarse phase precipitates. Their orientation shows that crack initiation proceeds in different crystallographic planes. Such a mechanism of crack initiation can be in place only in the case, if alloy ductility is high enough, and yield stress is insufficient for the crack to propagate just by the pore coalescence mechanism. A similar fracture mode is found also in the fracture section in the sample middle part and near the mouth of the avalanche crack (Figure 2, c, d). Quasi-cleavage is found near the tough facets. The noted features of the relief are indicative of a low plastic deformation of the metal, the degree of which in the local areas can be evaluated proceeding from the geometrical dimensions of individual relief elements, namely facets or tear ridges. Mostly short cracks are located in the fracture middle along the rolling direction, which is indicative of the high stress level in this section of the HAZ metal structure. A normal orientation of the ridges located along the elongated facets is also found. The fracture section of the avalanche crack arresting is characterized by con-

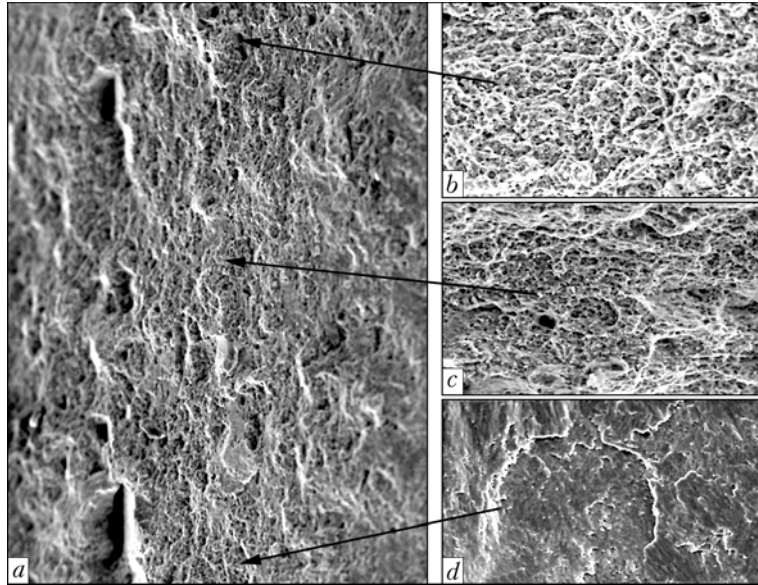


Figure 3. Fracture surface of a sample of B96 alloy after heating to the annealing temperature $T = (460 \pm 2) ^\circ\text{C}$ for 20 min and cooling in water

siderable intergranular fracture, occurring under the impact of a high level stressed state. Alternating sections of the pit and brittle intergranular fracture are indicative of embrittlement of the structural components under the conditions simulating the thermal cycle of nonconsumable electrode welding.

Nature of fracture surface in B96 alloy sample after heating up to the annealing temperature and cooling in water is typical of the thermal cycle of electron beam welding. The fracture contains about 80 % of the tough relief (Figure 3). Dispersed inclusions of 1 to 5 μm size precipitate in the metal due to a high cooling rate. This leads to formation of numerous small-sized facets with low ridges. Similar to the previous samples, the ridges are precisely oriented in the direction normal to the applied load.

In the fracture middle part the number of tough fragments decreases, and that of cleavage ones in-

creases. Fracture type in the fracture section, where the avalanche crack was stopped, is predominantly tough, although the crack initiates on brittle inclusions, as a result of tearing of the latter from the matrix. This is indicative of incomplete development of grain boundary segregations in this section of the HAZ of a weld made by electron beam welding with cooling in water.

The nature of the relief of B96 alloy sample changes at cooling in air after heating up to the annealing temperature (Figure 4). Type of sample fracture in this case is also mixed, however, among the numerous facets containing fine phase inclusions, also brittle fragments of the relief are observed (see Figure 3, a), which are absent at cooling in water. Fine pits in the studied alloy relief, having different dimensions and depth, are indicative of a low resistance to microcrack initiation during the action of normal local stresses.

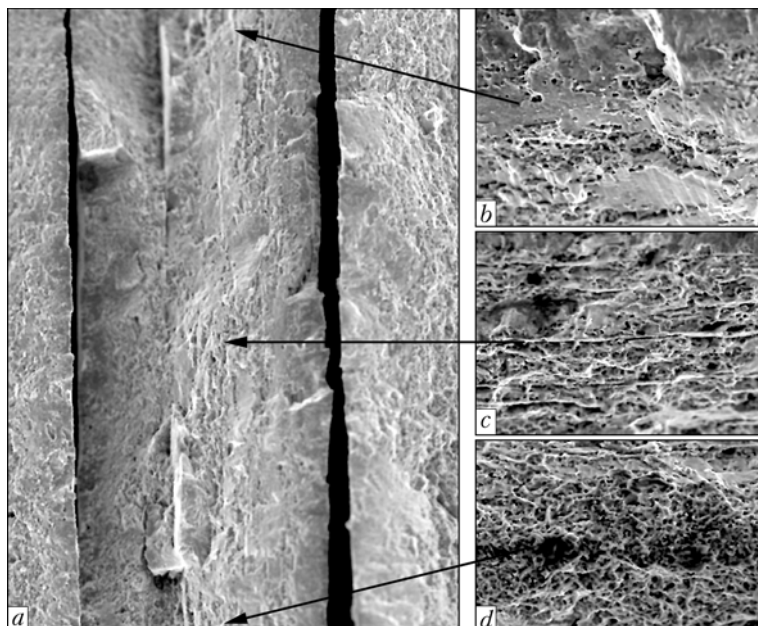


Figure 4. Fracture surface of a sample of B96 alloy after quenching at $T = (460 \pm 2) ^\circ\text{C}$ for 1 h and cooling in air



Phases appearing along the grain boundaries at metal heating create additional microstresses, and, thus contribute to the structure stressed state and are responsible for the local nature of crack initiation in the most brittle sections of the HAZ. This is confirmed by the presence of fragments of intermetallic particles broken up at cracking, on the pit bottom. In the center of sample fracture (Figure 4, *b, c*) the ridges have a precise orientation along the direction of action of tensile forces. This section features a mixed type relief, it, however, contains less cleavage fragments than the section under the notch. Cleavages are located mostly near the ridge group. The above section can be defined as the site of the change of the crack initiation mode in the crystallographic plane. In addition to cleavage fragments, the fracture also contains relief fragments, the surface of which is similar to oxide films, which, possibly, are exactly one of the causes for the change of crack initiation mode. Such a type of fracture is observed in the sample section, where the avalanche crack is arrested (Figure 4, *d*).

The main cause for crack initiation in the sample after heating up to the annealing temperature and cooling in air is fracture of the coarse particles located along the grain boundaries. They have the shape of geometrical figures and form predominantly in the sections, where the low-melting eutectic is located, which contains the compounds of the main alloying elements, namely zinc, copper, and magnesium. The cracks are 3–4 times longer than those formed at metal cooling in water (1–5 μm).

Fracture of samples of B96 alloy in the condition after heating up to the tempering temperature and cooling in air contains a considerable amount of fragments with small tough facets (Figure 5, *a*). Crack initiation occurs as a result of fracture of the phase particles located along the grain boundaries. They

have an elongated shape and are oriented along the base metal rolling direction, which leads to formation of facets of the same shape at fracture. Crack initiation results from tearing along the mated planes differing by the structural components, which is what accounts for appearance of numerous quasi-cleavage facets. Mostly isolated ridges are located around the facets, and between them — the sections of cleavage formed as a result of plastic shear in the metal under the conditions of deformation at testing for eccentric tension.

As the action of the thermal cycle in this section is rather short-term (3 min), no significant change of the texture is observed in the alloy fracture. In the sample middle part (Figure 5, *b, c*) «tough» facets alternate with small sections of quasi-cleavage, which may be due to the change of the crystallographic structure of the studied sample plane during crack propagation. In addition, individual sections, which look like cavities developing on eutectic formations, are found in the fracture [1]. They do not have any precise outlines, and are much wider than brittle cracks. The tough mode of their initiation is indicated by fine facets with low ridges and inclusions on the bottom. Type of fracture relief of the sample section, where the avalanche crack was arrested (Figure 5, *d*), is the same, as in its central section. As cooling in water of a sample of alloy B96, heated up to the tempering temperature, a greater number of tough sections appear in the fracture relief (Figure 6). This is indicative of the action of more favourable thermophysical conditions, which simulated electron beam welding. The high susceptibility to plastic deformation of the intergranular space metal is indicated by developed ridges around the facets, although the latter have small dimensions. This is also indicated by absence of microcracks on the surface of fractured samples.

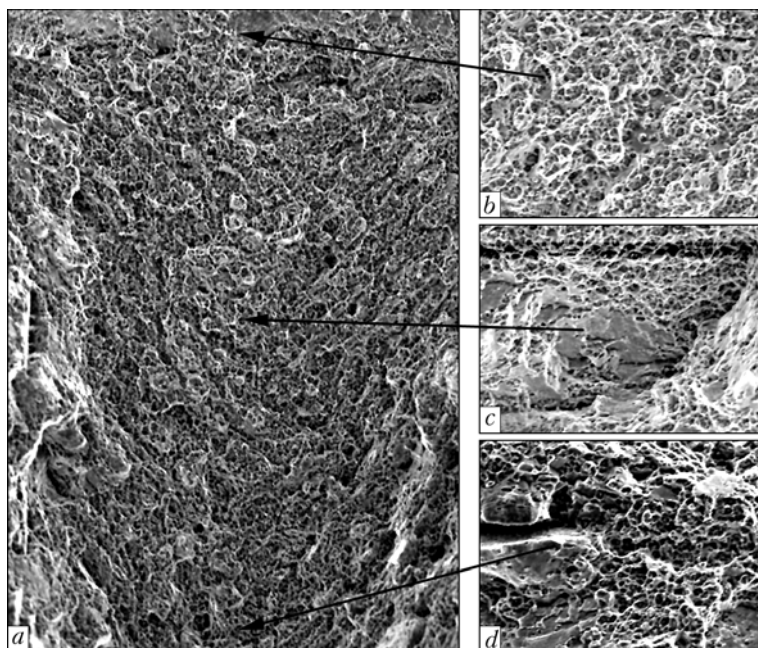


Figure 5. Fracture surface of a sample of alloy B96 after heating up to tempering temperature $T = (360 \pm 2) \text{ }^\circ\text{C}$ for 3 min and cooling in air

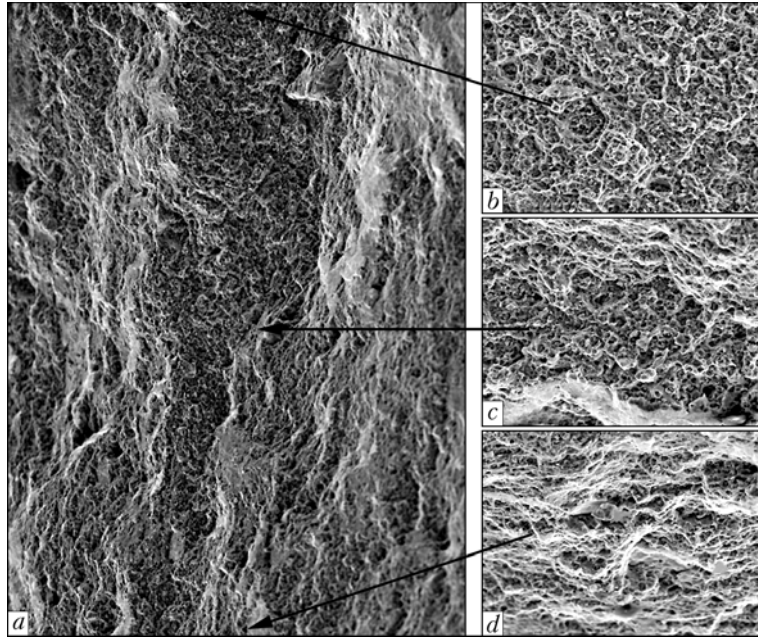


Figure 6. Fracture surface of a sample of alloy B96 after annealing at $T = (360 \pm 2) ^\circ\text{C}$ for 20 min and cooling in water

After artificial ageing at $T = 140 ^\circ\text{C}$ for 7 h fracture of samples from alloy B96 also runs by the mixed mode --- tough sections alternate with brittle sections (Figure 7). Proportion of areas taken up by them in the fracture, is equal to approximately 1:2. Cracks initiate predominantly in the bulk of inclusions, precipitating during ageing on the grain boundary. While coalescing, they form a stone-like fracture relief, which is characteristic for the case, when two or more fracture modes are active in the metal. It can be assumed that such a phenomenon is due to an abrupt lowering of grain-boundary energy due to adsorption or under the action of non-uniform segregation of the alloying elements and impurities on the grain bounda-

ries [2]. Fragments of broken inclusions are finely-dispersed and are located on the facet bottom.

The fracture mode is similar in the sample middle part and near the section, where the avalanche crack stopped (Figure 7, c, d). Cracks form in the layers along the rolling line. They are deep with flat walls which is, probably, related to brittle mode of crack propagation, running instantly along the entire height of the sample under the notch.

Fracture surface of a sample of B96 alloy in the initial condition has a brittle relief with delamination (Figure 8). Absence of plastic deformation zone in the fracture indicates that fracture ran in two stages. The first one is a plane-strain state, associated with the

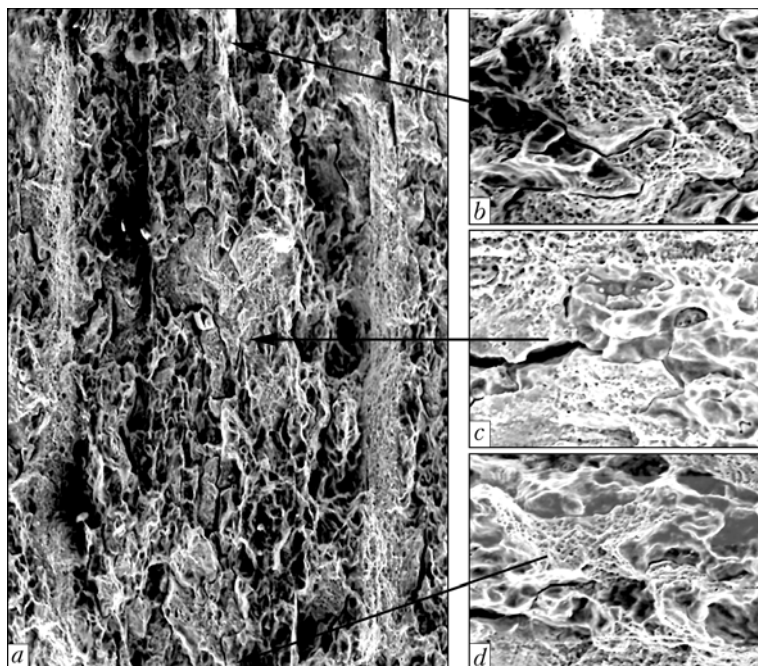


Figure 7. Fracture surface of a sample of B96 alloy in the section of ageing at $T = (140 \pm 2) ^\circ\text{C}$ for 7 h after heating in welding

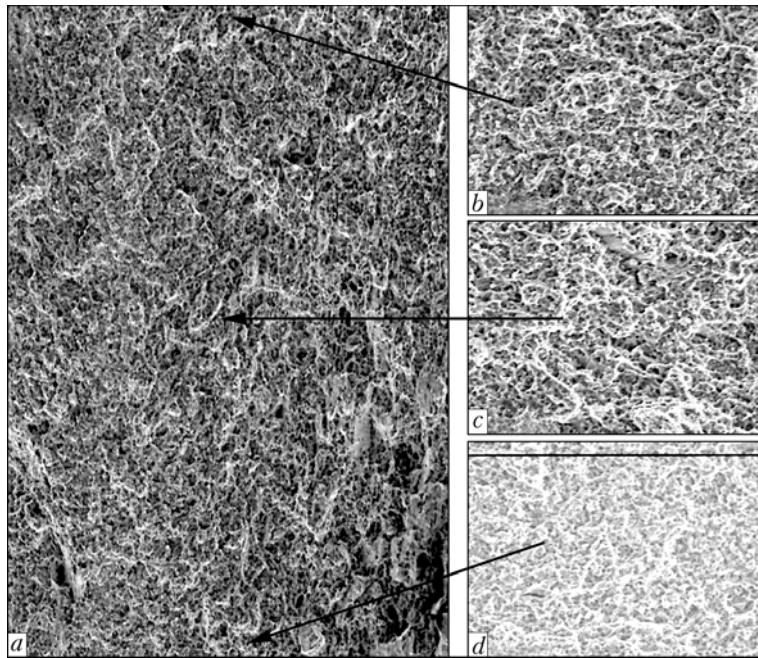


Figure 8. Fracture surface of a sample of B96 alloy in the initial condition

stressed state, caused by rolling during the sample manufacturing process and conditions of its testing. In this case, the metal is not able to actively absorb the plastic deformation energy. The second is a plane-stressed state which leads to formation of facets with low ridges and short cracks. In the sample middle the nature of the relief is similar, and a group of ridges is also formed. The ridge orientation coincides with the direction of the applied force under the conditions of eccentric tension. Figure 8, *d* shows a fragment of tough relief near the cleavage section. Such a type of the relief is found on the fracture surface in the section, where the avalanche crack stopped at sample fracture.

Thus, the thermophysical conditions characteristic of nonconsumable-electrode arc welding, lead to microcracking on grain boundaries and mixed fracture mode of B96 alloy sample, which may be due to an abrupt lowering of grain-boundary energy as a result of adsorption or non-uniform segregation of alloying elements and impurities under the impact of the thermal cycle.

A higher cooling rate of the metal under the conditions of electron beam welding promotes an increase of the amount of «tough» fragments of the relief on fractures with finer (from 1 to 5 μm) particles, precipitating in the grain bulk and along their boundaries. To prevent embrittlement of the structural components of the metal of welded joint HAZ, it is desirable to perform welding with a lower heat input, this increasing the metal resistance to crack initiation, and creating favourable conditions for combining the force and energy characteristics of fracture toughness in welded structures.

1. Ishchenko, A.Ya., Sklabinskaya, I.E. (1979) Specifics of transformations in heat-affected zone during welding of some high-strength aluminium alloys. *Avtomatich. Svarka*, **5**, 26–29.
2. Rabkin, D.M. (1986) *Metallurgy of fusion welding of aluminium and its alloys*. Kiev: Naukova Dumka.
3. Labur, T.M., Ishchenko, A.Ya., Taranova, T.G. et al. (2005) Features of crack initiation and propagation under the conditions of off-center tension of 1441 Al–Li alloy welded joints. *The Paton Welding J.*, **11**, 6–10.



MATHEMATICAL MODELING AND DEVELOPMENT OF MIG WELDING MONITORING CONTROLLER

F.N. KISILEVSKY and V.V. DOLINENKO

E.O. Paton Electric Welding Institute, NASU, Kiev, Ukraine

Object-oriented model of the MIG welding monitoring controller in the Simulink/MATLAB software environment is described. Investigations were carried out to study quality of operation of three monitoring algorithms. Implementation of the MIG welding controller with application of the object-oriented package xPC-Target/Simulink/MATLAB is suggested.

Keywords: MIG welding monitoring, object-oriented approach, controller, mathematical modeling, virtual welding, monitoring algorithms, MATLAB, Simulink, xPC-Target

Application of object-oriented designing of automatic control systems (ACS) allows, as it is known [1, 2], not just reducing terms of designing and increasing degree of the ready product correspondence to the technical requirements, but also achieving higher openness of the automatic system and possibility of repeated software use.

When developing object-oriented arc welding ACS, an important issue is development and modeling of low-level sub-systems, such as welding equipment controllers and subsystems for the welding process monitoring, whereby the following main requirements are established:

- reliable rigid real-time functioning;
- support of formed at the stage of the task assignment objects and abstractions of the welding data domain and protocols of interaction with other welding ACS subsystems;
- application of visual designing means, which allow developing the software.

In this work results of using object-oriented approach in designing the MIG welding ACS monitoring subsystem (hereinafter the controller) are presented. Designation of such controllers consists in performing input and primary processing of the welding signals (analogue and discrete ones) and forming estimation in general form of quality of the welding being performed on the basis of the real-time monitoring algorithms.

Software Simulink/MATLAB 6.x («Math-Works») was used as instrumental means for visual designing of the controller, whereby being guided by ideas of the help information accessibility and availability in the package of expanded composition of the mathematical class library [3–5].

The xPC-Target program package allows developing manager programs for IBM/PC compatible computers, operating in rigid real-time mode. Minimum operation time step of the manager program is

0.01 ms. Debugging process of the xPC-Target program is performed in the Simulink environment with application of the mode of remote communication with the controller over communication channel of Ethernet-10BaseT or RS-232c type.

The monitoring controller may be used both in composition of the arc welding ACS and as an independent system for controlling quality of the welding process performance.

The controller software fulfills several tasks:

- input, digitization, and filtration of the welding analogue signals;
- analysis of the welding signals for the purpose of detecting emergency situations, informing about non-conformance of the current welding mode to the assigned one;
- input of the estimations of the welding mode parameters and emergency situation labels into the upper-level computer over communication channel of Ethernet-10BaseT or RS-232c type;
- functioning of the controller in the welding simulation mode.

Due to synthesis of hierarchical system of mathematical models, functional system of the controller was obtained, shown in Figure 1. It should be noted that images of the functional systems correspond to Simulink models of respective subsystems.

The controller model consists of a number of models of a lower level:

- MIG welding model --- $F1$;
- analog-digital converter (ADC) --- $F2$;
- incremental sensor unit (encoder) --- $F3$;
- discrete input unit --- $F4$;
- serial transmitter unit of RS-232.RS-485 type --- $F5$;
- mathematical expectation (ME) and welding signal dispersion unit --- $F6$;
- probability ratio monitoring algorithm $SPRT$ --- $F7$;
- differentiating type monitoring algorithm IAL --- $F8$;
- integrating type monitoring algorithm $DPIO$ --- $F9$;

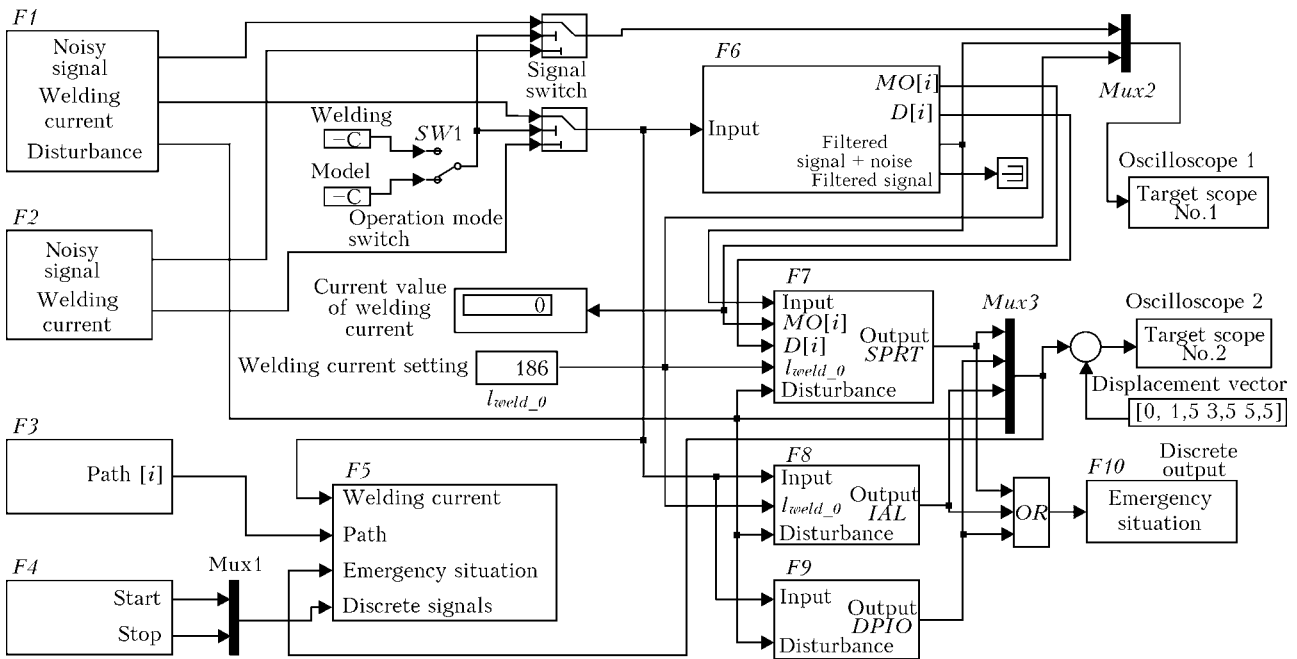


Figure 1. Functional scheme of MIG welding monitoring controller: *Mpx1–Mpx3* — multiplexers of signals; $i_{weld,0}$ — setting of welding current; the rest designations see in the text

- discrete output unit --- *F10*;
- signal and xPC-Target switches --- oscilloscopes.

Elements of the switches are designed for implementing testing mode, in which instead of real electric welding signals the MIG welding model signals are fed to the controller input.

Signal of the MIG welding model represents an additive mixture of two signals --- the determined and occasional ones.

The determined signal is formed by the model of the power source–welding torch system, which, in its turn, is a system of two models: the arc power source and the consumable electrode–arc system. The occasional component represents a stationary noise signal of normal distribution with zero ME, spectrum of which is formed by the low-pass filter (LPF) of 2nd order (LPF1) with transmission band 5000 Hz (according to 3 dB level). After summing the welding current signal is processed by LPF of Bessel type of 4th order (LPF2) with transmission band 100 Hz (according to 3 dB level) and digitized by the fetch-storage device, which simulate joint operation of the input hardware analogue filter and ADC.

Depending upon position of the switch *SW1* the controller may function in one of two modes --- regular «welding» and test (model) modes. The signal switch ensures flexibility of the controller. In regular mode signal from the ADC output is used, and in testing --- signal of the MIG welding model output. Then the welding current signal is fed to input of the statistical parameter estimation unit *F6* and inputs of the algorithms of integrating *IAL* (*F8*) and differentiating *DPIO* (*F9*) types.

Estimations of *D* and ME dispersion are calculated using the following recurrence formulas:

$$D[i] = D[i - 1] + \frac{1}{N - 1} ((x_c[i] - MO[i])^2 - (x_c[i - N] - MO[i - N])^2);$$

$$MO[i] = MO[i - 1] + \frac{1}{N} (x_c[i] - x_c[i - N]),$$

where *i* is the index of the data point being processed; *N* is the number of averaging points; x_c is the input signal. These estimations are then fed to inputs of the probability ratio monitoring algorithm *SPRT* (*F7*).

Emergency situation signals, which are formed by monitoring algorithms *F7–F9*, may be used for their bringing on the controller video monitor screen, switching of the signal indicators with application of the discrete signal output unit *F10*, and formation of information messages to the upper-level computer through the serial transmitter unit *F5*. It should be noted that availability of a video monitor in composition of the controller is not compulsory.

In the process of operation the controller also forms information messages into the upper-level computer, containing data on the weld length, averaged values of welding signals, and state of the synchronization signals of the welding cyclogram «Start» and «Stop».

Investigations of operation of the monitoring algorithms were carried out in the virtual welding mode with application of the MIG welding model, whereby the welding current signals were synthesized, which reflected response to disturbance at the distance torch–item, wire feed rate, and voltages of the arc power supply. For the first type of disturbances passage above obstacles of rectangular (a bar), saw-tooth (a wedge), and harmonic types was simulated.

It should be noted that the task of exact description of all physical process, which proceed in the power source–welding torch–arc–weld pool system was not assigned in the modeling (in particular, formation of



the weld, change of the sliding contact in the welding torch, etc. were not taken into account). At the same time, for making adequate estimation of operation of the monitoring algorithms and determining boundary values of their transmission coefficients, it is necessary to sufficiently accurately repeat shape of the welding signals. For this purpose a known dynamic mathematical model of the arc sensor was implemented, which allowed taking into account effect of the arc self-regulation and explaining changes of the shape and amplitude of disturbance signals depending upon output resistance of the arc power supply source.

Mathematical model of the arc sensor describes behavior of the consumable electrode-arc system for the MIG welding. It represents a system of linear differential equations [6, 7]:

$$\frac{dI_{arc}}{dt} = \frac{U_{xx} - \beta^2}{L_i} - I_{arc} \left(\frac{R_i}{L_i} + I_{el} \frac{\alpha^1}{SL_i} + \frac{\beta^1}{L_i} \right) + I_{arc}^{-1} \left(\frac{\alpha^2 v_{feed} S - \beta^3}{L_i} \right) - (I_{dist} - I_{el}) \frac{\beta^4}{L_i} \quad (1)$$

$$\frac{dI_{el}}{dt} = v_{feed} - I_{el} \frac{\gamma^2}{S} - I_{arc} \frac{\gamma^2}{S} \quad (2)$$

where $\alpha_1, \alpha_2, \beta_1-\beta_4, \lambda_1, \lambda_2$ are the welding constants; R_i is the active resistance of the welding circuit, Ohm; L_i is the welding choke inductivity, H; I_{arc} is the arc current, A; U_{xx} is the welding power supply voltage, V; S is the wire cross-section, mm^2 ; v_{feed} is the wire feed rate, mm/s; $I_{el}, I_{arc}, I_{dist}$ is the length of electrode extension and arc, and torch-item distance, mm, respectively, whereby

$$I_{dist} = I_{el} + I_{arc}$$

Identification of this mathematical model for the MIG welding scheme, presented in Figure 2, was carried out.

Mixture of gases 80 % Ar + 20 % CO₂ was used as a shielding atmosphere. Deposition of low-carbon steel 5 mm thick was performed under the following

conditions: welding current --- 170-190 A; arc voltage --- 22-35 V; Sv-08G2S wire feed rate --- 130-160 mm/s; diameter of the wire --- 1.2 mm; the torch-item distance --- 24-30 mm. The arc power supply source of VDU-506U3 type was used in the experiments. Measurement of the electrode extension and the arc length was made using a video camera, equipped with a protective optical filter. According to results of the experiment the following values of the coefficients were obtained (dimensions of a quantity are not given): $\alpha_1 = 1.1 \cdot 10^{-3}, \alpha_2 = 7.06, \beta_1 = 0.049, \beta_2 = 9.2, \beta_3 = 2.22, \beta_4 = 1.31, \gamma_1 = 0.83, \gamma_2 = 3.08 \cdot 10^{-5}$.

On the basis of the experimental data obtained and in correspondence with the mathematical model (1), (2) functional scheme of the model of the consumable electrode-arc system was synthesized.

Check of the mathematical model (1), (2) adequacy was performed by estimation of the response to transitional actions of such variables as wire feed rate v_{feed} and the torch-item distance I_{dist} , whereby incongruity of the arc current signal shape with results of experimental investigations was detected [8]. The reason of this was difference in output characteristics of the arc power source Migatronec BDH S550 and used by us power source of VDU-506U3 type.

That's why the model was synthesized, which took into account with sufficient accuracy real characteristics of the arc power source. Functional scheme of the power source-welding torch model is shown in Figure 3.

In this model output characteristics (of «rigid» type) of the VDU-506U3 source are implemented by the following linear transfer function:

$$U_{xx} = (B + R_{out})I_{weld_control} - R_{out}I_{weld_back} + A,$$

where A, B are the constants; R_{out} is the output resistance of the power source; $I_{weld_control}$ is the output current control parameter; I_{weld_back} is the arc current sensor signal.

The modeling showed that correspondence may be achieved in case of increasing output resistance parameter of the arc power supply source R_{out} up to

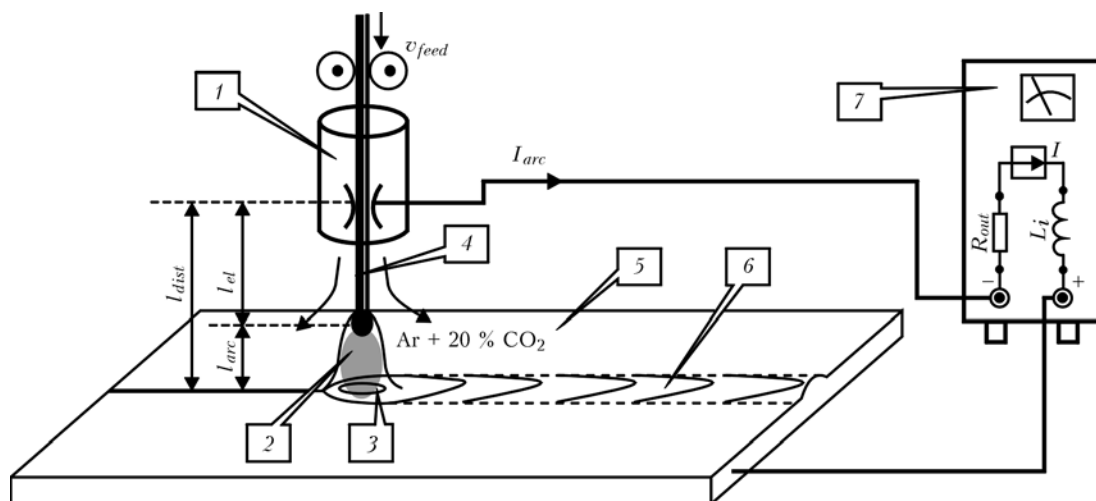


Figure 2. Scheme of MIG welding: 1 --- torch; 2 --- arc; 3 --- weld pool; 4 --- electrode extension; 5 --- item; 6 --- weld; 7 --- arc power supply source

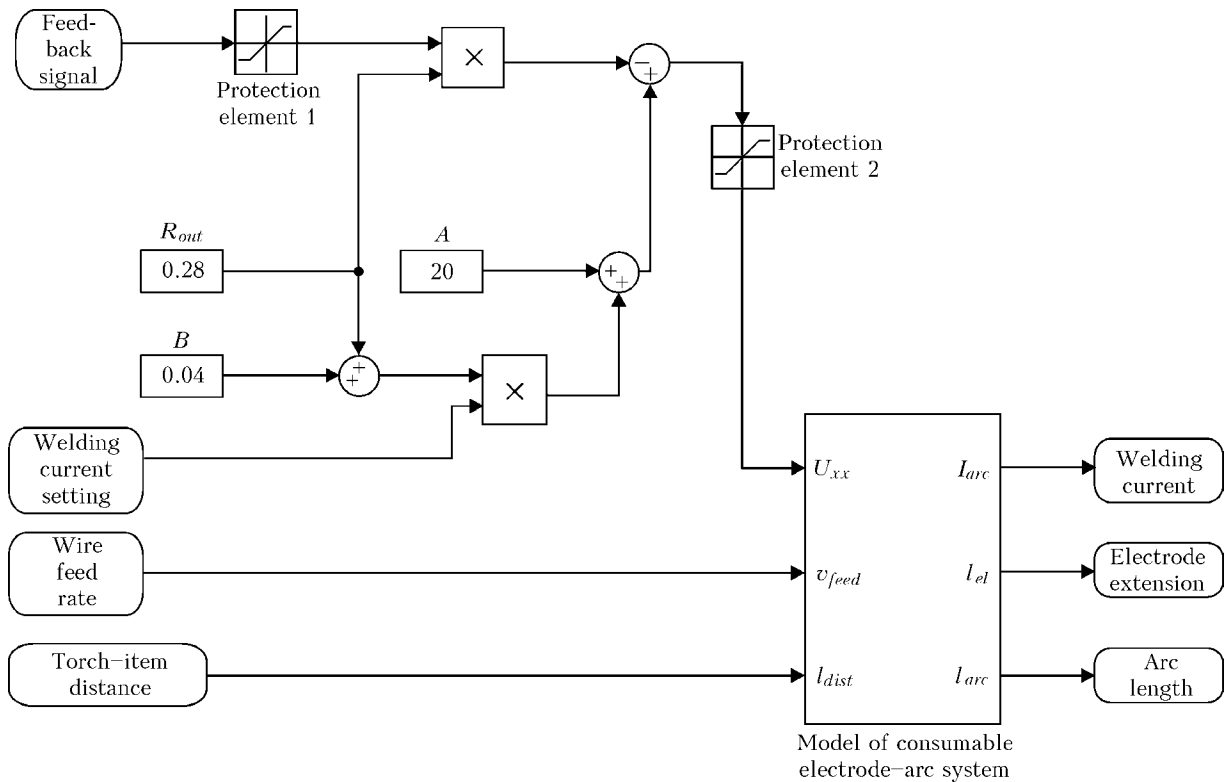


Figure 3. Functional scheme of power source-welding torch model

3–6 Ohm (typical value R_{out} for power source of VDU-506U3 type at operation currents 100–300 A is 0.28 Ohm).

So, good correspondence of behavior of the MIG welding model with experimental results is obtained, which allows investigating operation of the monitoring algorithms in the virtual MIG welding mode.

The $SPRT$ monitoring algorithm, which forms results of statistical check of the hypotheses (the probability ratio), is described by the following recurrent formula [8]:

$$SPRT[i] = SPRT[i - 1] + \frac{m_0 - MO[i]}{D[i]} \times \left(m_0 - x_c[i] - \frac{m_0 - MO[i]}{2} \right)$$

where m_0 is the assigned value of the welding signal control level.

In the process of monitoring current $SPRT[i]$ value is compared with the threshold value h_0 , and if condition $SPRT[i] < -h_0$ is fulfilled, emergency signal AL_{SPRT} is formed.

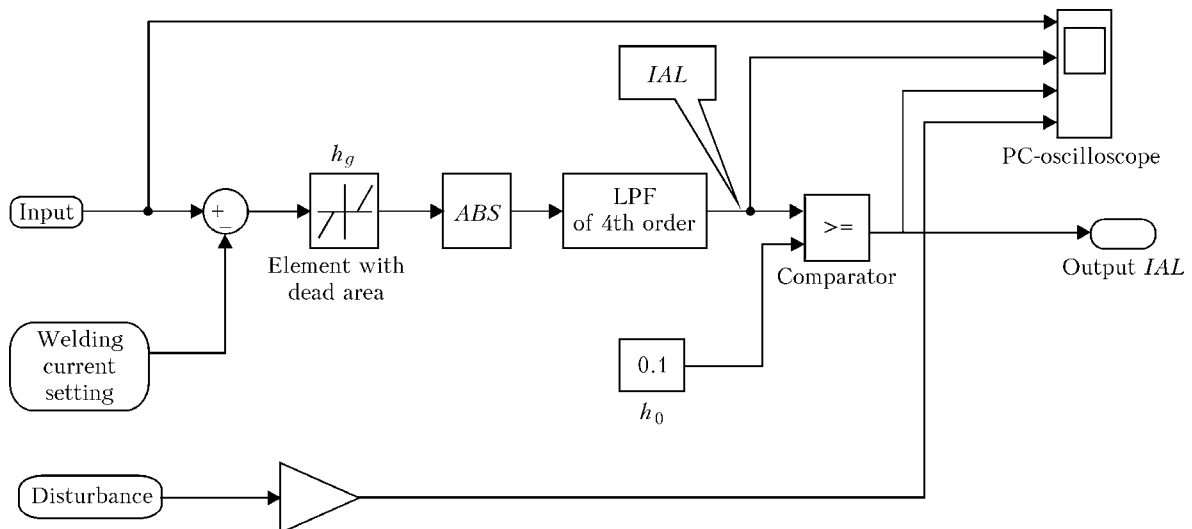


Figure 4. Functional scheme of IAL monitoring algorithm of integrating type: ABS --- module element; h_g --- dead area; h_0 --- actuation threshold



As alternative to the *SPRT* algorithm, known integrating type algorithms may be used, built according to the following scheme: LPF–element with the dead area–rectifier–comparator; element with the dead area–rectifier–LPF–comparator. As showed preliminary investigations, second type of the integrating algorithm (hereinafter *IAL*) is preferential due to its higher dynamic characteristics. In Figure 4 functional scheme of such monitoring algorithm is presented.

Shown on the scheme PC-oscilloscope element is used in modeling. In the *IAL* monitoring algorithm ripple LPF of Bessel type of 4th order with transmission band 1 Hz (according to 3 dB level) is used after non-linear element with a regulated dead area h_g and the rectifier. When an averaged signal leaves limits of the comparator actuation zone h_0 , the emergency signal AL_{IAL} is formed. Due to simplicity, this monitoring algorithm is rather widely used in practice.

Sometimes the need occurs to trace not statistical, but dynamic changes in the welding mode parameters. For this purpose monitoring algorithms of differentiated type --- smoothed differentiated semi-interval integral estimations --- may be used.

Output of the monitoring algorithm of first type is described by the following expression:

$$g(t) = \frac{1}{T} \int_{t-T}^t \left(\frac{dx_c}{dt} \right) dt,$$

where t is the current time; T is the averaging interval.

For the investigations algorithm of second type is selected, operation of which is more indicative. This *DPIO* monitoring algorithm implements a differentiating filter after averaging filters:

$$DPIO(t) = \left[\frac{2}{T} \int_{t-T}^{t-\frac{T}{2}} dx_c d\tau - \frac{2}{T} \int_{t-\frac{T}{2}}^t dx_c d\tau \right] / dt = \frac{2}{Tdt} \left(\int_{t-T}^{t-\frac{T}{2}} dx_c d\tau - \int_{t-\frac{T}{2}}^t dx_c d\tau \right) \quad (3)$$

where τ is the auxiliary variable of integration.

So, function (3) forms an output differentiation signal between two smoothed signals, following one after another in time with a delay, equal to half of the smoothing interval T . After simple transformations in recurrent form it may be written as

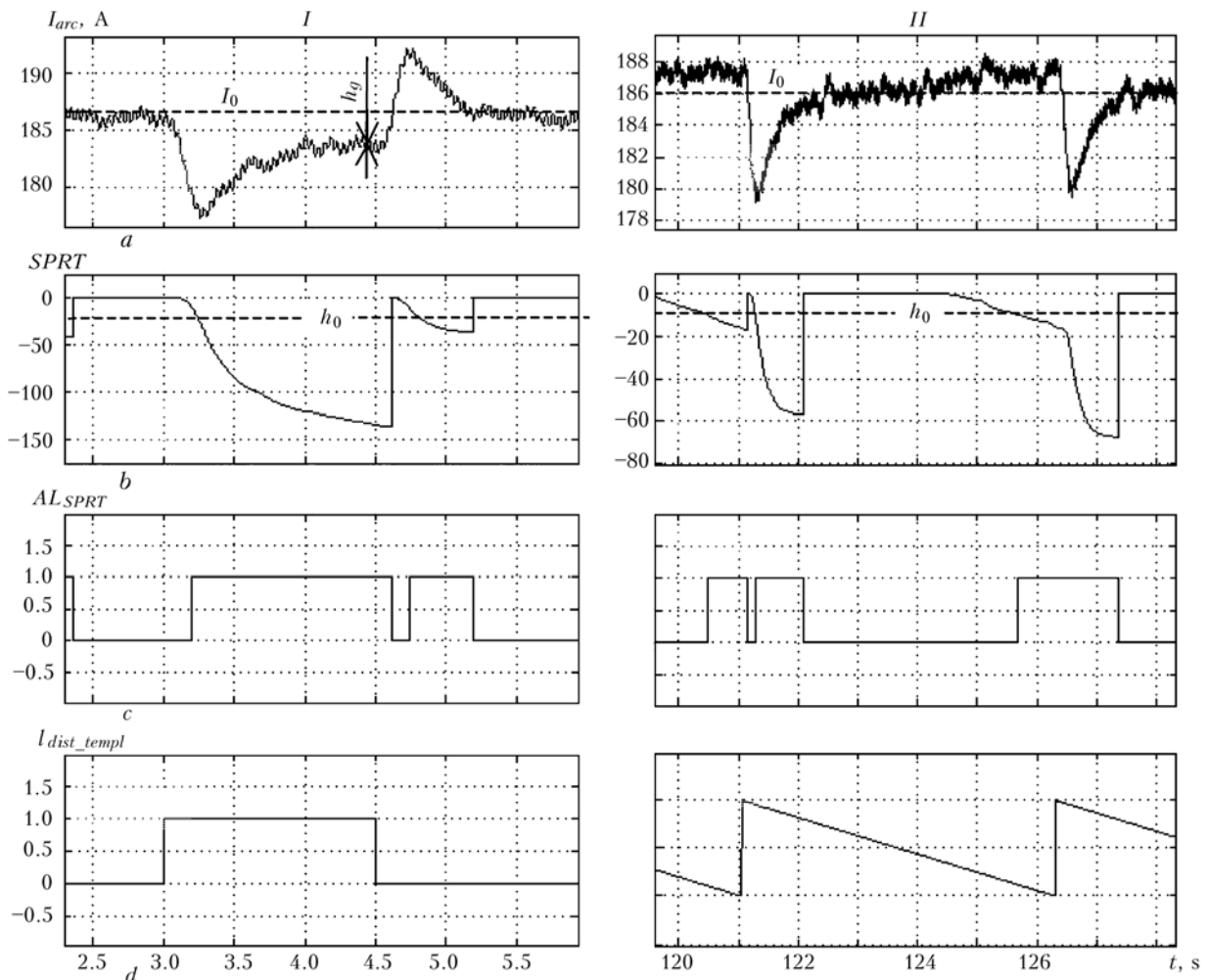


Figure 5. Modeling of *SPRT* algorithm operation for disturbance in form of torch–item distance change (power source of VDU-506U3 type) of rectangular (*I*) and saw-tooth shape (*II*): *a* --- filtered welding signal, noised by high-frequency signal; *b* --- output of *SPRT* monitoring algorithm; *c*, *d* --- signal of control emergency and disturbance, respectively; $h_g = 1$ A; I_0 --- level of welding mode setting



$$DPIO[i] - DPIO[i - 1] = \frac{2}{N} \times \left(2x_c \left[i - \frac{N}{2} \right] - x_c[i - N] - x_c[i] \right)$$

where $x_c[i - N/2]$ is the sample of a signal being analyzed in the middle of a smoothing interval; $x_c[i - N]$ and $x_c[i]$ is the same on the smoothing interval edges.

It should be noted that such function of the monitoring is synthesized for the first time in recurrent form and in comparison with the known similar approach [8] allows forming estimations, which are invariant to the number N of points of the analyzed signal averaging. In the process of monitoring module of the $DPIO[i]$ current value is compared with the threshold h_0 , and if condition $|DPIO[i]| > h_0$ is fulfilled, the emergency signal AL_{DPIO} is formed.

In investigation of the quality of operation of the monitoring algorithms the following requirements were taken into account:

- the algorithms should have dead area (for input signal of welding), boundaries of which may be regulated;
- within dead area outputs of the algorithms should correspond to absence of the control emergency signal;
- the control emergency signal should have the character of one-time actuation.

Investigations of the monitoring algorithms for different types of disturbance signals (rectangular, saw-tooth, short pulse, and harmonic ones) and different welding parameters (torch-item distance, wire feed rate, and arc voltage) were carried out. The most indicative results are presented in Figures 5--7. They reflect quality of operation of three monitoring algorithms for rectangular and saw-tooth disturbance signals, which are superimposed on the parameter torch-item distance I_{dist} .

Results of investigation of the *SPRT* monitoring algorithm showed (Figure 5) that presence of the only parameter h_0 does not allow assigning width of the

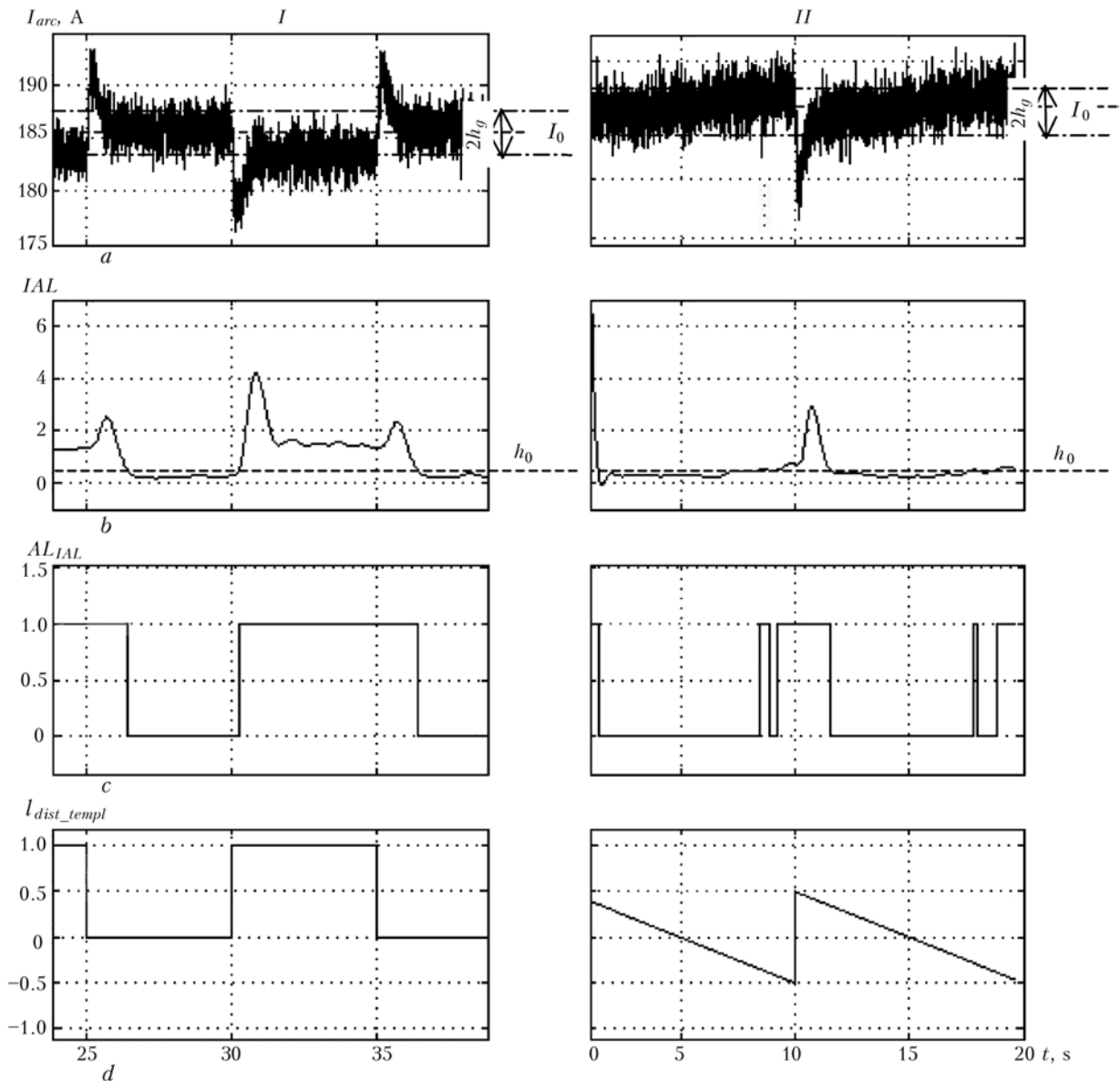


Figure 6. Modeling of IAL algorithm operation for disturbance in form of torch-item distance change (power source of VDU-506U3 type) of rectangular (*I*) and saw-tooth shape (*II*): *a*, *c*, *d* — the same as in Figure 5; *b* — output of IAL monitoring algorithm



dead area, which is determined by dispersion of the noise component in the welding signal. That's why an disturbance signal, which is present in the welding signal, may be masked by a strengthened noise. In this connection the *SPRT* algorithm was modernized: LPF with optimum characteristics was added, which filtered in the best way the noise signal and, at the same time, ensured minimum distortion of the disturbance signal shape. The produced signal was summed with the auxiliary high-frequency (150–400 Hz) signal with amplitude h_g , which simulated the welding noise signal. The modeling results demonstrated good quality of this algorithm operation both at statistical and dynamical disturbances. The *SPRT* monitoring algorithm may reliably register pulse disturbances, having duration up to 0.5 s. Adjustment of this algorithm consists in assignment of the dead area h_g and the actuation threshold level h_0 within 20–100 (ensures absence of the algorithm actuations for optimum welding mode).

The monitoring algorithm of integration type *IAL* may be used for tracking both slowly changing and

pulse disturbances. Comparative investigations of its behavior in dynamics showed (Figure 6) that when a ripple filter is correctly chosen, formation of emergency situation signals occurs without a significant delay. To shortcomings of this algorithm relates the fact that when welding conditions change slowly, it may repeatedly produce emergency situation signals. Adjustment of the algorithm consists in assignment of the dead area h_g and the actuation level h_0 within 0–1.

The *DPIO* differentiating algorithm is designed for formation of emergency situation signals only in case of pulse disturbances. Statistical changes in the welding current signal do not cause actuation of this algorithm (Figure 7). It may be useful in those cases, when it is necessary to register short-term changes in conditions of welding, which may cause defects in the weld.

It is known that short-term pulse disturbances, having duration up to 0.1 s, do not cause formation of defects. That's why the *DPIO* monitoring algorithms may be recommended for registration of pulse disturbances, having duration from 0.1 to 0.5 s. Ad-

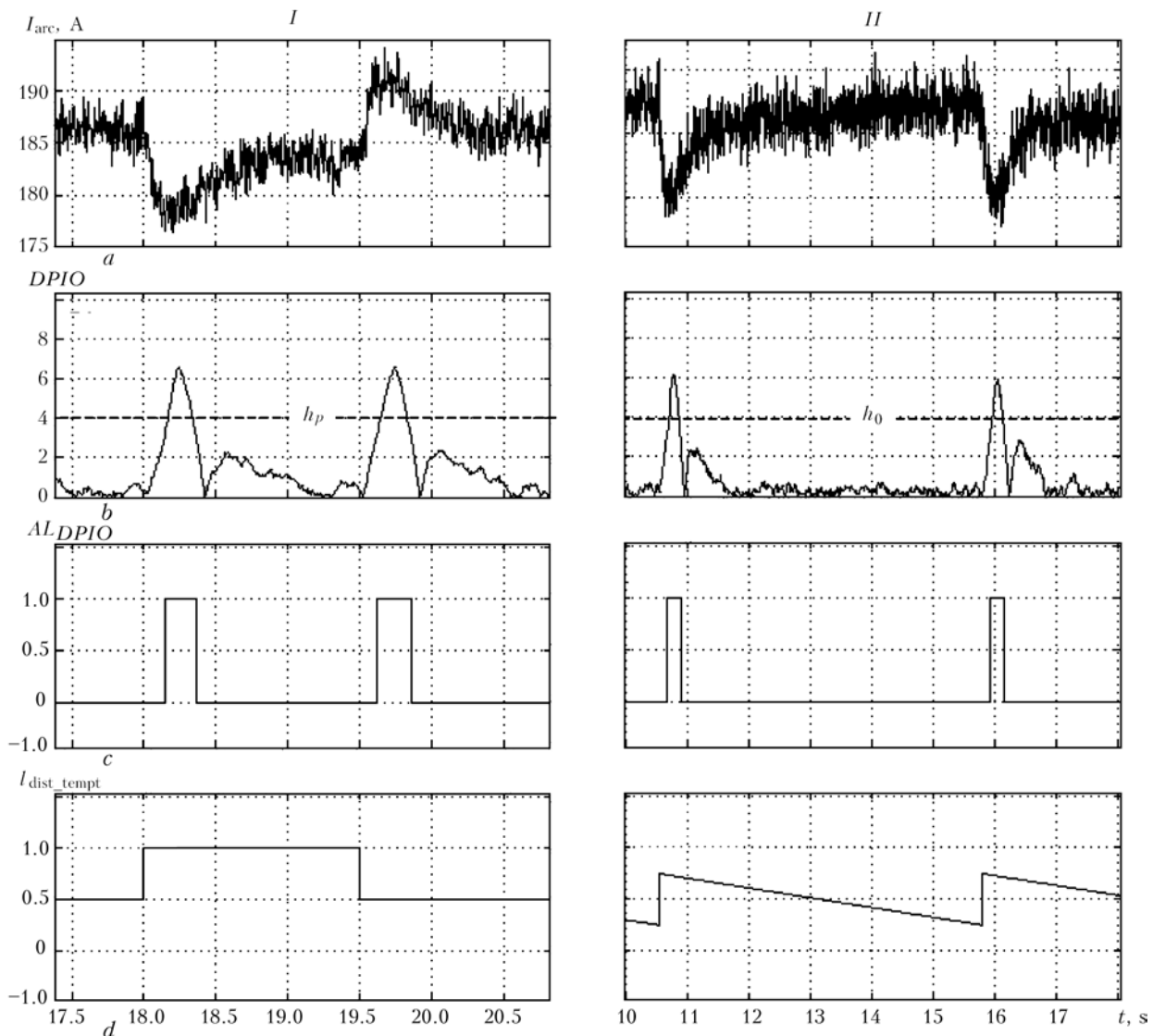


Figure 7. Modeling of *DPIO* algorithm operation for disturbance in form of torch–item distance change (power source of VDU-506U3 type) of rectangular (*I*) and saw-tooth shape (*II*): *a*, *c*, *d* — the same as in Figure 5; *b* — output of *DPIO* algorithm

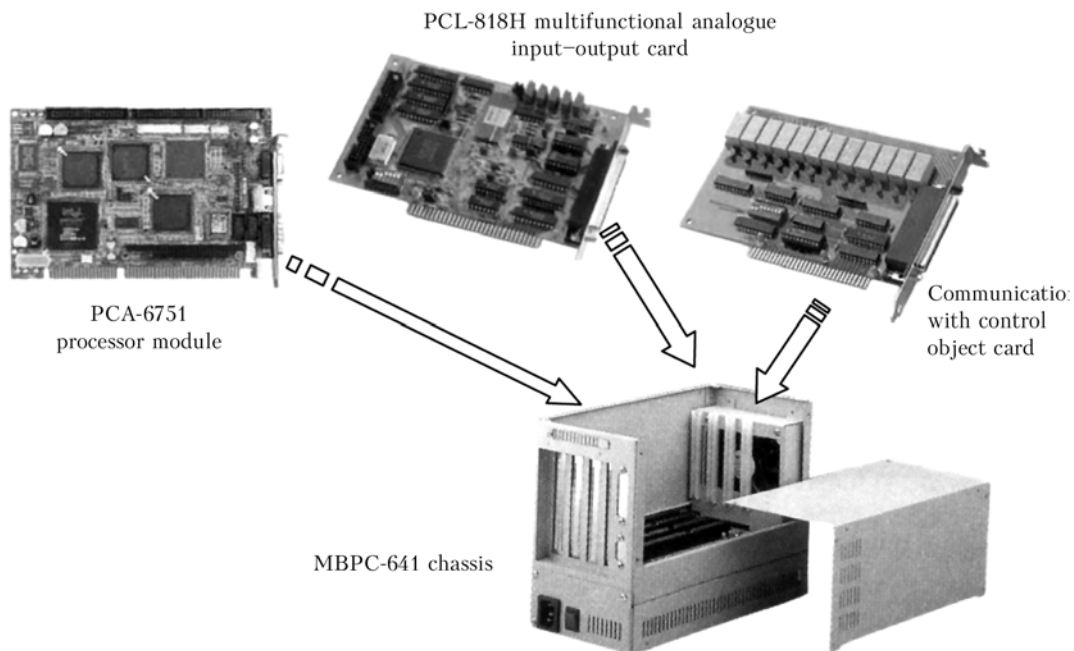


Figure 8. Hardware composition of MIG welding monitoring controller

justment of the algorithm consists in assignment of h_0 values within 2–10 (it should ensure absence of the algorithm actuations for optimum condition of welding) and smoothing interval N (in our case $N = 200$).

So, on the basis of carried out investigations the *SPRT* monitoring algorithm may be singled out, which meets all formulated requirements. At the same time for monitoring pulse disturbances the *DPIO* differential algorithm may be recommended, which allows reliable registering deviations in the welding conditions, having duration up to 0.1 s.

Implementation of the controller with application of the *xPC-Target* software is performed using the hardware, which is described in the *Simulink* package. Application of other modules is also possible, but in this case it is necessary to develop respective drivers for them. Hardware of the controller of series «Advantech», structure of which is presented in Figure 8, is used.

The controller includes the following hardware: module of the PCA-6751 processor, multifunctional input-output card PCL-818H, communication card with the control object and chassis MBPC-641. Module of the PCA-6751 processor represents the IBM/PC --- compatible industrial computer with processor Pentium MMX, operating at frequency 266 MHz and having random access memory (RAM) of 32 Mb. It includes controller Ethernet-10BaseT, two serial interfaces of RS-232/RS-485 type, controllers of VGA-display, and hard and floppy disk drives. Multifunctional input-output card PCL-818H carries out input and digitization of analogue welding signals with discreteness 12 bits and ultimate frequency 100 kHz. It includes six input-output lines of discrete signals and one 16-bit counter. The communication card with a control object has in its composition analogue LPF, which are located before the analogue input module and designed for limiting spectrum of

welding signals down to the half-value level of discretization frequency. On this card matching amplifiers-converters for input-output of discrete signals are also located.

Rigid real-time mode of operation is achieved due to application of the real-time operation system of *RTTarget-32* («On Time») type. Time step of the managing program is 1 ms (loading of the processor in this case is about 15 %). The managing program is entered either from a floppy disk or from a flash-disk and than only RAM is used in operation. It should be noted that the controller has not a hard disk, which allows operating it under conditions of shock loads and vibration.

So, an approach to the object-oriented development of the MIG welding monitoring controllers is proposed, in which method of end-to-end designing with application of software *xPC-Target Simulink/MATLAB* is used.

1. Buch, G. (2001) *Object-oriented analysis and design (with examples of applications on C++)*. Moscow: Binom.
2. Kisilevsky, F.N., Dolinenko, V.V. (2001) Object-oriented programming of systems of welding technological process control. *The Paton Welding J.*, **6**, 33–39.
3. Diakonov, V.P. (2004) *MATLAB 6/6.1/6.5 + Simulink. Principles of application: Complete user manual*. Moscow: SOLON-Press.
4. Lazarev, Yu.I. (2004) *Modeling of processes and systems in MATLAB*: Textbook. Kiev: BHV.
5. Chernykh, I.V. (2003) *Simulink: Medium of formation of engineering applications*. Moscow: Dialog-MIFI.
6. Dolinenko, V.V., Kisilevsky, F.N. (1988) Determination of torch weaving in welding with oscillations. In: *Inform. Materialy SEV*, Issue 1, 37–41.
7. Dolinenko, V.V. (1989) *Evaluation and control of torch position using the electric welding arc parameters*: Syn. of Thesis for Cand. of Techn. Sci. Degree. Kiev.
8. Adolfsson, S., Bahrami, A., Bolmsjo, G. et al. (1999) Quality monitoring in robotized spray GMA welding. *Int. J. Joining of Materials*, **10**(1), 3–23.



MODEL OF TRANSPORTATION OF HYDROGEN WITH DISLOCATIONS*

V.I. SHVACHKO and A.V. IGNATENKO

E.O. Paton Electric Welding Institute, NASU, Kiev, Ukraine

The model is suggested to describe the transportation of hydrogen atoms with edge dislocations, accounting for interaction of a hydrogen atom with edge dislocation and crystalline lattice of iron, as well as interaction of hydrogen atoms between each other. This allows the amount of transported hydrogen to be calculated depending upon the temperature of metal, velocity of an edge dislocation and concentration of free hydrogen. As shown by the numerical calculations, the transportation of hydrogen with an edge dislocation has maximum at a temperature close to the normal one.

Keywords: reversible hydrogen brittleness, transportation of hydrogen, edge dislocations, plastic flow, temperature dependence, strain rate

The problem of interaction of hydrogen with metals has been attracting an increased attention during the last decades. International and national conferences are held each year, and dozens of articles, extensive reviews and books are published, dedicated to different aspects of this problem. Theoretical developments and experimental studies are under way. An increasing interest in the problem of interaction of hydrogen with metals is caused by practical significance of this problem for control of the quality of welding, metal products, oil and gas industry, nuclear and hydrogen power generation.

One of the obstacles in ensuring reliability of welded metal structures is an embrittling action of hydrogen that dissolves in the weld metal during welding [1]. Among different types of hydrogen-induced brittleness of structural steels, of special notice is a reversible hydrogen brittleness (RHB) [2], which is

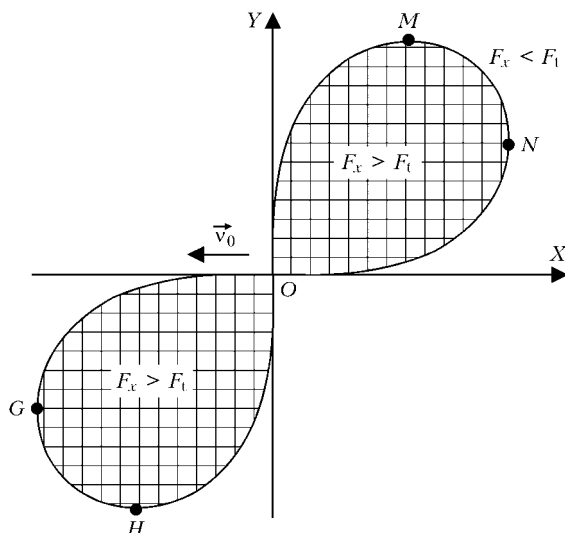


Figure 1. Schematic of relationship of forces acting on a hydrogen atom transported by dislocation (see designations in the text)

*The study was performed under the leadership of Prof. I.K. Pokhodnya.

related to the effect of small concentrations of hydrogen ($< 10 \text{ cm}^3/100 \text{ g}$) on mechanical properties and performance of a welded joint, and promotes formation of cold cracks.

Behaviour of an embryo sub-microcrack that interacts with hydrogen is a key point in the mechanism of EHB. Here the main role is played by dislocations [2], the movement of which is an elementary event of plastic deformation leading to formation of the sub-microcrack and, at the same time, an efficient method for transportation of hydrogen into its bulk. An experimental study of this process involves much difficulties, which makes it necessary to use numerical methods.

Description of the transportation of hydrogen with edge dislocations allows for the following components of the process: interaction of hydrogen with dislocations; interaction of hydrogen atoms moving at a constant speed with the crystalline lattice; and interaction of hydrogen atoms between each other.

Place the origin of co-ordinates to the centre of a uniformly moving edge dislocation (Figure 1). The hydrogen atom transported with the dislocation is affected by the force of interaction with the edge dislocation and force of resistance to this movement by the crystalline lattice of metal. The Cottrell equation [3] in polar (1) and Cartesian (1a) co-ordinates was used to determine the potential energy of interaction of hydrogen with the edge dislocation, u_d :

$$u_d = \frac{A \sin \alpha}{r}, \quad (1)$$

$$u_d = -\frac{Ay}{x^2 + y^2}, \quad (1a)$$

where A is the constant equal to $A = Eb$; E is the mean energy of interaction of a hydrogen atom with the dislocation, which is determined experimentally; b is the modulus of the Burgers vector; and r is the absolute value of the vector radius.

Let the edge dislocation move along axis X in a negative direction at speed v_0 (see Figure 1). The hydrogen atom moving with it is affected by the force of resistance, F_t , of the crystalline lattice. The value of force F_t was estimated using the Einstein relationship for a brownian particle:



$$F_t = \frac{kTv_0}{D}, \quad (2)$$

where k is the Boltzmann constant; T is the absolute temperature; and D is the diffusion coefficient.

Hence, the potential energy of a transported hydrogen atom is equal to

$$U = u_d - F_t x + u_0 = -\frac{A \sin \alpha}{r} - F_t r \cos \alpha + u_0, \quad (3)$$

where u_0 is the constant set from the edge conditions.

Equation (3) describes interaction of a hydrogen atom with the dislocation that transports it and a crystalline lattice. Now the problem of finding the amount of hydrogen transported with the dislocation is reduced to finding edge conditions: the boundary (geometric size, shape) of a hydrogen cloud, and the concentration of hydrogen at the hydrogen cloud-free hydrogen interface.

Find the points where resistance force F_t is equal to component F_x of the force with which the dislocation affects the hydrogen atom along axis X :

$$F_x = -\frac{\partial u_d}{\partial x} = -\frac{A \, 2xy}{(x^2 + y^2)^2} = -\frac{A \sin 2\alpha}{r^2}. \quad (4)$$

Equating F_x to F_t yields

$$\frac{A \sin 2\alpha}{r^2} = F_t, \quad (5)$$

$$r = \sqrt{\frac{A}{F_t} \sin 2\alpha}. \quad (6)$$

The basic form of the curve is shown in Figure 1. Tangential to curve (6) is parallel to axis X at points M ($\pi/3$) and H ($4\pi/3$), and parallel to axis Y at points N ($\pi/6$) and G ($7\pi/6$). To the right from curve ONM , $F_x < F_t$ and the dislocation cannot transport hydrogen from this region. $F_x > F_t$ inside region $ONMO$. An external force is generated, which can be balanced only if curve $ONMO$ carries ahead of it some extra amount of hydrogen. Curve $OGHO$ will «sweep» hydrogen: atoms located below point G will envelope the dislocation, and those located above this point will get into the hydrogen cloud (the probability of location of the hydrogen atom inside curve $OGHO$ is neglected).

If the effect exerted by a counter flow of hydrogen is neglected, it is possible to show that for the hydrogen cloud to be in equilibrium with external forces, the boundary of this cloud should lie on a closed equipotential curve. Therefore, the hydrogen cloud will touch curve ONM at some point K , where the potential energy U has a minimal value. By substituting (6) to (3) and taking a derivative, we find that $U_{\min} = -\sqrt{2AF_t}$ at angle $\alpha = \pi/4$. Then the boundary of the hydrogen cloud can be described by the following equation (Figure 2):

$$\frac{A \sin \alpha}{r} + F_t r \cos \alpha - \sqrt{2AF_t} = 0, \quad (7)$$

and equation (3) will have the following form:

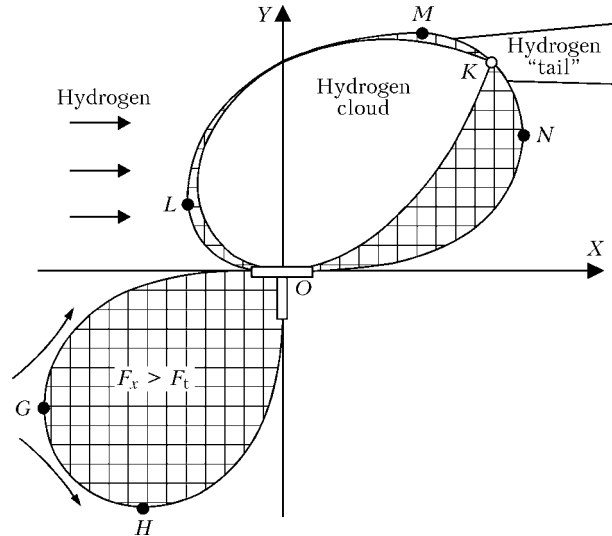


Figure 2. Schematic of interaction of hydrogen with moving dislocation (the reference system is related to the dislocation)

$$U = \frac{A \sin \alpha}{r} - F_t r \cos \alpha + \sqrt{2AF_t}. \quad (8)$$

Equation (7) will describe the shape of the hydrogen cloud in a case if we neglect the counter flow of hydrogen. However, after the process becomes steady, the entire amount of hydrogen carried into the cloud with the counter flow should go out of it. Hence, the cloud boundary should twice intersect curve ONM in a region of point K . To determine the maximal size of the cloud for each point $(x_0; y_0) \in ONM$, let us find point $(x_0; y_0)$ with the same potential:

$$\frac{Ay_0}{x^2 + y_0^2} + F_t x = \frac{Ay_0}{x_0^2 + y_0^2} + F_t x_0. \quad (9)$$

Solving equation (9) yields

$$x = -r \frac{\cos 2\alpha}{2 \cos \alpha} = -\sqrt{\frac{A}{F_t} \sin 2\alpha} \frac{\cos 2\alpha}{2 \cos \alpha}, \quad (10)$$

where $\alpha = \arctg(y_0/x_0)$ and $\alpha \in [0, \pi/3]$.

Plot curve OLM (Figure 2) by using the solution obtained. Region $ONMLO$ is somewhat bigger than region confined by equation (4).

As the value of potential energy U at point K is minimal, the vicinity of this point is the most favourable region for an outflow of excessive hydrogen. Therefore, a hydrogen «tail» is formed at this point behind the dislocation.

The character of interaction of hydrogen atoms between each other can be described by statistics used for the calculations. If the interaction of atoms can be ignored in the problem, the Boltzmann statistics is used to calculate concentration C :

$$C = C_0 \exp(-U/kT), \quad (11)$$

where C_0 is the atomic content of free hydrogen at the point where $U = 0$.

It can be seen from equation (11) that concentration $C \rightarrow +\infty$ at $U \rightarrow -\infty$. However, the edge dislocation cannot transport an infinite amount of hydro-

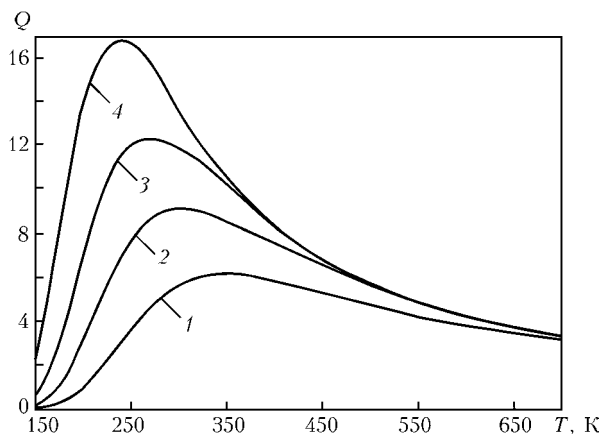


Figure 3. Quantity of hydrogen atoms, Q , transported with a unit length of edge dislocation depending upon the temperature of a specimen, T , at different velocities of the dislocation: 1 — $v_0 = 0.1$; 2 — 0.02; 3 — 0.005; 4 — 0.001 m/s

gen. Therefore, the Boltzmann statistics (11) is inapplicable to this problem.

Assume that one interstice in the crystalline lattice of iron can be occupied only by one hydrogen atom. This requirement is formally equivalent to the Pauli principle in quantum mechanics, which substantiates the possibility of using the Fermi–Dirac statistics to calculate the concentration of hydrogen [3]. Hence, the concentration of hydrogen atoms inside the cloud can be expressed by the following equation [4]:

$$C = \frac{C_0 f_u}{1 - C_0 + C_0 f_u} \quad (12)$$

where $f_u = \exp(-U/kT)$.

Integration of equation (12) yields the amount of hydrogen transported by a unit length of the edge dislocation equal to the Burgers vector:

$$Q = \frac{2}{b^2} \iint_{\Omega} C dx dy, \quad (13)$$

where Ω is the region occupied by the hydrogen cloud.

The following characteristics of metal: $b = 2.56 \cdot 10^{-10}$ m and $E = 0.6$ eV [5], were used to calculate the amount of hydrogen transported with a dislocation length equal to the modulus of the Burgers vector. The relative concentration of free hydrogen was assumed to be equal to $C = 2.5 \cdot 10^{-4}$ (approximately 5 cm³/100 g), and the concentration of hydrogen at the hydrogen cloud boundary was estimated from the law of conservation of mass. The distance at which the dislocation still affects the hydrogen atom was limited to forty Burgers vectors. The coefficient of diffusion of hydrogen was estimated from the following equation [6]: $D = 1.6 \cdot 10^{-7} \exp\left(-\frac{19640}{RT}\right)$, m²/s.

Figure 3 shows the results of calculations of the amount of hydrogen, Q , transported by a unit length of the edge dislocation depending upon the temperature of a specimen, T , for different dislocation velocities v_0 . The calculation results obtained can be explained by a complex character of interaction of hy-

drogen with the edge dislocation. The concentration of hydrogen about a quiescent edge dislocation grows at low temperatures, but resistance force F_t acting on the hydrogen atom being transported also grows because of a low coefficient of diffusion of hydrogen. Therefore, almost all the hydrogen cloud detaches from the edge dislocation under the effect of force F_t during movement, and this dislocation becomes capable of transporting a relatively small amount of hydrogen. Resistance force F_t decreases with increase in temperature. So, other conditions being equal, the edge dislocation transports more hydrogen. At a temperature close to the normal one, the amount of hydrogen transported with the edge dislocation reaches its maximum (Figure 3, curves 1 and 2). Further increase in temperature leads to a fall of the concentration of hydrogen about the edge dislocation because of thermal movement of hydrogen atoms. Thus, the amount of hydrogen transported to the regions of increased temperatures decreases. According to study [2], RHB of metal occurs providing that the dislocations carry a sufficient amount of hydrogen to the sub-microcrack. Temperatures close to the normal one are the most favourable temperature range, which agrees with the calculated temperature dependence for the transportation of hydrogen with an edge dislocation.

In addition to temperature, the amount of the transported hydrogen is also affected by the velocity of the edge dislocation. According to the results obtained, decrease in velocity v_0 is accompanied by increase in the amount of the transported hydrogen, and maximum of the dependence moves to a range of lower temperatures (Figure 3, curves 3 and 4). The velocity of the edge dislocation, v_0 , is proportional to a relative rate of metal strain, $\dot{\epsilon}$ [3]. Therefore, as follows from the calculations, decrease of the latter leads to increase of the degree of RHB and shift of the peak of the hydrogen induced brittleness to a range of lower temperatures. If the value of $\dot{\epsilon}$ is sufficiently high, the amount of the transported hydrogen substantially decreases. In this case, the reversible hydrogen brittleness of metal may not show up at all. The data obtained correlate with the experimental results [1, 3, 7].

It should be noted in conclusion that the model suggested is in good agreement with the experimental data. Application of this model will make it easier to predict a hydrogen-induced brittle fracture of welded joints in structural steels.

1. Pokhodnya, I.K., Shvachko, V.I. (1997) Physical nature of hydrogen-induced cold cracks in welded joints of structural steels. *Avtomatich. Svarka*, **5**, 3–12.
2. Pokhodnya, I.K., Shvachko, V.I. (2001) Nature of hydrogen brittleness of structural steels. *Fiziko-Khimich. Mekhanika Materialiv*, **2**, 87–96.
3. Kolachev, B.A. (1985) *Hydrogen brittleness of metals*. Moscow: Metallurgiya.
4. Hirth, J.P., Carnahan, B. (1978) Hydrogen adsorption at dislocations and cracks in Fe. *Acta Met.*, **26**, 1795–1803.
5. Meshkov, Yu.Ya., Pakharenko, G.A. (1985) *Structure of metal and brittleness of steel products*. Kiev: Naukova Dumka.
6. Boellinghaus, Th., Hoffmeister, H., Middel, C. (1995) Scatterbands for hydrogen diffusion coefficients in low and high alloyed steels with an austenite decomposition microstructure and high alloyed steels with an austenitic microstructure at room-temperature. *IIW Doc. IX-1812*.
7. Pokhodnya, I.K., Stepanyuk, S.N., Shvachko, V.I. (2000) Role of temperature in hydrogen-induced cracking of structural steels and welded joints. *The Paton Welding J.*, **2**, 2–7.



CORROSION RESISTANCE OF THERMAL SPRAY COATINGS OF QUASI-CRYSTALLINE PHASE-CONTAINING AlCuFe BASE ALLOYS

Yu.S. BORISOV, A.L. BORISOVA, V.F. GOLNIK and Z.G. IPATOVA
E.O. Paton Electric Welding Institute, NASU, Kiev, Ukraine

Corrosion resistance of detonation and plasma coatings of AlCuFe base powders alloyed with scandium, chromium and a set of elements Ti, Cr and Si in 0.1 n KOH solution, 0.1 n HCl solution and synthetic sea water was studied by the potentiostatic method. Dependence of electrochemical properties (potential and electrochemical rate of corrosion) of the coatings upon their spraying method, compositions and quasi-crystalline phase content was determined.

Keywords: thermal spray coatings, quasi-crystalline phase, Al-Cu-Fe system alloy, corrosion properties

After publication in 1984 of the first study dedicated to quasi-crystals, the focus of researchers was on revealing their nature (atomic structure) and investigation of magnetic, electric and mechanical properties, as well as dynamics of the lattice. The issues of technical application of quasi-crystalline materials require an in-depth study of such a characteristic as corrosion resistance in different aggressive environments. Because of their high brittleness, such materials are applied mostly in the form of thin films or coatings.

Information on corrosion resistance of coatings containing the quasi-crystalline phase is limited and covers alloys of the Al-Cu-Fe and Al-Ce-Fe-Cr systems [1-6] (these investigations were conducted with the aim to use them for the manufacture of kitchenware). For example, study [1] showed a high corrosion resistance of alloys containing the quasi-crystalline phase in 0.1 n NaOH solution with pH 13. Alloys Al₆₅Cu₂₀Fe₁₅ with 80 % of the icosahedral ψ -phase, Al₇₀Cu₉Fe_{10.5}Cr_{10.5} with orthorhombic approximant of the decagonal phase, and Al₇Cu₂Fe with the crystalline phase are superior in corrosion resistance to aluminium. In addition, the chromium-containing alloy, whose corrosion rate is more than three orders of magnitude lower compared with aluminium, has the highest corrosion resistance.

Corrosion resistance of plasma coatings of alloy Al₇₁Cu₈Fe_{10.5}Cr_{10.5} was studied by electrochemical methods at the direct and alternating currents in 4 % solution of acetic acid with an addition of 0.5 M Na₂SO₄ at a temperature of 95 °C [2, 4]. It turned out that spray coatings were somewhat inferior in corrosion resistance to cast alloys of the same composition. However, additional annealing of the spray coatings at a temperature of 830 °C for 20 min led to a substantial increase in their corrosion resistance. It is the opinion of the authors that this is related both to increase in density of a coating and to formation of the decagonal phase, which is more corrosion-resistant than the initial icosahedral phase. On the other hand, considerable difference of β - and λ -phases from the crystalline and approximant phases causes gal-

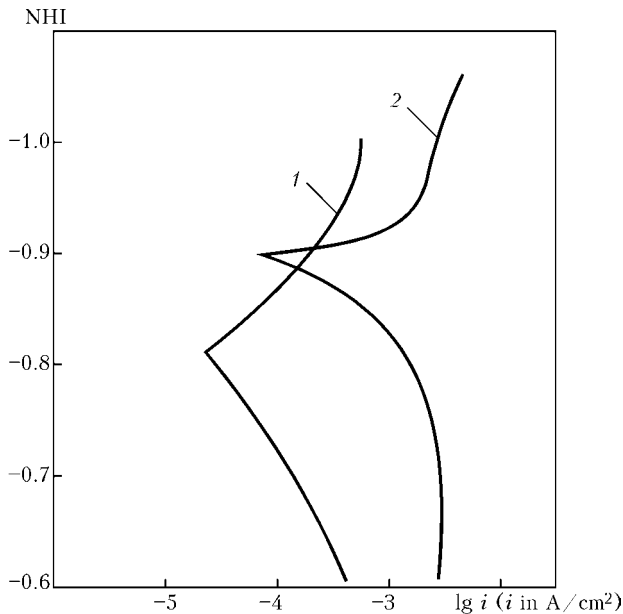
vanic effects to occur at interfaces between the phases and, accordingly, deteriorates corrosion resistance.

Study [3] gives results of investigations into behaviour of quasi-crystalline alloys Al₆₃Cu₂₅Fe₁₂ in alkaline and acid solutions at the values of hydrogen ion exponent pH ranging from 0 to 13, compared with different crystalline phases AlCuFe. Results of investigations of pitting corrosion on the surface of Al-Cu-Fe system alloys of different chemical compositions (β -, λ -, ψ - and ω -phases) are given in study [5]. The data on corrosion behaviour of quasi-crystalline approximant phases in the Al-Cu-Fe-Cr and Al-Cr-Fe systems, compared with stainless steel, are given in [6].

This study was conducted to investigate corrosion resistance of plasma and detonation coatings of Al-Cu-Fe (Al₆₅Cu₂₅Fe₁₂) system unalloyed powders, of unalloyed powders of the Al-Cu-Fe (Al₆₃Cu₂₅Fe₁₂) system alloy, the powders of the alloy with an addition of scandium (0.265 and 0.44 at.% Sc) and chromium (8 at.% Cr), and multicomponent alloys of the Al-Cu-Fe-TiCrSi systems with an addition of 5, 15 and 25 at.% of the second component in 0.1 n KOH solution, 0.1 n HCl solution, and synthetic sea water.

Powders for the deposition of coatings were produced at the E.O. Paton Electric Welding Institute by argon atomisation of the melt, and at the Institute for Materials Science Problems of the NAS of Ukraine by high-pressure water atomisation of the melt. Detonation coatings produced by the method of detonation spraying (DS) were deposited using the «Perun-S» unit under the following process conditions: flow rate of working gases, m³/h: 0.35 (propane-butane), 0.95 (oxygen) and 0.4 (air); spraying distance --- 110 mm. Particles of the powder were 40-63 μ m in size. Plasma coatings produced by the method of plasma spraying (PS) were deposited using the «Kiev-7» unit under the following process parameters: current 200 A, voltage 330 V, spraying distance 200 mm, and plasma gas (air) flow rate 25 m³/h. Particles of the powder were 40-63 or 25-40 μ m in size. The coatings were applied to the substrate having a room temperature and preheated to 270 °C. Thickness of the coatings was measured with a micrometer.

Electrochemical behaviour and corrosion resistance of thermal spray coatings were studied by the poten-



Potentiostatic curves characterising corrosion of plasma (1) and detonation (2) coatings $Al_{63}Cu_{25}Fe_{12}$ (36 % of ψ -phase) in 0.1 n KOH solution

tiostatic method using a specially designed pressure cell, which provided the one-sided access of electrolyte to a coating and required no protection of non-working surfaces, as is the case of using standard cell YaSE-2 that is part of a set of potentiostat P-5827 M.

Chlorine-silver electrode filled with a saturated solution of potassium chloride was used as a reference electrode, and platinum served as an auxiliary electrode.

Electrochemical rate and potential of corrosion of the coatings were determined using the graphical method on the basis of polarisation curves (Figure) by extrapolation of Tafel regions of the cathode and anode curves up to $E = E_{cor}$.

Characteristics of the coatings under investigation and their corrosion properties are given in Table 1.

The coatings under investigations differ in chemical and phase composition, including in content of the quasi-crystalline phase, the amount of which is lower, as a rule, than in the initial powder. Thus, an addition of scandium to the Al-Cu-Fe system quasi-crystalline alloy leads to increase in the ψ -phase content of the initial water-atomised powder (fraction from -63 to +40) from 53 to 72-73 wt.%, the detonation coating from 17 to 32-35 wt.%, and plasma coating from 36 to 38 wt.% (Nos. 2, 7, 8, 10 in Table 1).

In PS of the coatings using powder of the identical phase and particle size composition, a higher ψ -phase content of the coatings is characteristic of spraying on a preheated substrate (Nos. 4 and 5, Table 1).

Powders and coatings of the Al-Cu-Fe system alloy with a chromium addition contain a small amount of the ψ -phase, the main component with a quasi-crystalline structure in this system being approximant of the decagonal quasi-crystalline phase O_1 (No.9, Table 1).

Cubic 1/1 approximant of the icosahedral α -phase, the maximal content of which is achieved in a powder with 25 at.% of the second component, is formed in the AlCeFe-TiCrSi system alloys. The α -phase is a key phase in plasma and detonation coatings of this alloy.

Analysis of the results obtained (Table 1) proves that for all the investigated coatings, independently of their composition and spraying method, the maximal electrochemical corrosion rate takes place in alkaline solution, and the minimal one in sea water. That is, the rate of corrosion correlates with the solution pH value, and decreases in a range from low-acid to neutral solutions. It remains unchanged in a pH range from 6 to 8, and then increases with further increase in pH from 8 to 14. Therefore, the corrosion rate in 0.1 n HCl solution (pH 1) is higher than in neutral sea water (pH 8), and is still higher (pH 13) in alkaline solution than in both corrosive environments.

In all the electrolytes under investigation, the rate of corrosion of the Al-Cu-Fe, Al-Cu-Fe-Sc and Al-

Table 1. Electrochemical characteristics of thermal spray coatings containing quasi-crystalline (ψ , O_1) or approximant (α) phase

No.	Composition of spraying powder, at. %	Deposition method	$\dot{O}_s, \text{ }^\circ\text{N}$	Characteristics of powders		Phase content, wt. %	
				Production method	Particle size, μm	Powder	Coating
1	$Al_{63}Cu_{25}Fe_{12}$	DS	20	ArP	40-63	45 ψ	36 ψ
2	$Al_{63}Cu_{25}Fe_{12}$	DS	20	WP	40-63	53 ψ	17 ψ
3	$Al_{63}Cu_{25}Fe_{12}$	PS	270	ArP	25-40	50 ψ	36 ψ
4	$Al_{63}Cu_{25}Fe_{12}$	PS	20	ArP	40-63	45 ψ	36 ψ
5	$Al_{63}Cu_{25}Fe_{12}$	PS	270	ArP	40-63	45 ψ	45 ψ
6	$Al_{63}Cu_{25}Fe_{12}$	PS	20	ArP	40-63	45 ψ	36 ψ
7	$Al_{62.735}Cu_{25}Fe_{12}Sc_{0.265}$	DS	20	WP	40-63	72 ψ	35 ψ
8	$Al_{62.56}Cu_{25}Fe_{12}Sc_{0.44}$	DS	20	WP	40-63	73 ψ	32 ψ
9	$Al_{66}Cu_{18}Fe_8Cr_8$	DS	20	WP	40-63	42 O_1	37 O_1
10	$Al_{62.735}Cu_{25}Fe_{12}Sc_{0.265}$	PS	20	WP	40-63	72 ψ	38 ψ
11	$95Al_{63}Cu_{25}Fe_{12} + 5TiCrSi$	DS	20	WP	40-63	21 ψ	--
12	$85Al_{63}Cu_{25}Fe_{12} + 15TiCrSi$	DS	20	WP	40-63	69 α	$\alpha + AP$
13	$75Al_{63}Cu_{25}Fe_{12} + 25TiCrSi$	DS	20	WP	40-63	88 α	$\alpha + AP$

Note. ArP and WP --- argon and water atomised powder, respectively; AP --- amorphous phase.



Table 1 (cont.)

No.	Composition of spraying powder, at. %	Electrolyte					
		0.1 n KOH		0.1 n HCl		Sea water	
		\bar{A} , V	$i \cdot 10^5$, \bar{A}/cm^2	\bar{A} , V	$i \cdot 10^5$, \bar{A}/cm^2	\bar{A} , V	$i \cdot 10^5$, \bar{A}/cm^2
1	$\text{Al}_{63}\text{Cu}_{25}\text{Fe}_{12}$	-0.90	6.3	-0.38	3.0	-0.58	0.4
2	$\text{Al}_{63}\text{Cu}_{25}\text{Fe}_{12}$	-0.93	7.6	-0.34	5.0	-0.69	0.58
3	$\text{Al}_{63}\text{Cu}_{25}\text{Fe}_{12}$	-0.78	4.7	-0.44	2.3	-0.47	0.76
4	$\text{Al}_{63}\text{Cu}_{25}\text{Fe}_{12}$	-0.81	2.3	-0.46	2.1	-0.58	0.83
5	$\text{Al}_{63}\text{Cu}_{25}\text{Fe}_{12}$	-0.80	1.0	-0.40	0.63	-0.64	0.52
6	$\text{Al}_{63}\text{Cu}_{25}\text{Fe}_{12}$	-0.84	2.5	-0.44	2.1	-0.51	0.63
7	$\text{Al}_{62.735}\text{Cu}_{25}\text{Fe}_{12}\text{Sc}_{0.265}$	-0.90	4.0	-0.40	1.7	-0.59	1.4
8	$\text{Al}_{62.56}\text{Cu}_{25}\text{Fe}_{12}\text{Sc}_{0.44}$	-0.93	7.6	-0.32	3.9	-0.60	1.6
9	$\text{Al}_{66}\text{Cu}_{18}\text{Fe}_8\text{Cr}_8$	-0.88	1.3	-0.38	0.91	-0.50	0.76
10	$\text{Al}_{62.735}\text{Cu}_{25}\text{Fe}_{12}\text{Sc}_{0.265}$	-0.89	3.8	-0.38	1.5	-0.58	1.2
11	$95\text{Al}_{63}\text{Cu}_{25}\text{Fe}_{12} + 5\text{TiCrSi}$	-0.54	0.6	-0.35	0.57	-0.48	0.5
12	$85\text{Al}_{63}\text{Cu}_{25}\text{Fe}_{12} + 15\text{TiCrSi}$	-0.57	0.57	-0.35	0.55	-0.40	0.45
13	$75\text{Al}_{63}\text{Cu}_{25}\text{Fe}_{12} + 25\text{TiCrSi}$	-0.50	0.48	-0.35	0.46	-0.51	0.39

Cu-Fe-Cr system coatings, both plasma and detonation ones, depends upon the content of the quasi-crystalline phase in them: the higher the content of this phase, the lower the rate of corrosion. Thus, for the detonation coatings with 36 % of the ψ -phase, compared with 17 % (Nos. 1 and 2, Table 1), it is lower in KOH solution by a factor of 1.2, in HCl solution by a factor of 1.7, and in sea water by a factor of 1.4. The plasma coatings with 36 % of the ψ -phase in alkaline solution, hydrochloric acid solution and sea water are 5, 3 and 1.5 times less resistant, on the average, than coatings containing 45 % of the ψ -phase (Nos. 3, 4, 6, compared with No. 5, Table 1).

Comparison of the results of investigation into corrosion resistance of the coatings of unalloyed and alloyed powders produced under identical conditions shows that an addition of 0.265 at. % Sc to the Al-Cu-Fe system alloy increases corrosion resistance of the detonation coatings in alkaline and acid solutions, and decreases it to some extent in sea water (Nos. 1 and 7, Table 1). Adding 0.44 at. % Sc decreases corrosion resistance of the coatings in all the corrosive environments (Nos. 1 and 8, Table 1).

Alloying with chromium, like alloying with 0.265 at. % Sc, leads to increase of corrosion resistance in alkaline and acid solutions, and decrease of corrosion resistance in sea water (Nos. 1 and 9), the effect of chromium (8 at. %), compared with scandium (0.265 at. %), being more pronounced. For example, the coatings alloyed with chromium are superior in corrosion resistance to those alloyed with scandium: 3-6 times in KOH solution, 2-4 times in HCl solution, and 1.5-2 times in sea water, both being inferior in corrosion resistance in sea water to the unalloyed Al-Cu-Fe powder coatings.

Standard electrode potentials of scandium and chromium in aqueous solutions of the respective salts at a temperature of 25 °C are as follows: $\text{Sc}^{3+}/\text{Sc} = -2.077$ V, and $\text{Cr}^{3+}/\text{Cr} = -0.744$ V, i.e. scandium is located much

more to the left than chromium in a series of potentials, which means that it is less corrosion-resistant.

Effect of a spraying method on corrosion resistance of coatings is different in different environments. For example, in alkaline and acid solutions the plasma coatings of unalloyed powders are superior in corrosion resistance to the detonation ones, having the same ψ -phase content (Nos. 3, 4, 6, compared with No. 1). In sea water, the detonation coatings are more corrosion-resistant than the plasma ones. Comparison of corrosion resistance of the coatings of scandium-alloyed powders (Nos. 7 and 10) shows that the rate of corrosion of the plasma coatings is lower than that of the detonation ones in all corrosive environments.

The highest corrosion resistance in all solutions was exhibited by multicomponent detonation coatings of the Al-Cu-Fe-Ti-Cr-Si system (Nos. 11-13), electrochemical characteristics of these coatings being but slightly dependant on their chemical composition, although the rate of corrosion decreases to some extent with increase in the content of component TiCrSi.

Electrochemical process of corrosion of multicomponent coatings in electrolytes is of a very complex nature. It includes selective dissolution of different elements and formation of new phases on the surface, such as oxide phases, which can form a strong passivating film, depending on their structure. Electrochemical characteristics of the corrosion process depend both upon the corrosive environment and upon the characteristics of a coating itself (chemical and phase composition, imperfection of structure, porosity, etc.).

Effect of different elements on corrosion parameters can be explained to a certain extent by their physical-chemical characteristics, e.g. standard electrode potential and affinity for oxygen (Table 2).

Hence it follows, in particular, that scandium, being an electrically negative element, should increase the rate of corrosion, which is the case of an experiment with an addition of 0.44 at. % Sc to the alloy. At the



Table 2. Standard electrode potential, E^0 , and enthalpy of formation of oxides at 25 °C, ΔH [7]

Indicator	Al	Cu	Fe	Sc	Ti	Cr	Si
E^0 , V	-1.66	0.521	-0.44	-2.08	-1.628	-0.91	0.102
ΔH , kJ/mol	-1676	-173.2	-822.2	-1908.6	-1518	-1140.6	-910.9
Oxide	Al ₂ O ₃	Cu ₂ O	Fe ₂ O ₃	Sc ₂ O ₃	Ti ₂ O	Cr ₂ O ₃	SiO ₂

same time, dependence of corrosion characteristics upon the scandium content of a coating is not entirely unambiguous, as scandium may aggravate passivation of aluminium [8] under certain conditions. This is

likely to take place with an addition of a small amount of scandium (0.265 at.%).

Substantial decrease in the rate of corrosion of the coatings alloyed with chromium can be related to a

Table 3. Results of calculation of predicted service life of 500 µm thick thermal spray coatings based on Al-Cu-Fe system alloys in different corrosive environments

No.	Composition of spraying powder, at. %	Deposition method	Pycnometric density, g/cm ³	Electrolyte	Electrochemical corrosion rate, ×10 ² , mA/cm ²	Weight corrosion indicator, ×10 ² , g/(m ² ·h)	Depth corrosion indicator, ×10 ² , mm/year	Service life, years
1	Al ₆₃ Cu ₂₅ Fe ₁₂	DS	4.55	0.1 n ÊÎ Í	6.3	21.1	40.6	1.2
				0.1 n Í Cl	3.0	10.1	19.4	2.6
				Sea water	0.4	1.3	2.5	20.0
2	Al ₆₃ Cu ₂₅ Fe ₁₂	DS	4.33	0.1 n ÊÎ Í	7.6	25.5	51.6	0.9
				0.1 n Í Cl	5.0	16.8	34.0	1.5
				Sea water	0.58	1.9	3.8	13.2
3	Al ₆₃ Cu ₂₅ Fe ₁₂	PS	4.19	0.1 n ÊÎ Í	4.7	15.8	33.0	1.5
				0.1 n Í Cl	2.3	7.7	16.1	3.1
				Sea water	0.76	2.5	5.2	9.6
4	Al ₆₃ Cu ₂₅ Fe ₁₂	PS	4.21	0.1 n ÊÎ Í	2.3	7.7	16.0	3.1
				0.1 n Í Cl	2.1	7.0	14.6	3.4
				Sea water	0.83	2.8	5.8	8.6
5	Al ₆₃ Cu ₂₅ Fe ₁₂	PS	4.24	0.1 n ÊÎ Í	1.0	3.3	6.8	7.3
				0.1 n Í Cl	0.63	2.1	4.3	11.6
				Sea water	0.52	1.7	3.5	14.3
6	Al ₆₃ Cu ₂₅ Fe ₁₂	PS	4.30	0.1 n ÊÎ Í	2.5	8.4	17.1	2.9
				0.1 n Í Cl	2.1	7.0	14.2	3.5
				Sea water	0.63	2.1	4.3	11.6
7	Al _{62.735} Cu ₂₅ Fe ₁₂ Sc _{0.265}	DS	4.17	0.1 n ÊÎ Í	4.0	13.4	28.1	1.8
				0.1 n Í Cl	1.7	5.7	11.9	4.2
				Sea water	1.4	4.7	9.9	5.0
8	Al _{62.56} Cu ₂₅ Fe ₁₂ Sc _{0.44}	DS	4.12	0.1 n ÊÎ Í	7.6	25.5	54.2	0.9
				0.1 n Í Cl	3.9	13.1	27.8	1.8
				Sea water	1.6	5.4	11.5	4.3
9	Al ₆₆ Cu ₁₈ Fe ₈ Cr ₈	DS	4.31	0.1 n ÊÎ Í	1.3	4.4	8.9	5.6
				0.1 n Í Cl	0.91	3.0	6.1	8.2
				Sea water	0.76	2.5	5.1	9.8
10	Al _{62.735} Cu ₂₅ Fe ₁₂ Sc _{0.265}	PS	4.22	0.1 n ÊÎ Í	3.8	12.7	26.4	1.9
				0.1 n Í Cl	1.5	5.0	10.4	4.8
				Sea water	1.2	4.0	8.3	6.0
11	95Al ₆₃ Cu ₂₅ Fe ₁₂ + 5TiCrSi	DS	6.10*	0.1 n ÊÎ Í	0.6	2.0	2.9	17.3
				0.1 n Í Cl	0.57	1.9	2.8	17.9
				Sea water	0.5	1.7	2.5	20.2
12	85Al ₆₃ Cu ₂₅ Fe ₁₂ + 15TiCrSi	DS	6.01*	0.1 n ÊÎ Í	0.57	1.9	2.8	17.9
				0.1 n Í Cl	0.55	1.8	2.7	18.7
				Sea water	0.45	1.5	2.2	22.8
13	75Al ₆₃ Cu ₂₅ Fe ₁₂ + 25TiCrSi	DS	5.91*	0.1 n ÊÎ Í	0.48	1.6	2.4	21.0
				0.1 n Í Cl	0.46	1.5	2.3	21.9
				Sea water	0.39	1.3	1.9	26.0

* Apparent density.



higher value of standard potential of chromium, as well as, as noted by the authors of [2, 4, 6], to an increased corrosion resistance of the decagonal crystalline phase, compared with the icosahedral phase.

The data of Table 1 show that the coatings of powders of the AlCuFe–TiCrSi system alloys are by far superior in corrosion resistance in acid and alkaline solutions to all the rest of the coatings under investigations. Only in sea water the rates of corrosion of these coatings and coatings of the unalloyed powder are almost identical. Like in all the other cases, the most aggressive environment for the coatings of powders of the AlCuFe–TiCrSi system alloys is an alkaline solution (although the rates of corrosion in acid and alkaline solutions differ but slightly), and the least aggressive one is a sea water. Electrochemical characteristics of these coating are slightly dependent upon their chemical composition, although the rate of corrosion decreases a bit with increase in the TiCrSi content component. Increase in corrosion resistance of these coatings is most probably related to the effect of titanium and chromium, owing to their electrochemical characteristics, on the one hand, and to strength of oxides of these metals and resistance to pitting corrosion, on the other hand.

Other factors, such as roughness and degree of porosity of a coating, size and distribution of phases of a different chemical composition, length of interfaces, presence of residual internal stresses, etc., should also be taken into account, as noted in study [4].

The experimental data obtained allow a comparative evaluation of life of the investigated coatings of the same thickness in the corrosive environments under consideration. This evaluation was made on an assumption that aluminium in the form of ion Al^{3+} transfers to the solution in electrochemical corrosion of the AlCuFe base coatings.

According to studies [9, 10], quantitative estimation of the average electrochemical corrosion rate with time t can be performed using the weight loss indicator, which depends upon the corrosion current density:

$$w = \frac{Ai}{ZF}, \quad (1)$$

where w is the corrosion rate; A is the atomic weight of metal; i is the corrosion current density; Z is the valence of metal in a given corrosion process; and F is the Faraday constant.

If we assume that coatings are uniformly dissolved over the entire surface during the corrosion process, by substituting the $F = 96520$ A·s value to formula (1) we will obtain the following expression for the depth corrosion indicator \dot{I} (mm/year):

$$\dot{I} = \frac{8.76w}{\rho}, \quad (2)$$

where ρ is the coating density, g/cm³; and 8.76 is the conversion factor.

Results of calculation of the predicted service life of the investigated coatings through 500 μ m thickness are given in Table 3. As follows from the Table, the

coatings have a minimal service life in KOH alkaline solution, the lower limit of which for the detonation coatings of $Al_{63}Cu_{25}Fe_{12}$ with 17 % of the ψ -phase and of AlCuFe alloyed with 0.44 at.% Sc is 0.9 years (Nos. 2 and 8, Table 3). The upper limit (more than 20 years) relates to a multicomponent coating of $75Al_{63}Cu_{25}Fe_{12} + 25TiCrSi$ (No.13, Table 3).

The same situation holds also for the HCl solutions, where the minimal service life is 1.5 year for coating No.2, and maximal service life is about 21.9 years for coating No.13.

The minimal service life in sea water is 4.3 years for coating No.8, and maximal service life is 26 years for coating No.13.

It should be noted that the investigated coatings provide a reliable electrochemical protection for steel St.3 in all the electrolytes considered, and these coatings require no impregnation. The larger the difference between the corrosion potentials of a coating and St.3, the better the protection of this steel by the coating.

For instance, the range of corrosion potentials of the coatings in KOH solution is $-(0.50-0.93)$ V, whereas corrosion potential of St.3 in this electrolyte is -0.08 V. The difference between the coating and St.3 corrosion potential is $-(0.42-0.85)$ V.

For HCl, the range of corrosion potentials of the coatings is $-(0.32-0.46)$ V, whereas the corrosion potential of St.3 in this solution is -0.32 V, the difference being -0.14 V.

For sea water, the difference between the coating and St.3 corrosion potentials is $-(0.11-0.33)$ V.

Therefore, the efficiency of electrochemical protection of St.3 by the investigated coatings based on AlCuFe decreases as follows: KOH \rightarrow sea water \rightarrow HCl.

The authors are grateful to the Science and Technology Center in Ukraine for its financial support rendered to this study, which was completed under project 1630.

1. Dubois, J.M., Kanq, S.S., Massiani, Y. (1993) Application of quasicrystalline alloys to surface coating of soft metals. *J. Non-Crystalline Solids*, **153/154**, 443–445.
2. Massiani, Y., Ait-Yaazza, S. (1995) Electrochemical corrosion behaviour of quasicrystalline coatings in dilute acetic acid. In: *Proc. of 5th Int. Conf. on Quasicrystals* (Avignon, 22–26 May, 1995), 790–793.
3. Rudiger, A., Koster, U. (2000) Corrosion behavior of Al–Cu–Fe quasicrystals. *Mater. Sci. Eng.*, **294–296**, 890–893.
4. Dubois, J.M., Proner, A., Bucaille, B. et al. (1994) Quasicrystalline coatings with reduced adhesion for cookware. *Ann. Chem. Fr.*, **19**, 3–25.
5. Spurr, A.N., Pinhero, J.P., Sorderet, J.D. et al. (1999) Electrochemical pitting and repassivation on icosahedral Al–Cu–Fe, and a comparison with crystalline phases. *Mat. Res. Soc. Symp. Proc.*, Vol. 553, 275–280.
6. Veys, D., Rapin, C., Aranda, L. et al. (2004) Electrochemical behavior of approximant phases in the Al–(Cu)–Fe–Cr system. *J. Non-Crystalline Solids*, **11**, 1–10.
7. Rabinovich, V.A., Khavin, Z.Ya. (1977) *Concise chemical reference book*. Leningrad: Khimiya.
8. Vyazovikina, N., Milman, Yu., Sirko, A. (2002) New high-strength corrosion-resistant aluminium alloys. *Fiziko-Khimich. Mekhanika Materialov*, **3**, 554–558.
9. Zhuk, N.P. (1976) *Theoretical course of corrosion and protection of metals*. Moscow: Metallurgiya.
10. Keshe, G. (1984) *Corrosion of metals*. Moscow: Metallurgiya.



PECULIARITIES OF OUTFLOW OF TWO GAS FLOWS FROM NOZZLES OF WELDING TORCHES IN AUTOMATIC CONSUMABLE ELECTRODE WELDING

S.T. RIMSKY

E.O. Paton Electric Welding Institute, NASU, Kiev, Ukraine

Laser-interferometry and shadow methods were used to study structure and character of outflow of argon and carbon dioxide flows, simultaneously outflowing onto the flat barrier from the internal and external nozzles of flat configuration with different geometry of the channels. Optimal combinations of rates of the internal and external shielding gas flows and efficient designs of the torch nozzles were found. Design of the torch for welding under forced conditions in a double flow of shielding gases, ensuring efficient shielding of the welding zone from air at currents up to 900 A and low flow rates of argon and carbon dioxide, is suggested.

Keywords: arc welding, consumable electrode, shielding gases, gas flow rate, double-layer shielding, gas shielding efficiency, optical methods, forced conditions, porosity of welds, design of torches

It is difficult to ensure reliable shielding of the arc and molten metal zone against harmful action of air in gas-shielded consumable electrode welding under forced conditions. Since the time, when this method of welding was developed, many researchers studied outflow of the shielding gas jet from nozzles of welding torches for the purpose of choosing such optimal parameters of the gas jet outflow, which would ensure the best shielding properties [1–5]. Recommendations, developed as a result of these investigations, were designed for one flow of gas, outflowing from nozzles of welding torches of different designs.

In addition to welding in one gas flow, gets popular method of welding in a double flow (it is known in the European market under the name MAGCI process), consisting of two coaxially located gas jets [6]. In this case it is important to ensure minimal miscibility, because the arc must burn in central jet of the gas, which has certain useful technological properties. Parameters of central jet of the gas (for example, Ar or mixture of gases Ar + He) are selected in such way that their minimal flow rate be ensured in connection with their high cost. Flow rate of the gas, supplied into the external nozzle, may be several times higher than that of the gas, supplied into the central nozzle. This less expensive gas shields central jet and ensures additional shielding of the weld pool. Double-jet gas shielding allows reducing argon flow rate by 50–60 % [6].

In perfection of gas shielding in welding two main trends have been outlined: ensuring of a reliable gas shielding in welding under forced conditions at low flow rates of expensive gases; and application of the principles of gas shielding organization, different from the traditional ones, by developing perfect designs of the welding torches. Both trends deserve of serious attention and require for deep investigation concerning different conditions of welding.

Among methods of investigation of gas flow inhomogeneity, which allow studying complex double-layer shielding, consisting of oxidizing and neutral gases, widespread and basic are two optical methods, which add each other --- interference and shadow ones. Interference method allows getting direct distribution of densities, while shadow method allows determining density gradients of gas jets. Main advantages of optical investigation methods in comparison with other physical methods consist in the following:

- optical methods do not introduce outside excitations into the space being investigated and do not cause changes of physical and chemical properties of the environment;
- they have higher sensitivity and allow noting and measuring local temperature changes of air or other gases up to 0.1°, which is difficult to do in other methods;
- they make it possible to simultaneously investigate the whole space occupied by this phenomenon, and are irreplaceable for determining fields of temperatures and pressure of flows, flame, etc.;
- they may be successfully used for investigation of non-stationary, quickly passing processes (propagation of shock waves and flame front) due to absence of inertness.

Influence of different factors on efficiency of the complex (double-layer) gas shielding of a welding zone was investigated on a pilot installation, scheme of which is presented in Figure 1. The installation consists of a four-mirror interferometer (of Mach-Zehnder type) and shadow instrument (of Tepler type), a working section, cylinders with gases, and measuring instruments. The IT-14 interferometer may be used in the double-adjustment mode for producing interferograms and shadowgrams. In the first case the LG-36A quant generator was used as a light source, in the second case the DRSh-500 mercury quartz lamp of super-high pressure was used.

In the working section of the installation experimental extension (gas) nozzles, made from organic glass, with different configuration of channels were

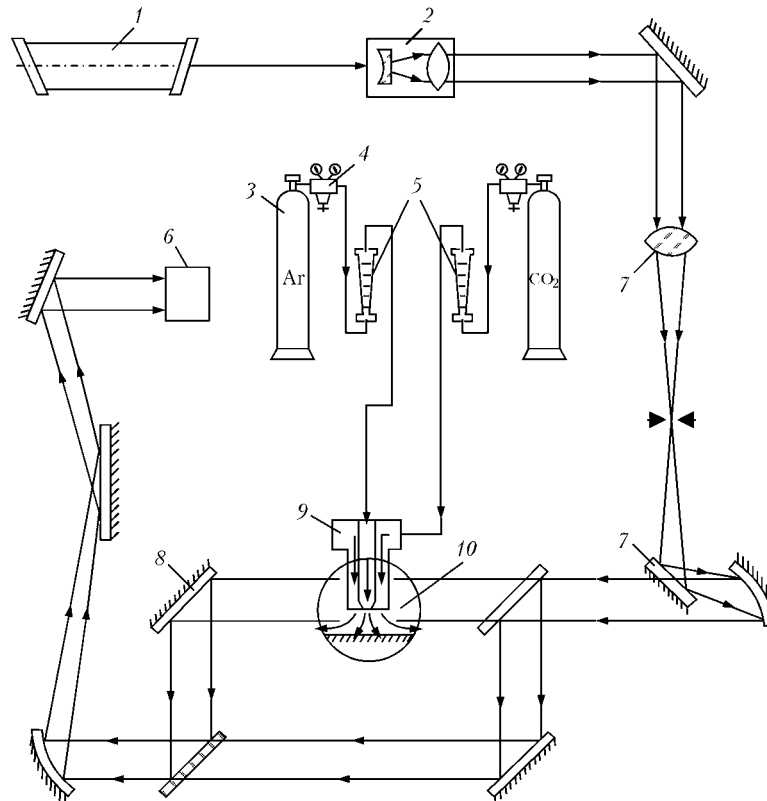


Figure 1. Scheme of pilot installation: 1 — laser; 2 — optical attachment; 3 — cylinders with gas; 4 — gas reducers; 5 — rotameters; 6 — receiving device; 7 — collimator; 8 — interference part of instrument; 9 — welding torch; 10 — optical window

located: two external channels for the carbon dioxide flow, and the internal one — for argon. Surfaces of the experimental extension nozzle channels had flat configuration. Extension nozzles were placed perpendicular to direction of the main light flow of the optical instrument, which allowed avoiding additional distortions of the flow structure on interference and shadow pictures. In the upper part the extension nozzles had a distribution head, which ensured receiving of two different gases and their directing into respective channels. Argon and carbon dioxide have different refraction factors, that's why they may be well distinguished in the receiving part of the interferometer. Inside the extension nozzles a special rod was installed, simulating a current-leading tip and a welding electrode. Distance from the lower edge of the extension nozzle to horizontal plane equaled 20 mm. Flow rate of the gases was determined by the RS-3 rotameters.

Investigation of the gas shielding efficiency was performed according to the complex methodology in two stages. At the first stage character of outflow of gas flows depending upon design peculiarities of the experimental extension nozzles (Figure 2) and change of argon and carbon dioxide flow rates were investigated by means of the IT-14 interferometer (all together 12 combinations of the shielding gas flow rates were tested) (Table). Argon was used as a determining factor in investigation of this design of the extension nozzle as the most useful and relatively expensive shielding gas in arc welding. Ratio of flow rates $CO_2:Ar$, determined by the K number, changed from 0.94 to 7.50 (see the Table).

On the basis of the optical test results working torches were manufactured with profiles of the extension nozzles, having the best gas-dynamic properties.

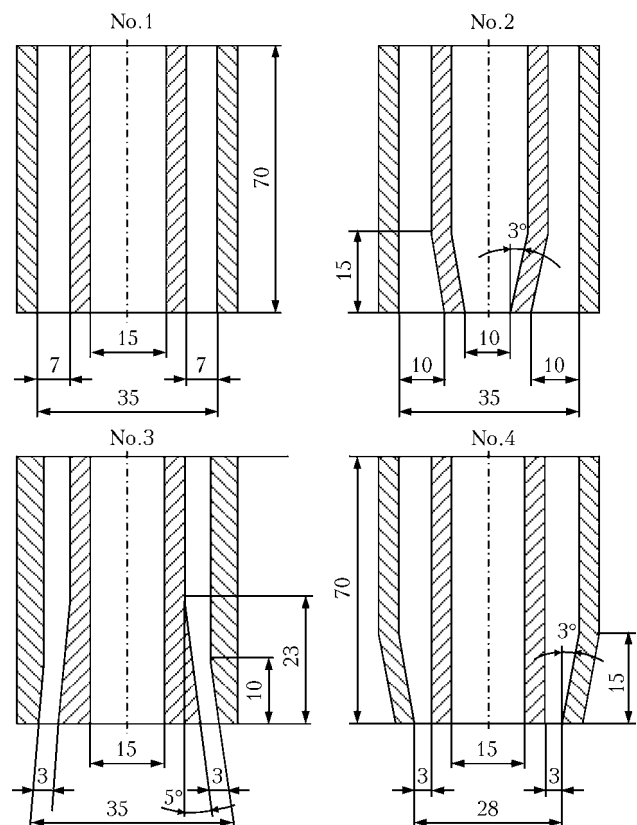


Figure 2. Scheme of experimental extension nozzles in section of 20 mm width: Nos. 1-4 — extension nozzle numbers

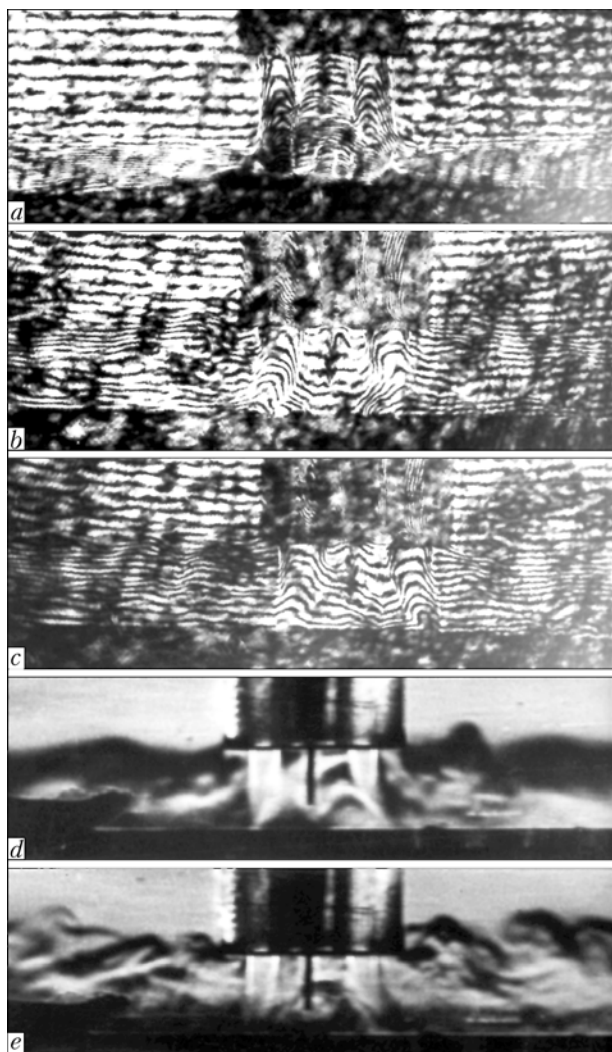


Figure 3. Interference (a-c) and shadow (d, e) patterns of outflow of Ar and CO₂ gas flows from experimental extension nozzle No.1 at different ratio of flow rates of gases: a, d — $K = 2.19$; b, e — $K = 3.19$; c — $K = 5.84$

At the second stage working torches of different design were tested under real welding conditions in comparison with widely used in the industry torch with a cylindrical nozzle. Deposition of beads on plates from steel VSt3sp (killed) was performed by welding wire Sv-08G2S of 2 mm diameter. In the experiments welding current force, gas flow rate and distance from the nozzle to the item being welded were changed. Efficiency of the gas shielding was estimated by the weld quality — presence of porosity and content of nitrogen in the weld metal. For determining porosity all welds were subjected to radiographic analysis. Content of nitrogen in the metal chips was determined by chemical analysis. Content of nitrogen in the steel and welding wire constitutes 0.007 and 0.012 wt.%, respectively. Such comprehensive method of estimating gas shielding efficiency of the welding zone is practically useful and the most accurate.

Application of flat models of welding torches (extension nozzles) in investigation of the gas shielding quality of the welding zone by means of the IT-14 interferometer made it possible to correctly present dynamic picture of interaction of two gas flows.

Flow rates of experimental mixtures of shielding gases

Flow rate, l/h		CO ₂ :Ar, number K
CO ₂	Ar	
300	120	2.50
500		4.16
700		5.84
900		7.50
300	220	1.36
500		2.27
700		3.19
900		4.09
300	320	0.94
500		1.56
700		2.19
900		2.81

The gas flow, escaping from the extension nozzle (Figures 3 and 4), meets on its way an obstacle in the form of a plane of the metals being welded. Obtained picture of sharp change of the movement direction of the gas jets, spreading of the latter over the obstacle surface, mutual mixing of argon and carbon dioxide, and their mixing with the ambient air environment confirm the fact that this complex gas-dynamic situation does not yield to the strict mathematical description. The most right way of investigating such processes is their visualization by means of optical instruments for getting interference and shadow patterns with their subsequent analysis and decoding.

Structure and characteristic peculiarities of the gas shielding zone with application of the experimental extension nozzle No.1 (see Figure 2) at various flow rates of argon and carbon dioxide may be seen in Figure 3. From presented interference and shadow patterns one may determine how structure of the gas shielding zone changes depending upon different variable factors. Complex character of interaction of two concomitant gas flows, which meet a flat obstacle, is seen. Boundaries of gas flows are clearly seen in the process of their outflow from the experimental extension nozzle. As gas jets move away from the outlet section, a noticeable turbulization and mutual mixing of the flows takes place. After achieving flat obstacle gas jets mix and spread over the surface, whereby the gas flow turns at 90° that causes further development of turbulence and active mixing of the flow with ambient air environment. With this kind of the extension nozzle, as flow rate of argon increases (Figure 3, a), zone of the space, occupied by this gas, increases too, and near surface of the obstacle carbon dioxide is displaced on the external side. As flow rate of carbon dioxide increases, zone, filled with argon, reduces (Figure 3, c), whereby stormy mixing of the gases takes place, and it is difficult to determine their boundaries. As flow rates of carbon dioxide and argon increase, the gas flows get more «resilient», but in this stormy interaction their boundaries on surface of the obstacle preserve, forming a stable flow of the gas mixture (Figure 3, a).

Of a certain interest is investigation of the character of outflow of the gas flows from the experimental nozzle No.3, which has internal profile of the contractor type (see Figure 2). On interference and shadow patterns (Figure 4) with application of the extension nozzle No.3 boundaries of the diverging carbon dioxide flow and spreading over the obstacle surface flow of the argon and carbon dioxide gas mixture are clearly seen. In case of using the contractor extension nozzle, general picture of outflow of the gas flows preserves like in direct profile of the extension nozzle No.1. However, in this case there are certain structure peculiarities of the gas flows, which consist in the following facts. In the contractor outflow of the gases the flow gets more «resilient» and stable at a comparatively big distance from outlet edge of the extension nozzle. Arrangement of interference strips along the flow of carbon dioxide indicates that in immediate proximity from the extension nozzle edge speed of the flow, and therefore its density, changes insignificantly over the jet section. As the flow moves forward, distortions of the interference strips increase (the strips extend), which proves significant deformation of the profile of the flow speeds, especially in the area of boundary with ambient environments (on one side --- with argon flows, on the other side --- with air environment), whereby it should be noted that carbon dioxide flow has a concomitant laminar boundary layer on its boundaries. Laminar envelope of a certain thickness surrounds the main turbulent core of the gas flow and acts as a shielding layer, while in case of application of the extension nozzle No.1 the shielding laminar layer gets thinner and disappears as ratio of the gas flow rates K increases (see Figure 3, a-c).

Presented in Figure 4 interference and shadow patterns prove that at comparatively low flow rates of argon and low flow rates of carbon dioxide it is possible to clearly track zone of each outflowing gas. As flow rate of argon increases (Figure 4, a, b), displacement of carbon dioxide on external side occurs, whereby directly under the extension nozzle thickness of general mixed layer of the gases near horizontal surface increases insignificantly in contrast to application of the extension nozzle No.1 (see Figure 3, a, b), when this layer of the gases gets thicker, loses its speed, and is intensively mixed with air. Zone boundaries of the used gases are well pronounced. By means of getting away from the welding zone the mixed gas flow has a sufficient resilience.

Carried out investigations of physical picture of the gas shielding zone made it possible to develop a number of recommendations, which allow selecting optimal conditions for argon and carbon dioxide flow rates and ensure efficient shielding of the arc against action of air.

At flow rates of argon, equal to 120, 220 and 320 l/h, it is necessary to maintain ratio K within the shaded area, shown in Figure 5. As ratio of flow rates of the gases K increases above the shaded area, quick destruction of argon flow by carbon dioxide occurs, the zone, filled by argon, reduces, and changes

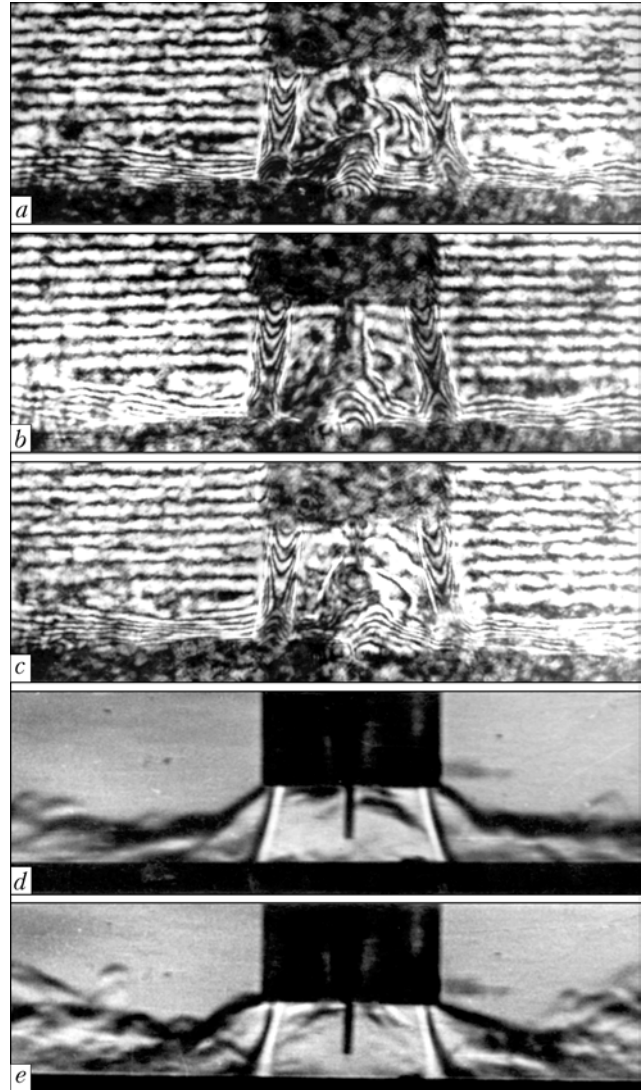


Figure 4. Interference (a-c) and shadow (d, e) patterns of outflow of Ar and CO₂ gas flows from experimental extension nozzle No.3 at different ratio of flow rates of gases: a, d --- $K = 2.19$; b, e --- 3.19; c --- 5.84

composition of the argon and carbon dioxide mixture in the arcing zone. In welding it may worsen stability of the arcing and cause other unfavorable phenomena of metallurgical and technological character.

In mechanized welding of steel by wire of 1.0--1.2 mm diameter low currents (≤ 350 A) are usually used, which allows ensuring good shielding of the welding zone against air. Application of forced conditions in automatic welding by wire of more than 1.6 mm diameter requires for perfect design of the nozzle and the very torch and ensuring of the quality shielding zone at the welding current up to 900 A and distance from the nozzle end to the item of 25--30 mm. For this purpose the gas jet should have sufficient rigidity and not to be destroyed by light draughts and movements of air, caused by the ventilation.

Design peculiarity of the welding torch, made according to profile of the contractor type extension nozzle No.3, is the fact that shielding flow of carbon dioxide is shifted from argon jet at a certain distance and at the instant of outflow from the nozzle does not

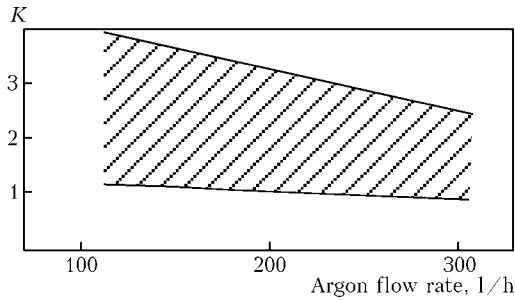


Figure 5. Area of efficient double-layer gas shielding depending upon ratio of flow rates K

contact with it. External annular flow of carbon dioxide, outflowing from the nozzle at a small angle to the electrode axis, plays part of a peculiar gas curtain around argon flow and at the same time shields the arc and the weld pool from air. By changing distance from the nozzle to the item and speeds of carbon dioxide and argon outflow it is possible regulate to a certain degree necessary composition of the gas mixture in the welding zone. Such structure of the double-layer gas shielding allows removing a number of shortcomings, peculiar to the welding process in one gas flow, for example in carbon dioxide or argon, and create other conditions for arcing or transfer of the electrode metal, achieving necessary welding-technological characteristics of the process. Such torch ensures reliable shielding of the welding zone at currents up to 900 A with good quality of welds.

It is known that welding torches with a cone or a cylindrical nozzle have narrow range of the gas flow rates, in case of deviation from which shielding jet of the gas gets turbulent and intensively mixes with air [4]. A shielding gas flow is subjected in welding to action of the arc discharge, especially of convective flows from the weld pool. In addition, process of the shielding gas mixing with air is effected by intensity and scale of turbulence [4]. These characteristics of the flow sharply increase at outlet from the nozzle and depend upon geometry of the nozzle profile and the gas flow rate. For equalizing the field of gas outflow speeds and reducing degree and scale of turbu-

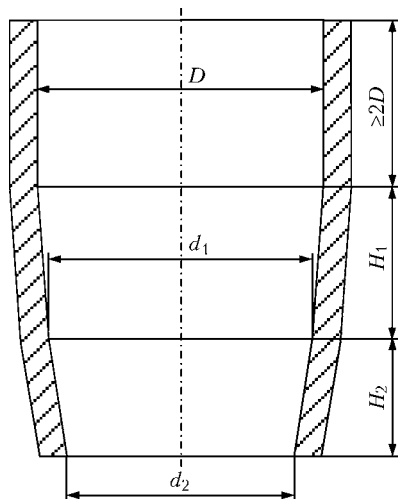


Figure 6. Scheme of double-cone nozzle for welding under forced conditions

lence the nozzles are used, which ensure compression of the gas flow [4, 7].

By means of the IT-14 interferometer character of outflow from cylindrical and double-cone nozzles was studied, using shadow method, at different flow rates of the shielding gas. The investigations showed that a nozzle-compressed gas flow is the most stable, when a double-cone nozzle is used [7]. Main geometric dimensions of a double-cone nozzle (Figure 6) are as follows: $d_1 = (0.75-0.95)D$, $d_2 = (0.50-0.90)D$, $H_1 = (0.65-0.80)D$, $H_2 = (0.50-0.70)D$, where d_1 is the circumference diameter of conjugation of the cones; d_2 is the outlet hole diameter of the lower cone; D is the diameter of the upper cone base; H_1 and H_2 are the heights of the upper and the lower cones.

From comparison of the shadow patterns one may get convinced that as the gas flow rate increases, the

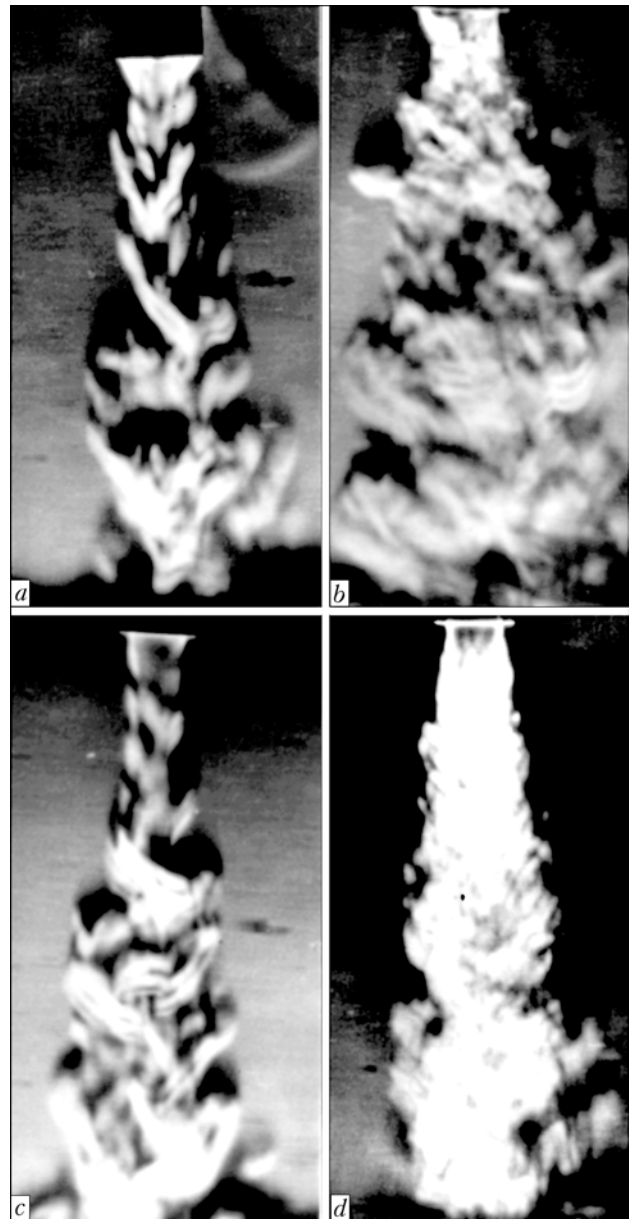


Figure 7. Character of shielding gas outflow from cylindrical (a, b) and double-cone (c, d) nozzles of welding torch depending upon flow rate of gas: a, c — 900; b, d — 1800 l/h (nozzle diameter is 22 mm)

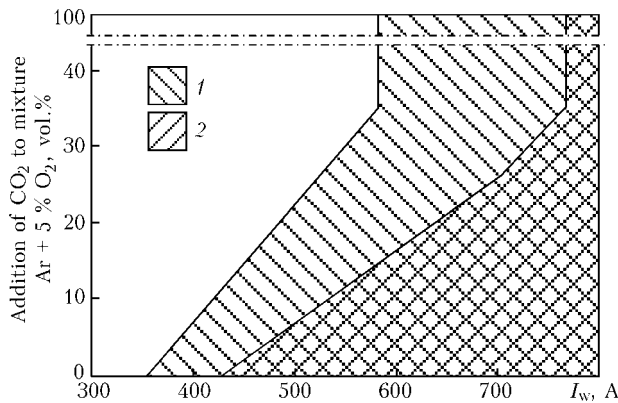


Figure 8. Influence of nozzle design on resistance of weld metal to formation of porosity depending upon composition of shielding gas and welding current: 1 — pores, cylindrical nozzle; 2 — pores, double-cone nozzle (gas flow rate is 1400 l/h)

jet, outflowing from the cylindrical nozzle (Figure 7, a, b), expands and gets turbulent, which causes its noticeable mixing with air. In case of using a double-cone nozzle increase of the gas flow rate increases rigidity of the jet (Figure 7, c, d) and ensures significantly larger length of the laminar section at outlet from the nozzle [7], whereby jet of the outflowing gas does not expand (Figure 7, c, d).

From the technological factors the biggest influence on quality of the welding zone shielding against air exert the gas flow rate, distance from the torch nozzle to the item being welded, value of the welding current, and design of the torch. Minimal necessary flow rate of the gas exists, which ensures under chosen conditions of the welding (design of the torch, the mode parameters, etc.) satisfactory shielding of the metal, being remelted by the arc, against air.

Influence of the nozzle design and the mixture composition Ar + O₂ + CO₂ on quality of the metal shielding against air in welding under forced conditions is presented in Figure 8. Significant reduction of the weld porosity is ensured by the double-cone nozzle and increase of carbon dioxide content in the triple mixture. The latter is stipulated by thermal expansion action of carbon dioxide and dissociation of the latter at the arc temperatures [8], and increase of oxidizing potential of the gas [9]. At high temperature it dissociates with increase of the volume, which allows under certain condition displacing air from the welding zone and thus improving quality of shielding. However, as prove experimental data (Figure 8), if content of CO₂ in the triple mixture exceeds 35 %, effect from dissociation of carbon dioxide is not reached. The main influence on resistance of the welds to formation of porosity, under other equal conditions, exert design of the nozzle and the welding current value.

In welding under forced conditions in two flows of gas with application of the torch, made according to profile of the nozzle No.3 (see Figure 2), as well as the torch with a double-cone nozzle (see Figure 6) significantly lower content of nitrogen in the welds is ensured (Figure 9) in comparison with widely use in the industry cylindrical nozzle. This allows performing multi-pass automatic welding with thick wire of carbon and low-alloy steels at currents up to 900 A with high quality of welds [10].

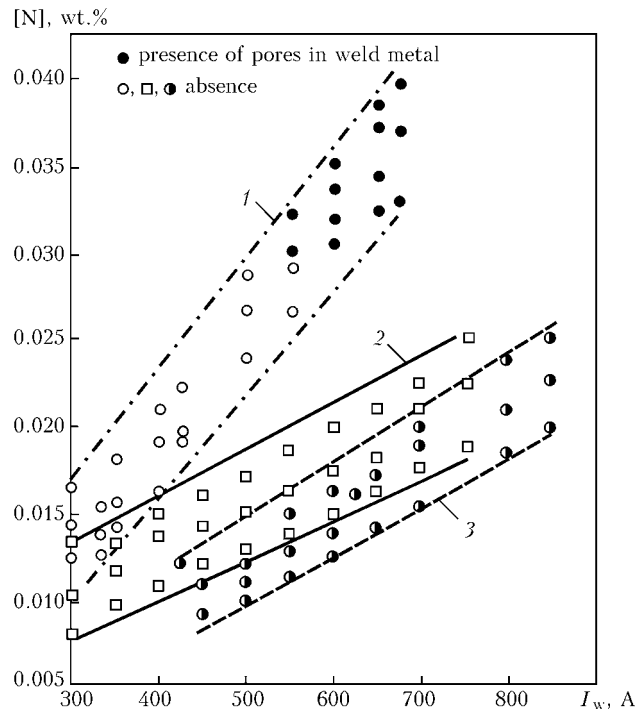


Figure 9. Influence of single- (1, 2) and double-layer (3) gas shielding on absorption of nitrogen by weld metal: 1, 2 — cylindrical and double-cone nozzle, respectively, with flow rate of gas (Ar + 5 % O₂ + 25 % CO₂) of 1600 l/h; 3 — torch for double-layer gas shielding with profile of nozzle No.3 (see Figure 2) at ratio of flow rates of gases $K = 2.81$

CONCLUSIONS

1. Physical picture of the gas shielding structure of two concomitant flows of argon and carbon dioxide, flowing onto a flat surface, is established by shadow and interference methods of investigation.
2. Obtained shadow and interference patterns of the double-layer gas shielding allowed determining optimal mode characteristics concerning flow rate of the bi-component flow for creation of the most favorable conditions for the shielding zone formation.
3. The version of the torch design and economical flow rate of the gases for welding at currents up to 900 A with high quality of the welds is established on the basis of analysis of gas-dynamic processes of outflow of two gas flows.

1. Ardentov, V.V., Fedorenko, G.A. (1973) On jet protection in gas-arc welding. *Svarochn. Proizvodstvo*, **1**, 3–5.
2. Bezbakh, D.K. (1969) Study of gas jets in gas-shielded welding. *Avtomatich. Svarka*, **6**, 3–32.
3. Petrov, A.V., Shtrikman, M.M. (1961) Study of shielded gas jet parameters in arc welding. *Svarochn. Proizvodstvo*, **5**, 5–8.
4. Starchenko, E.G., Lyubavsky, K.V. (1968) Influence of torch nozzle design on efficiency of gas shielding of welding zone. *Ibid.*, **11**, 13–16.
5. Kasatkin, B.S., Lobanov, L.M., Ivanova, O.N. et al. (1980) Investigation of shielding gas flows in welding torches using the holographic interferometry. *Avtomatich. Svarka*, **2**, 15–18.
6. (1982) MAGGI — a novel shielded arc welding process. *Metal Construction*, **10**, 550–553.
7. Rimsky, S.T., Svetsinsky, V.G., Ulianov, V.I. *Conical nozzle for welding torch*. USSR author's cert. 518299. Int. Cl. B 23 K 9/16. Publ. 25.06.76.
8. Novozhilov, N.M. (1979) *Principles of metallurgy of shielded-gas arc welding*. Moscow: Mashinostroenie.
9. Pidgaetsky, V.V. (1970) *Pores, inclusions and cracks in welds*. Kyiv: Tekhnika.
10. Svetsinsky, V.G., Rimsky, S.T. (1984) Welding of girth joints on multilayer pipes in shielded gas mixture Ar + O₂ + CO₂. In: *Proc. of All-Union Conf. on Multilayer Welded Structures and Pipes*. Kiev: Naukova Dumka, 177–182.



IMPROVEMENT OF WELDED JOINT STRUCTURE UNDER THE IMPACT OF WIDEBAND ULTRASONIC VIBRATIONS DURING WELDING

V.I. KIRIAN¹, A.A. KAJDALOV¹, D.P. NOVIKOVA¹, I.L. BOGAJCHUK¹ and M. KESNERS²

¹E.O. Paton Electric Welding Institute, NASU, Kiev, Ukraine

²«Aplis», Riga, Latvia

Problems of ultrasonic elastic vibration influence on materials are discussed. Treatment of a welded item by ultrasonic vibrations in a wide frequency band is proposed. Possibility of formation of a more fine-grained structure as a result of such treatment both in the weld metal and HAZ in arc welding of ordinary carbon steel St3sp is shown.

Keywords: arc welding, ultrasonic vibration impact, solidification, weld, HAZ, residual stresses, metal structure

Welded joints are usually characterized by a coarse-grained weld metal structure formed at a comparatively slow cooling of the weld pool, and presence of residual stresses creating a risk of distortion and cracking. The purpose of the work consists in studying the metal structure of a welded joint exposed to wide band ultrasonic vibrations during weld formation. It is known that the more solidification centers form in the metal and the lower the linear speed of crystal growth, the more fine-grained will the metal structure be. The solidification process depends on the temperature field, as well as the impact of alternating pressure due to propagation of an elastic acoustic wave of the audio and ultrasonic range in the melt. According to the traditional concepts, weak fields of ultrasonic impact should not have any noticeable influence on viscosity or other kinetic properties of the liquid. If the field energy recalculated for an atom is by several orders of magnitude lower than thermal energy kT (where k is the Boltzmann constant, T is the absolute temperature), it will not have any noticeable influence on elementary acts of the transfer processes. It is obvious that such fields do not influence the viscosity of gases or simple liquids, but in granular structures they may influence the displacement of grain boundaries. At ultrasonic treatment of the melt, refinement or fracture, as well as deformation of structural formations in the liquid take place. In addition, the main physico-chemical properties of the metal melts are changed, namely viscosity, surface tension on the melt–solid phase boundary, temperature distribution, diffusion and degassing processes, and capillary effect. The produced solid metal is even more fine-grained, if the melt was «sounded» before solidification.

A large number of studies have been conducted in the laboratory by now [1–4], which revealed the effects of elastic vibration impact on the material. However, their practical application is slowed down by the absence of highly-efficient equipment and methods of monitoring the acoustic parameters at application

of vibrations to the item. The mechanism of ultrasonic waves breaking up the structural objects in the melt or «quasimolecules» of FeSi type compounds is unclear, so that many technological processes of ultrasonic impact are still insufficiently developed. At present only ultrasonic cleaning, cutting and welding are used on the industrial scale.

At treatment of the weld pool by powerful elastic mechanical vibrations (power density of more than 1 W/cm^2) of the audio and ultrasonic range, the melt is usually «sounded» on one fixed frequency through the filler wire by a special tool or using item vibration. To lower the residual stresses the welded structure can be subjected to treatment by elastic vibrations after welding.

In individual cases the frequency of elastic vibrations («sounding») applied for welded structure treatment, is selected to be equal to one of the resonance frequencies of this structure. However, frequencies far from the resonance are more often used. On the other hand, the resonance ensures a greater amplitude of vibrations at a low consumed energy, this being highly important for large-sized items. Depending on the properties of «sounded» metal, the energy required for excitation of vibrations of a certain magnitude at resonance and outside it, can differ by several orders of magnitude. This difference is characterized by quality factor Q of the oscillatory system, which shows how many times the amplitude of forced vibrations at resonance exceeds the amplitude outside the resonance at the same excitation power. The quality factor values are different for different metals. On average, steels have $Q = 8000$, titanium alloys 21000, copper 6300, brass 13000, aluminium alloys 10000.

At higher temperature the quality factor is essentially lower, and it increases at cooling. However, even at elevated temperatures Q value is equal from several hundred up to several thousand, depending on the metal properties. The resonance frequency also changes at the change of temperature and crystalline structure. To achieve a constant treatment amplitude, the treatment frequency should follow the variations



of the resonance frequency. The structure (part) of a rather complex shape has numerous resonances with different frequencies. Parts usually consist of a number of elementary geometrical figures connected to each other, in which different types of elastic vibrations develop (Figure 1). In addition to the main types, also torsional vibrations, higher harmonics vibrations, etc. are possible. In complex-shaped parts these vibrations will proceed simultaneously, and their parameters can change, depending on the condition of the part and external conditions both by frequency and by amplitude. At excitation of elastic vibrations only in one of these frequencies (even if all the resonance changes are precisely followed) part vibrations will run only in one direction. Influence on the processes occurring in the item, will be limited, and not all of its parts will be subjected to treatment. All the processes in these item will occur spontaneously, and the final result of ultrasonic treatment will be unpredictable.

Thus, in order to treat all the sections of the item being welded in the same way, it is necessary to excite elastic vibrations in a broad frequency spectrum. Ideally, it is, probably, necessary to induce «white noise» with an infinite frequency spectrum.

At wideband ultrasonic treatment of the welded item elastic resonance vibrations will be excited in all of its parts, which will be transferred to the weld pool by each individual part of the item. The pool develops an oscillatory process with a broad frequency spectrum. The parameters of this process will change all the time, as the rigid structure configuration changes as a result of successive welding of individual sections, this leading to a change of resonance frequencies. In this case, the pool will not form stagnant zones of high-pressure and rarefaction, leading to a non-uniformity of the solidification process. «Mixing» of the frequency spectrum in the pool will occur, this creating the conditions for a uniform solidification of the melt and formation of a fine-crystalline structure of the weld metal. The same structural transformations proceed in the HAZ metal around the weld pool, and the fine-grained metal structure should also form there under the conditions of «sounding» at cooling.

Experimental investigations were conducted under the conditions of arc welding of plates of $125 \times 298 \times 6$ mm size from St3sp steel (killed). Welding was performed using Oerlikon special electrodes (E382B12H10 and EN499 type). Weld 1 was made with 2.5 mm electrode at welding current of 50–55 A, weld 2 — with electrode of 3.25 mm diameter at 75–80 A current. Each weld of 50 mm length was made in two passes, and then, to avoid the influence of subsequent manipulations, the welded section of the sample was cut off. Weld 1 was made without ultrasonic treatment, and the welded section was cut off after complete cooling in air. Welds 2 and 3 were made with application of wideband ultrasonic vibrations from a specially developed generator (Figure 2). Ultrasonic treatment was interrupted for the time of

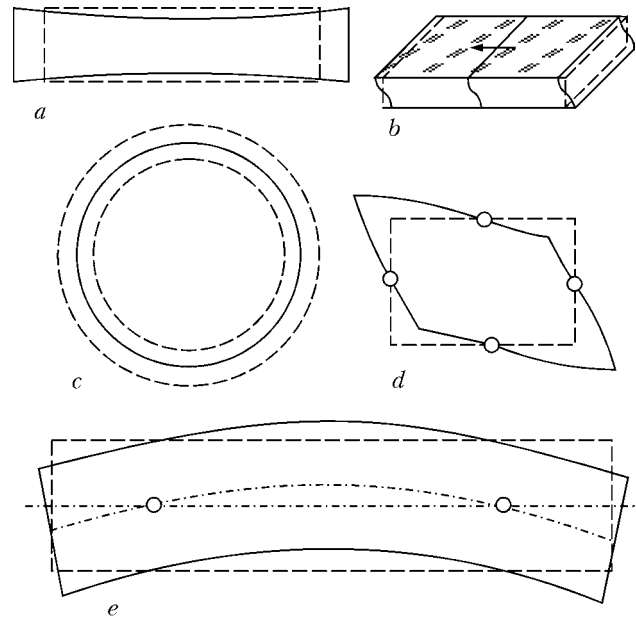


Figure 1. Schematic of the main types of resonance elastic vibrations: *a* — longitudinal vibrations of a rod; *b* — shear vibrations across plate thickness; *c* — radial vibrations of a disc; *d* — shear vibrations around a contour; *e* — bending vibrations along the length and width

weld cleaning after the first pass and was then continued up to complete cooling of the welded sample in air. The power consumed by the vibration generator did not exceed 300 W, the range of excited frequencies being equal to 40 Hz–40 kHz. At treatment of weld 2 the vibration amplitude in the range of 40 Hz to 20 kHz was higher than in the range of 20–40 kHz. At treatment of weld 3, contrarily, the vibration frequency was higher in the range of 20–40 kHz. Vibrations were applied by bringing the ultrasonic head into contact with the flat face surface of the plates being welded at about 60 mm distance from the plane of symmetry of the weld.

Metallographic examination of the influence of wideband sound and ultrasonic treatment on the welded joint structure and properties was conducted. Sections for examination were prepared by a standard procedure with application of diamond pastes. The structure was revealed by chemical etching of samples in nital, investigations were conducted in an optical microscope Neophot-32. Microhardness measurements were made by the LECO microhardness meter M-400 at 500 g load. Grain point was determined by visual comparison with scale references to GOST 5639–82.



Figure 2. Appearance of a generator of wideband audio and ultrasonic vibrations for treatment of welded products

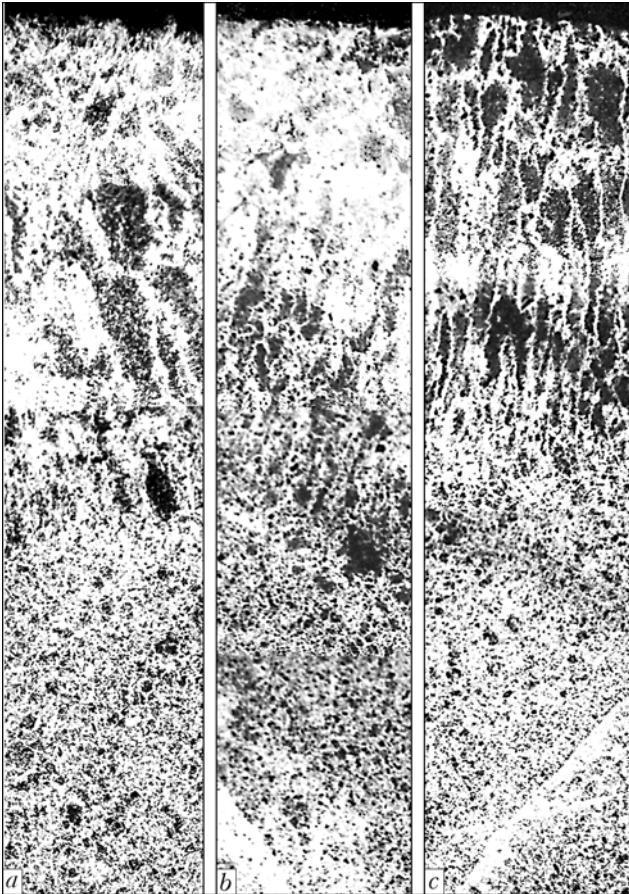


Figure 3. Microstructure of metal in the central part of welds 1-3 (a-c) ($\times 32$)

Macrostructural analysis showed that defects of the type of cracks, pores, lacks-of-penetration, etc. were absent in the welded joints. It was found that in as-welded condition (weld 1) the width of the cast crystallites in the weld central part is greater than that of the joints ultrasonically treated during welding (welds 2 and 3), and is equal to 220, 150 and 100 μm ,

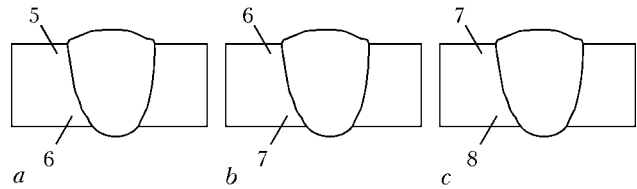


Figure 4. Schematic of a cross-section of welded joints and grain point in the HAZ metal of welds 1-3 (a-c)

respectively (Figure 3). In the root part of the cast weld metal, a refinement of the granular structure under the impact of ultrasonic vibrations was also noted.

Bainite, pearlite and polygonal ferrite, located along the boundaries of the cast austenite grains are also present in the weld metal microstructure (central part). At application of ultrasonic vibrations to the solidifying metal the width of ferrite plates is essentially reduced --- from 20-30 (as-welded condition) to 10-20 and 6-10 μm , respectively. Microhardness in this section of the joint is equal to *HV* 1580-1650 MPa in the initial condition. Microhardness of the metal of welds 2 and 3 rises up to the values of 1650-1810 and 1720-1980 MPa, respectively, which is attributable to lowering of the fraction of polygonal ferrite and increase of the amount of the bainite structural component.

The grain structure of ferrite, pearlite and bainite in the weld root part is refined from the initial 6 to 17 and 8 points in welds 2 and 3, respectively (Figure 4). Microhardness of a mixture of grain structures in the initial condition is equal to 1720 to 1770 MPa. At application of ultrasound in the root part of weld metal, the microhardness rises to 1790 in weld 2 and 1840-1980 MPa in weld 3, which is also related to reduction of the share of the ferritic and pearlitic structural components and increased precipitation of bainite.

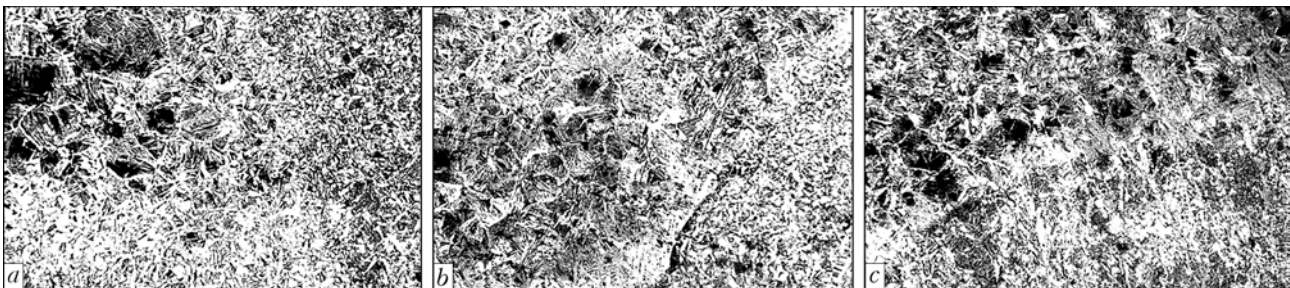


Figure 5. Microstructure of the HAZ metal in the central part of welds 1-3 (a-c) ($\times 100$)

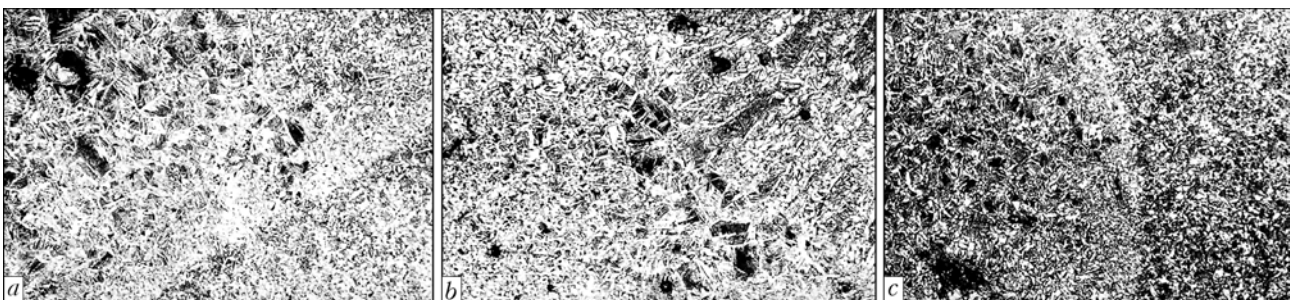


Figure 6. Microstructure of the HAZ metal in the root part of welds 1-3 (a-c) ($\times 100$)



In the metal of the joint HAZ in the overheated zone, the structure is a mixture of pearlite, bainite and ferrite precipitation by the type of Widmanstatten structure and in the form of thin strings along the pearlite and bainite grain boundaries. Under the impact of ultrasonic vibrations a refinement of the HAZ metal structure is observed both on the level of the weld central part across the section thickness, and on the level of the weld root part (Figures 5 and 6).

Microhardness of the HAZ metal for welds 1–3 is equal to 1230–1450, 1250–1510 and 1610 MPa on the level of the central part of welds, and 1510–1560, 1510–1650 and 1790–1820 MPa on the level of the weld root part, respectively.

Thus, the wideband ultrasonic treatment of steel during fusion welding improves the structure of weld metal and HAZ. In the weld metal the width of the cast crystallites in the central part is reduced, equiaxed grains in the root part are refined and the thickness

of ferrite interlayers is decreased. The HAZ metal structure is also refined.

The developed method of wideband ultrasonic treatment can, possibly, be applied not only in most of the fusion welding processes, but also when producing a fine-grained structure of metal products in other kinds of metal treatment, at which phase precipitations of the metal crystalline structure take place, for instance, in casting, surfacing, surface strengthening, coating deposition, etc.

1. Nerubaj, M.S. (1978) Application of ultrasound in treatment of heat-resistant and titanium alloys. *Mashinostroenie*, **8**, 21–23.
2. Kravchenko, V.A., Nerubaj, M.S., Shtrikov, B.L. (1978) Superfinishing of bearing parts by ultrasound application. *Vestnik Mashinostroeniya*, **10**, 67–70.
3. Markov, A.I. (1980) *Ultrasonic treatment of metals*. Moscow: Mashinostroenie.
4. Azizbekyan, L.A., Nersisyan, E.Ts., Oganesyan, D.G. (1996) Improvement of weld quality by ultrasonic wave treatment. In: *Transact. of ArmSKhA. Series Technical Sciences*, Issue 1, 180–184.

STRENGTH PROPERTIES OF LASER-ARC BUTT WELDED JOINTS IN THIN-SHEET ALLOY AMg6

V.A. SHONIN and T.N. NEDEJ

E.O. Paton Electric Welding Institute, NASU, Kiev, Ukraine

Results of investigation into transverse tension properties of 1.9 mm thick welded joints in aluminium alloy AMg6, made by hybrid laser-arc welding and MIG welding in argon atmosphere by the traditional technology, are presented. Effect of such postweld treatments as removal of weld reinforcement and high-frequency peening of metal surface layers at the weld toe is considered.

Keywords: aluminium alloys, thin-walled structures, hybrid laser-arc welding, metal electrode welding, butt joint, mechanical properties, tension, weld reinforcement, high-frequency peening

Important factor determining efficiency of application of hybrid welding methods for joining aluminium alloys is high productivity of this process with a substantial decrease in heat input [1], compared with conventional arc welding methods. The most promising of the hybrid welding methods is a combination of laser beam (LB) with metal electrode inert gas (MIG) welding [2, 3].

At the same time, the data on strength properties of the joints made by laser-arc (MIG + LB) welding are insufficient to recommend this process for the fabrication of critical thin-walled aluminium structures. In the majority of cases such structures operate under conditions of alternating loads and are sensitive to accumulation of fatigue damages in the joints. Given that the arc welded joints have lower fatigue resistance, compared with the base metal, their service life can be extended by postweld treatments, such as removal of reinforcement or local peening of surfaces at the weld toe [4, 5]. Therefore, along with the data on a set of mechanical properties of the as-welded

joints made by the hybrid method, it is also important to have the data on their state after the treatments providing extension of service life of the joints.

The purpose of this study was to evaluate the effect of the MIG + LB welding method on mechanical tensile properties of butt joints in thin-sheet aluminium alloy AMg6 in the as-welded state and after additional treatments, as well as to compare them with properties of the similar joints produced by MIG welding.

AMg6 alloy sheets 1.9 mm thick, 1.2 mm welding wire SvAMg6 (GOST 7871–75) and argon as a shielding gas (GOST 10157–79) were used to weld specimens. MIG welding was performed by using standard equipment «Fronius TPS-2700» under the following conditions: welding current $I_w = 90$ A, arc voltage $U_a = 17.8$ V, welding speed $v_w = 50$ m/h, and wire feed speed $v_f = 5.9$ m/min. Hybrid MIG + LB welding was performed by using the industrial CO₂-laser LP-104 with a net power of 2.5 kW under the MIG welding conditions: $I_w = 185$ A, $U_a = 23.3$ V, $v_w = 300$ m/h, and $v_f = 11.8$ m/min [6]. Chemical composition of the base metal and weld metal of the welded joints was determined by spectral analysis (Table). The base metal had the following mechanical properties: $\sigma_t = 357.3$ – 365.4 MPa, $\sigma_{0.2} = 191.8$ – 209.2 MPa,

Chemical composition of weld metal (wt.%)

Template cutting zone	Si	Mg	Mn	Cu	Zn	Ni	Ti	Fe
Base metal	0.14–0.15	6.2–6.3	0.62–0.64	0.06–0.07	0.20–0.22	0.03	0.03	0.28
Weld:								
MIG	0.14	6.0	0.63	0.05	0.10	0.02	0.03	0.16
MIG + LB	0.15	6.1	0.64	0.05	0.18	0.02	0.03	0.19

$\sigma_{0.01} = 151.4\text{--}157.2$ MPa, $E = 70.95\text{--}71.31$ GPa, and $\delta_5 = 18.6\text{--}20.4$ %.

Mechanical properties of the welded joints were determined on standard flat specimens according to GOST 6996–66 and GOST 1497–84. The test specimens were cut from large-size welded billets. The weld in the specimens was located normal to the rolling fibres and load applied during the tests. In the MIG + LB welded joints the weld thickness was $(1.4\text{--}1.8)a_{b,m}$ (where $a_{b,m}$ is the thickness of the base metal), and in the MIG welded joints the weld thickness was $(2.1\text{--}2.3)a_{b,m}$. Proportional or gauge length of a specimen was assumed to be equal to 50 mm, and width --- to 20 mm.

Three variants of the specimens were studied: 1 --- as-welded, 2 --- with removed reinforcement, and 3 --- with peened surfaces at the weld toe without removal of reinforcement. Not less than three specimens of the same type were made for each variant.

Local high-frequency peening of the variant 3 specimens was performed by using a portable piezo-ceramic ultrasonic tool [5]. The tool tips had a single-row group of needle-like strikers 3 mm in diameter. The speed of peening was 4–5 mm/s. Weld reinforcement in the variant 2 specimens was removed by grind-

ing to the level of surface of the base metal along the specimen axis.

Tensile tests were conducted using an upgraded testing machine of the UME-10tm model. Deformation diagrams were fixed with a two-coordinate recorder of the N307/1 type. Strain gauge with base $l_e = 25$ mm was used to determine the proof values of yield stress $\sigma_{0.2}$ and elasticity limit $\sigma_{0.01}$. The speed of movement of the testing machine grips was 0.5 mm/min, and then, to fracture of a specimen, 5 mm/min. Elongation δ_5 after fracture of the test specimens was evaluated from the initial gauge length $l_0 = 5.65\sqrt{ba} = 35$ mm (here b and a are, respectively, the specimen width and thickness). The character of accumulation of residual strains in different zones of the welded joint was determined from the values of local elongation δ_1 . This was done by using a transverse marking with a spacing of 1 mm along the specimen axis. The marks before the tests were made and elongation of a specimen between the marks after the tests was measured using the BMI-1 toolmaker’s microscope.

The tensile test results are represented by average values of mechanical properties of welded joints on three specimens (Figures 1 and 2). The values of re-

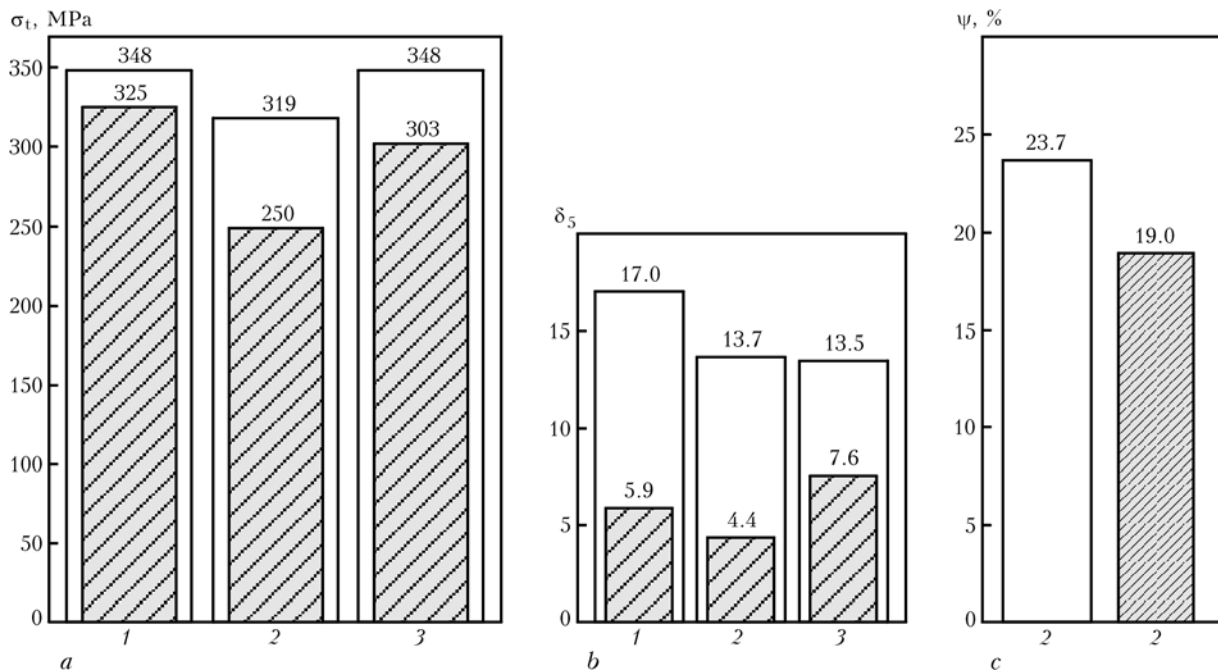


Figure 1. Mechanical properties of MIG + LB (dashed regions) and MIG (light regions) welded joints in the as-welded state (1), after peening (2) and after removal of weld reinforcement (3) in short-time tensile tests: a --- short-time strength σ_t ; b --- elongation δ_5 ; c --- reduction in area ψ

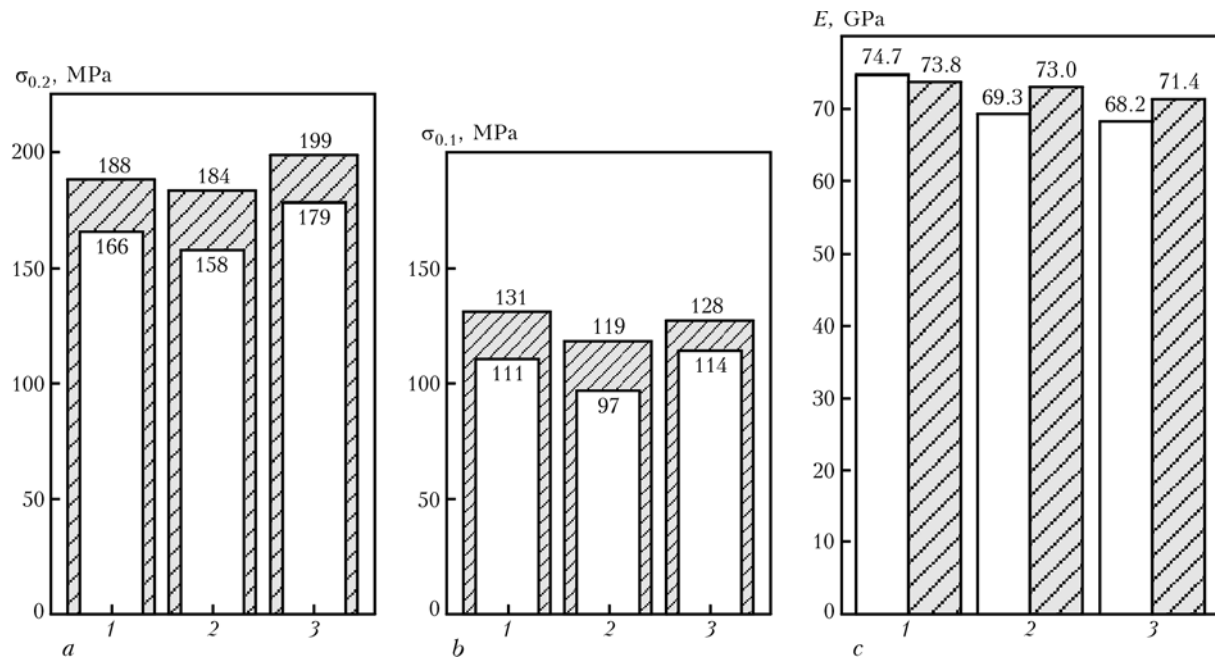


Figure 2. Elasto-plastic (a) and elastic (b, c) properties of MIG + LB (dashed regions) and MIG (light regions) welded joints in tension: 1–3 — see Figure 1

duction in area ψ (Figure 1, c) were determined only for smooth specimens with the removed weld reinforcement. Typical distribution of local elongation δ_1 in a joint after fracture is shown in Figure 3.

The data on mechanical properties of the joints made by hybrid MIG + LB welding differ markedly from those of the MIG welded joints. Independently of a manufacture variant, specimens of the butt joints made by hybrid welding are characterised, on the average, by higher values of elasticity limit $\sigma_{0.01}$ and yield point $\sigma_{0.2}$, compared with those of the MIG welded joints, the values of short-time strength σ_t and elongation δ_5 being lower than σ_t and δ_5 of the MIG welded joints (Figures 1 and 2).

Tests of the geometrically identical joints (smooth proportional specimens made by variant 2) showed that the hybrid welding method, compared with MIG welding, provided a 16 % increase in the $\sigma_{0.2}$ values, 23 % increase in the $\sigma_{0.01}$ values and 5 % increase in elasticity modulus E , but a 28 % decrease in the σ_t values, 3.1 times decrease in δ_5 , and 1.3 times decrease in ψ . Fracture in this case occurred in the weld metal, this corresponding to a substantial degree to mechanical properties of the joints shown in Figures 1 and 2. Differences in thermal conditions of the above welding processes affect the uniformity of mechanical properties of the weld metal, weld zone and fusion zone metals, which is evidenced by the character of a non-uniform distribution of local elongation δ_1 . In the MIG + LB welded joints, the maximal values of residual strains in deformation to fracture are accumulated in the weld metal (Figure 3, c). The metal of the near-weld zone, which is little prone to heat affect, is deformed almost uniformly. In the MIG welded joints, the maximal values of residual strains are accumulated both in the weld metal and weld zone,

because of a substantial heat affect provided by this welding method (Figure 3, d).

Visual examination of fracture of smooth specimens showed that the MIG + LB welded joints fractured in the weld with brittle tear. The fracture surface is grey in colour, and has roughness characteristic of a granular fracture. No crack-like formations were detected in the fusion zone. The MIG welded joints fractured in the weld. Fracture was of a tough character, and the fracture surface was oriented at an angle of 45° to the loading axis. Fractures had a smooth bright surface, and tears were detected in the fusion zone.

Reinforcements induce a non-proportional loading along the specimen axis and lead to increase in the ultimate fracture force for the weld. In the MIG + LB welded joints, it is the fusion zone that is responsible for fracture. Short-time strength of such a joint (variant 1) is 30 % higher than σ_t of the joints with the removed weld reinforcement (variant 2). The MIG + LB welded joints are characterised by the minimal external reinforcement without rolls on the fusion zone, and by the presence of shallow undercuts. Residual strains in the joints at fracture are distributed uniformly in the weld zone up to external boundaries of the fusion zone, and maximal values of δ_1 take place primarily in the fusion zones and, partially, in the adjoining regions of the weld and base metal (Figure 3, a). Short-time strength of the fusion zone metal was a bit higher (by 2 %) compared with the MIG weld metal (see Figure 1).

In MIG welding, a substantial height of reinforcement with rolls on the base metal in the fusion zone originated in weld formation became the cause of fracture of the joint far from the weld in HAZ at a distance of about 10 mm from the weld toe (Figure 3, b). Short-time strength of the joints (variant 1) was 9 %

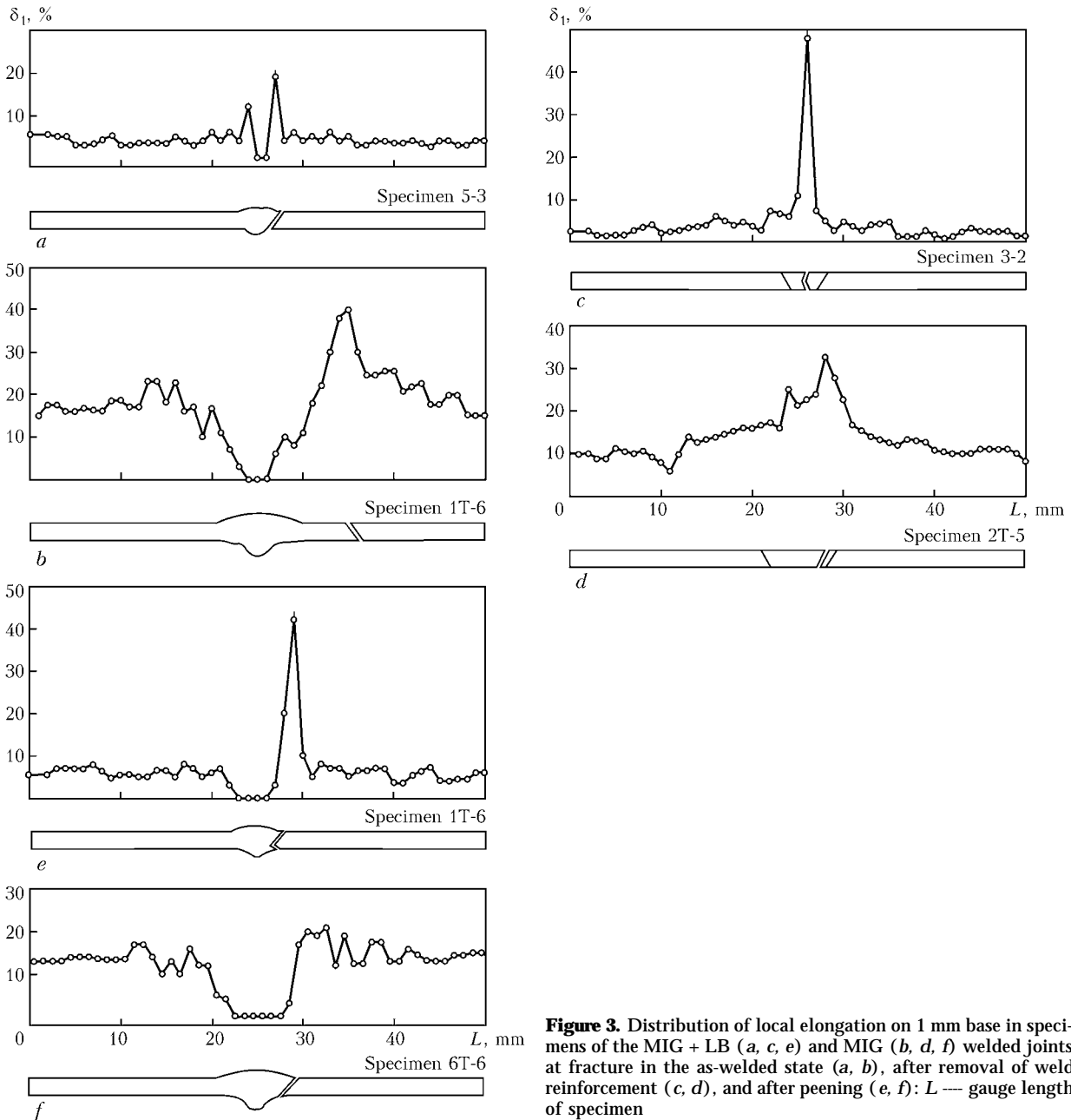


Figure 3. Distribution of local elongation on 1 mm base in specimens of the MIG + LB (a, c, e) and MIG (b, d, f) welded joints at fracture in the as-welded state (a, b), after removal of weld reinforcement (c, d), and after peening (e, f): L — gauge length of specimen

higher, on the average, compared to the joints with the removed reinforcements (variant 2). No residual elongation was detected in the weld with the as-welded reinforcement. Separations of the weld metal rolls from the surface of the base metal and tears in the fusion zone under a roll occurred in fractures of the specimens.

In the MIG + LB welded joints with reinforcements in the as-welded condition (variant 1), the values of $\sigma_{0.01}$ and $\sigma_{0.2}$ were 10 and 2 % higher, and in the MIG welded joints these values were 14 and 5 % higher, respectively, compared with the similar values of the joints with the removed weld reinforcements. The values of elongation δ_5 in the MIG + LB welded joints increased 1.34 times, and those in the MIG welded joints increased 1.24 times. Weld reinforcements in the MIG + LB welded joints had a little

effect on the E value, whereas in the case of MIG welding they led to increase of 8 % in the E values.

Local peening of the surface layer at the weld toe in the MIG + LB welded joints (variant 3) caused increase in $\sigma_{0.2}$ to 6 % and decrease in $\sigma_{0.01}$ of 2 %, compared with the similar values of the as-welded joints (variant 1). After peening of the MIG welded joints, the values of $\sigma_{0.2}$ and $\sigma_{0.01}$ increased to 8 and by 3 %, respectively. In this case the values of elasticity modulus E of the MIG + LB welded joints decreased by 3 %, and those of the MIG welded joints decreased to 9 % (see Figure 2). It seems that the peened metal layers restrain the initial stage of plastic strains in the welded joints, but lead to decrease in the elasticity modulus. σ_t of the peened joints was 13 % lower, on the average, compared to the as-welded joints made by MIG + LB welding, and remained almost un-



changed in the joints made by MIG welding (see Figure 1). Fracture of the joints after peening occurred mostly in the fusion zones and was of a tough character. Regions of separation of the peened metal can be seen in fractures of the destructed specimens, the level of accumulated residual elongation being decreased in the peened zones (see Figure 3, e, f).

Therefore, butt joints in thin-sheet aluminium alloy AMg6, produced by MIG + LB welding using electrode wire SvAMg6, are characterised by increased values of elasticity limit and yield stress, which may have a positive effect on improvement of fatigue resistance of these joints under high-cycle loading. Short-time strength and ductility of the weld metal in hybrid welding do not reach the values characteristic of the joints made by MIG welding. That is why, removal of the weld reinforcement to extend service life is not indicated for the MIG + LB welded joints. The effect of local peening of the joints with non-removed reinforcements shows up in growth of the yield stress value. Short-time strength of the joints does not increase in this case.

It is likely that the metallurgical factor, i.e. the effect of the rate of solidification of the weld on its structural state, is responsible for mechanical properties of the joints produced by hybrid MIG + LB welding. Here the effect by the mechanical factor (transverse shrinkage of the weld metal) is mitigated, and no solidification cracks are formed in high-speed welding [7].

CONCLUSIONS

1. The use of hybrid high-speed MIG + LB welding of thin-sheet aluminium alloy AMg6 provides increase

of 18 % in the elasticity limit values and 13 % in the short-time strength values of the butt joints with non-removed reinforcements, compared with the similar values of the MIG welded joints.

2. Equal forces for fracture of the weld and adjoining zones in the MIG + LB welded joints can be provided only in the presence of the weld reinforcement, because strength and ductility of the weld metal produced by using electrode wire SvAMg6 do not reach the values of short-time strength of the base metal.

3. The use of postweld high-frequency peening of the surface layer at the toe of the weld with reinforcement leads to increase in yield stress of a welded joint, the value of short-time strength being not increased.

1. Stauffer, H., Hackl, H. (2001) Laser-MIG process for automotive industry. *The Paton Welding J.*, **12**, 26–29.
2. Dilthey, U., Lueder, F., Wieschemann, A. (1999) Erweiterte Moeglichkeiten beim Schwei en von Aluminiumlegierungen durch den Laser-MIG-Hybridproze. *Aluminium*, **75**(1/2), 64–75.
3. Shida, T., Hirokawa, M., Sato, S. (1997) CO₂-laser welding of aluminum alloys (Welding of aluminum alloys using CO₂-laser beam in combination with MIG arc). *Quarterly J. JWS*, **15**(1), 18–23.
4. Shonin, V.A., Mashin, V.S., Vojtenko, O.V. et al. (2003) Improvement of fatigue resistance of tee welded joints in sheet aluminium alloy AMg6. *The Paton Welding J.*, **7**, 7–10.
5. Trufiyakov, V.I., Shonin, V.A., Mashin, V.S. et al. (2001) Application of high-frequency peening to improve the fatigue resistance of butt welded joints in aluminium alloys. *Ibid.*, **7**, 6–10.
6. Shonin, V.A., Mashin, V.S., Khaskin, V.Yu. et al. (2006) Residual stresses in joints on thin-sheet alloy AMg6 induced by arc and laser-arc welding. *Ibid.*, **9**, 20–24.
7. Rabkin, D.M. (1986) *Metallurgy of fusion welding of aluminium and its alloys*. Kiev: Naukova Dumka.

UNIVERSAL ELECTRODES FOR WELDING HIGH-ALLOY HEAT-RESISTANT DISSIMILAR STEELS

Coated metallic electrodes of ANV-70 grade of 07Kh25N13G2 type for manual arc welding of metal structures of high-alloy steels of different structural classes (austenitic, austenitic-ferritic and ferritic) provide, unlike the known analogues, for example electrodes 03L-6, TsL-25, ZNO-8, the better formation of weld metals, removal of slag crust, lower losses of electrode material for spattering, more stable arc burning in welding in all spatial positions.

Purpose and application. Electrodes ANV-70 are designed for welding heat-resistant and high-temperature dissimilar steels of 10Kh23N18, 25Kh25N20S2, 20Kh23N13, 15Kh25T types used in power, chemical machine building and other branches of industry.

Status and level of development. Technology of manufacture has been mastered and electrodes ANV-70 are tested.

Proposals for co-operation. Signing of contracts.

Main developers and performers: Prof. Yushchenko K.A., Dr. Kakhovsky Yu.N., Dr. Bulat A.V.

Contacts: Prof. Yushchenko K.A.
E-mail: Tel./fax: (38044) 289 9087, 287 1088



PECULIARITIES OF MELTING OF FLUX-CORED STRIPS WITH EXOTHERMIC MIXTURES CONTAINED IN THEIR FILLER

V.V. CHIGAREV, D.A. ZARECHENSKY and A.G. BELIK
E.O. Paton Electric Welding Institute, NASU, Kiev, Ukraine

Results of analysis of the effect exerted by exothermic mixtures of different compositions contained in a flux-cored strip filler on the character of melting of electrode and distribution of temperature at its extension are given.

Keywords: wear-resistant alloy, deposited metal, flux-cored strip, filler, exothermic mixture, melting character, shunting of current, heat effect

Flux-cored strips are widely applied for deposition of wear-resistant alloys. However, their technological capabilities are limited in a number of cases by different rates of melting of their sheath and filler, which leads to deterioration of quality of the deposited metal.

Results of investigations [1–4] into the processes of melting of flux-cored strips showed that temperature at the strip tip is insufficient for complete melting of the core, which provides transfer of the electrode material via the drop stage.

In melting of flux-cored electrode materials the rate of melting of the strip core lags behind that of melting of the strip sheath, which leads to a spontaneous transfer of the core components to the weld pool, and this transfer cannot be controlled. This process of transfer of components in melting of flux-cored strips is promoted by refractoriness of the charge components, insufficient degree of combined reduction of the sheath and core, and shortage of the effective heat for melting.

Causes of this character of melting of flux-cored strips is insufficiently studied in technical literature, which prevents implementation of their advantages.

The purpose of this study was to investigate the effect of additions of exothermic mixtures to the filler of flux-cored strips on distribution of the heat energy in their melting.

Investigations were conducted to evaluate heating of the sheath and filler of a flux-cored strip in cladding, which was performed by using the automatic device AD-231 with the power supply KIU-1201. The temperature was fixed with 0.2 mm diameter chromel-alumel thermocouples using recorders N-340 and oscillograph K-12-22. Schematic of fixing of the thermocouples is shown in Figure 1. Thermal junctions were welded to the strip sheath by capacitor-discharge spot welding. A thermocouple was insulated in the charge at the junction location. Sections of experimental flux-cored strips 1000 mm long were used in the experiments. Compositions of the fillers are given in the Table. Stoichiometric proportion of iron oxides and reducing agents was maintained in the compositions of the fillers. It was taken into account that the temperature of not less than 1473–1573 K is required for the beginning of exothermic reactions [5], which takes place only at the tip of a consumable electrode. Cladding with the experimental strips was performed at the reverse-polarity direct current $I_w = 700\text{--}750$ A, arc voltage $U_a = 30\text{--}32$ V, and extension of 50 mm.

Figure 2 shows distribution of a heating temperature in the flux-cored strip sheath and filler during cladding. The thermal junction was fixed at a distance of 4–6 mm from the boundary of the electrode tip melted by the arc to prevent its effect on thermocouples.

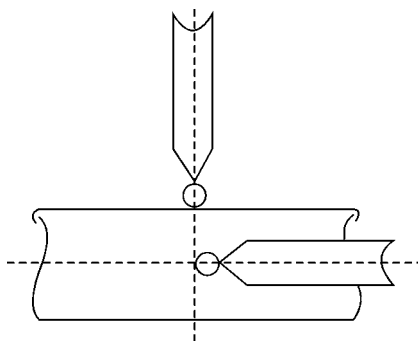


Figure 1. Schematic of fixing of thermocouples on flux-cored strip

Compositions of fillers (wt.%) of experimental flux-cored strips

No. of flux-cored strip	Iron powder	Scale (hematite)	Aluminium powder
1	--	100.00	--
2	100	--	--
3	75	18.75	6.25
4	50	37.50	12.50
5	25	56.25	18.75
6*	26	44.00	--

*Contains 30 wt.% of ferroalloys.

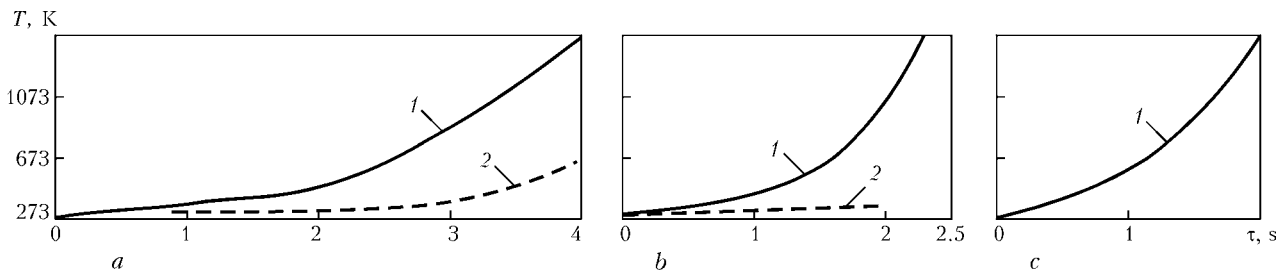


Figure 2. Distribution of heating temperature in sheath (1) and filler (2) of flux-cored strips 1 (a) and 2 (b), and strip without filler (c)

As established, the sheath at the extension can be heated to a temperature of 473 K, and at a distance of 8–10 mm from the sheath tip the temperature grows. After extinguishing of the arc, heating at the electrode tip propagates to the thermal junction, and the average temperature is 1473 K. The filler is heated together with the sheath.

Temperature of the filler is insignificant at the extension, and only near the electrode tip it grows to 373 K. As established, no temperature conditions required for the beginning of exothermic reactions exist at the electrode extension.

It can be seen from Figure 2 that temperature gradient between the sheath and filler of the flux-cored strip increases with distance of thermal junctions to the arc. The time for reaching maximal temperatures of the core sheath at the extension for a flux-cored strip without a filler (Figure 2, c) and strip with a scale (Figure 2, a) contained in the filler is 2 times as low as in the case of an iron powder filler (Figure 2, b). The latter is heated more intensively than the hematite filler, which is attributable to shunting of the current with the filler, as well as to its thermal conductivity.

Shunting of the current with the filler is confirmed by the experimental data [6], which are indicative of the fact that increase in the heating temperature leads to the identical increase in resistance of the flux-cored strips without a filler and with the hematite filler, while in strips with the iron powder filler, which are characterised by an increased thermal conductivity compared with hematite, part of the current flows through the filler, thus decreasing heating of the sheath at the extension.

Figure 3 shows the effect by compositions of flux-cored strips containing exothermic aluminium- and ferroalloy-based mixtures on heating of the sheath and filler. It was determined that the filler is slightly heated before extinguishing of the arc, and after extinguishing (point A in Figure 3) its temperature markedly grows. A gradual decrease of temperature in the sheath and a dramatic increase of temperature in the filler take place 0.5–1.0 s after extinguishing of the arc, instead of a dramatic decrease of temperature in the electrode sheath and filler, this being caused by an exothermic reaction occurring in the filler.

The character of the curves plotted for melting of strips containing different amounts of exothermic aluminium-based mixtures shows that temperature of the

filler grows with increase of the mixture content in it due to more heat evolved as a result of exothermic reactions (Figure 3, a–c). Increase in the sheath heating temperature and rate is caused by decrease in the shunting current due to the scale contained in the filler.

The mechanisms of heating of the sheath and filler persist also in the case of using an exothermic mixture

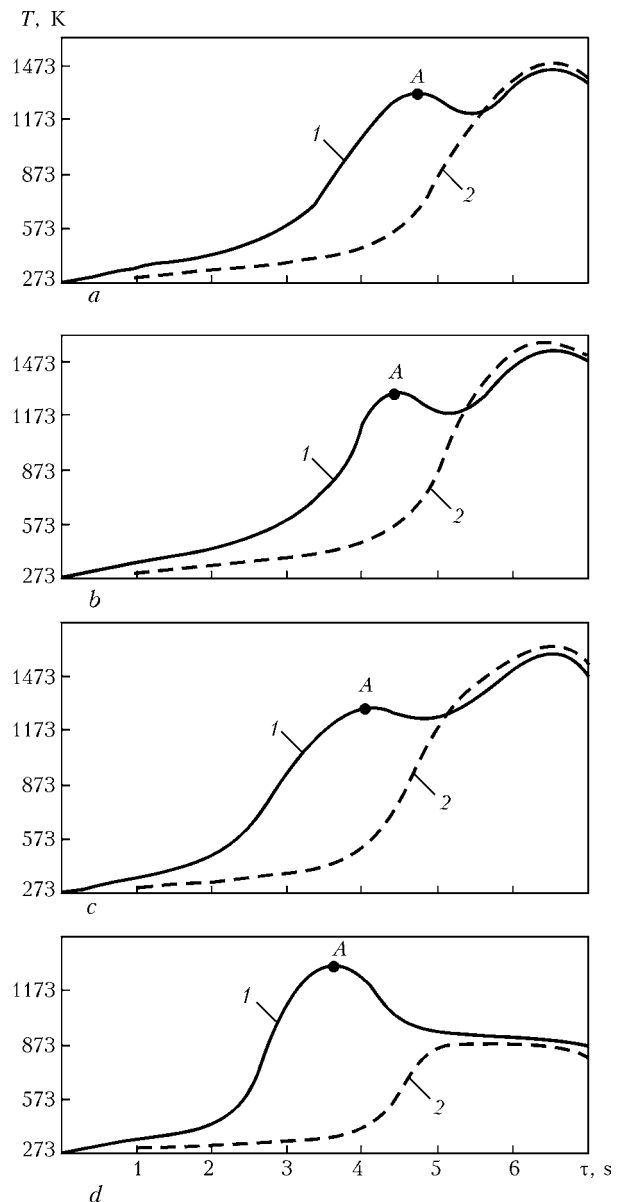


Figure 3. Effect of compositions of exothermic mixtures in flux-cored strips on distribution of temperatures in strip sheath (a) and filler (2) for specimens 3–6 (a–d)



with a reducing agent of ferroalloys (strip 6, Table), the character of heating of the filler being different. It can be seen from Figure 3, *d* that the temperature jump in heating of the filler is lower than in the case of using aluminothermic mixtures (strips 3–5, Table). The filler is heated near the melting tip by not less than 300 K, and after extinguishing of the arc it is heated to 700 K due to the heat energy of the reactions.

The data obtained are indicative of the fact that there exists a temperature gradient between the sheath and filler for the flux-cored strips of the compositions under consideration. The character of heating of the strip sheath and filler is approximately identical for all compositions of the flux-cored strips containing the exothermic mixtures, although the heating temperature is different. As shown by the investigation results, the exothermic mixtures based on iron oxides with aluminium and ferroalloy reducers have a different effect on heating and melting of the flux-cored strips. Thus, the strip sheath containing ferroalloys is heated to 1000 K for 3 s of melting of the electrode. The strip sheath containing aluminium is heated to 550 K in shunting of the current with the filler during the same time. A higher temperature jump in heating of the hematite-aluminium filler evidences a higher evolution of heat as a result of the exothermic reactions.

The use of exothermic mixtures based on hematite and ferroalloys will allow minimisation of transfer of the heat energy from the sheath to filler, as well as increase in the values of melting of the flux-cored strips.

The thermal effect of exothermic reactions can be controlled through the content of the exothermic com-

ponent in the filler, whereas the rates of melting of the sheath and filler can be controlled through establishing the optimal composition and content of this component in the filler, thus providing their uniformity.

CONCLUSIONS

1. Adding exothermic mixtures based on iron oxides to the composition of fillers of flux-cored strips provides occurrence of the reaction at the electrode tip, which allows prevention of spillage of the filler particles and improvement of quality of the deposited metal.

2. Iron scale (hematite) contained in the flux-cored strip filler decreases shunting of the current with the filler and increases the rate of heating of the strip sheath, which promotes melting of the electrode.

3. Exothermic mixtures in fillers of different compositions hardly change the character of heating of the sheath and filler of flux-cored strips, but they do change the heating temperature and rate.

1. Azizova, S.A., Lyalin, K.V. (1969) Study of the process of electrode metal melting and transfer in flux-cored wire welding. *Svarochn. Proizvodstvo*, **8**, 8–10.
2. Erokhin, A.A., Zelenova, V.I., Ioffe, I.S. (1978) Dependence of reactions between the core metal and charge on characteristics of flux-cored wire and welding parameters. *Avtomatich. Svarka*, **7**, 18–21.
3. Kotov, G.N., Erokhin, A.A. (1968) Influence of coating thickness and its metal additives on electrode melting rate. *Ibid.*, **8**, 16–17.
4. Ioffe, I.S., Erokhin, A.A. (1970) Melting coefficient of wire with iron powder in the charge. *Ibid.*, **9**, 64–65.
5. Baptizmansky, V.I., Isaev, E.I., Zhigunin, V.I. et al. (1970) *Deoxidising and alloying of steel with exothermic ferroalloys*. Kiev: Tekhnika.
6. Zarechensky, A.V., Leshchinsky, L.K., Chigarev, V.V. (1985) Peculiarities of melting of flux-cored strips containing thermit mixtures. *Svarochn. Proizvodstvo*, **8**, 39–41.

NEWS

NKMZ SUPPLIES EXCAVATORS TO BELARUS AND RUSSIA



The Novokramatorsk Machine-Building Factory (NKMZ), Kramatorsk, Donetsk District, delivered two excavators with new capabilities, i.e. ESh-11/70 and ESh-10/50 (modification of ESh-11/70), to Belarus and Russia. New machines equipped with advanced control systems are more reliable, cost-effective and comfortable than their older counterparts, and they are simpler to operate. Ingenious designs of the new control system of the excava-

tors made it possible to substantially simplify control of their main drives, ensured smooth start of synchronous electric motors, and provided vibration protection of control cabinets.

The efficient control system of the NKMZ brand earth-moving machines replaced the one used earlier. Manufacture of the advanced machines opens up new prospects for the Factory in the industrial market.



INFLUENCE OF PULSE ELECTROMAGNETIC ACTIONS ON FORMATION AND SOLIDIFICATION OF WELDS

R.N. RYZHOV

NTTU «Kiev Polytechnic Institute», Kiev, Ukraine

On the basis of experimental investigations efficiency of the weld formation and solidification control processes was estimated using external electromagnetic actions based on application of pulse magnetic fields.

Keywords: electromagnetic actions, hot cracks, formation and solidification of welds

External electromagnetic actions (EMA) on the pool melt and process of the electrode wire mass transfer are performed in arc welding by conduction and induction methods. In the first method force action on mentioned objects of control is created at vector interaction in their elementary volumes of the welding current with a constant or a low-frequency controlling magnetic field (CMF). The second method is based on induction by means of axial pulse magnetic fields of eddy currents in the pool or in drops of the electrode metal. Their interaction with radial component of CMF creates volumetric force, acting in direction from the electromagnet.

It is established that EMA with constant and low-frequency CMF are more frequently used for improving the weld quality parameters. They are used for controlling hydrodynamics of the pool melt, due to which improve processes of the weld solidification and degassing [1]. Radial CMF are used for compensating gravitational forces, which act on the pool in gravity welding [2], and deviations or fluctuations of the arc [3]. EMA with pulse CMF are used only for controlling process of the electrode wire mass transfer [4] and increasing current density in the pool, which increases efficiency of mentioned technologies of gravity welding. Rather narrow application of such EMA may be connected with insufficient degree of investigation of their technological processes.

It is known [5] that for maximum refining of primary structure of the welds and reduction of their porosity and inhomogeneity the EMA frequency should correspond to the natural frequency of solidification of the material being welded, which depends upon chemical composition of the latter. In electromagnetic stirring, which is the most distributed kind of EMA, due to inertance of the melt, frequency of reversal of its flows, moving under action of Lorentz force from the head to the tail part of the pool, does not exceed 25–30 Hz. Proceeding from the fact that solidification frequency of many materials being welded is practically by one order higher than that mentioned above, achieved by means of such EMA

improvement of quality of the welds can not be considered maximally possible.

One can efficiently influence on solidification processes by excitation in the pool volume of high-frequency oscillations of the melt, which is confirmed by results of many investigations (for example, welding with ultrasonic treatment of the melt, modulated current welding, etc.). For implementation of such actions one can also use pulse EMA, performed by induction method, but published data on their efficiency were not found. Possible accompanying changes of the weld formation parameters are also of interest.

Proceeding from mentioned above, the purpose of this work is estimation of the pulse CMF-base EMA efficiency in controlling processes of formation and solidification of the welds.

In the process of experimental investigation the CMF high-frequency pulses in the welding zone were generated by serial discharge of high-voltage capacitors of 100 μF capacity through the water-cooled inductor coil, located on external surface of the ferromagnetic nozzle. Current of the capacitor charging was regulated by rheostats, and discharge frequency f_{pulse} by included into the power supply circuit of the inductor thyristor, controlled from a specialized generator.

EMA influence on solidification processes of the welds was estimated by resistance of the welds to formation of hot cracks. Formation of the latter was simulated on technological samples «fish skeleton», manufactured from the AMg6 aluminium alloy. Parameters of the welding mode were chosen in such

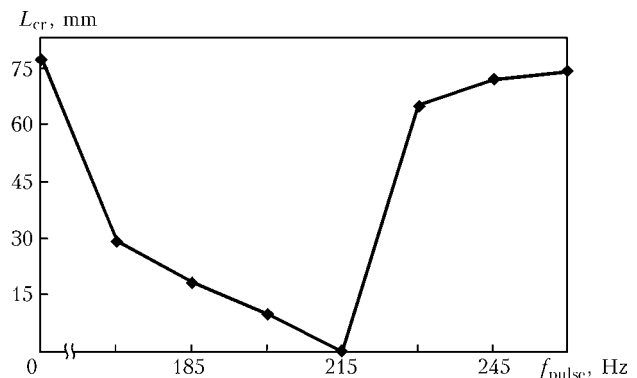


Figure 1. Change of length of hot cracks L_{cr} in technological samples «fish skeleton» at different frequency of CMF pulses f_{pulse}

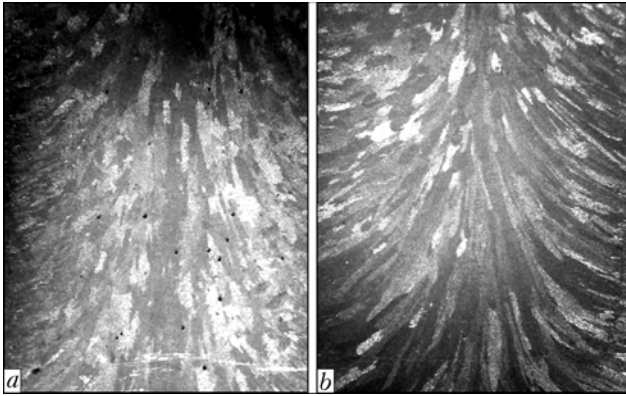


Figure 2. Macrostructure of welds in arc welding under conventional conditions (a) and with pulse EMA (b) ($f_{\text{pulse}} = 200$ Hz)

way that length of the crack be maximal under initial conditions: $I_w = 110$ A, $U_a = 10$ V, $v_w = 19$ m/h. Frequency of CMF pulses was changed within the 0–260 Hz range, and distance from the ferromagnetic nozzle end to the pool surface plane equaled 3 mm.

In the course of experiments significant reduction in the hot crack length in the samples was registered in the cases, when frequency of CMF pulses corresponded to 170–220 Hz (Figure 1). At $f_{\text{pulse}} = 215$ Hz brittle fracture of the specimens was completely absent. Macrostructure analysis, carried out for explanation of mentioned effect, showed that under EMA conditions, close to the optimal ones, refining of the crystallites occurred over the whole section of the welds (Figure 2). In the rest cases changes of the structure in central area of the welds was less noticeable than near the fusion line. Proceeding from this fact one may assume that dependence exists between frequency of CMF pulses and the distance, over which propagate in the direction of solidification front created with its assistance vertical fluctuations of the melt. Presence in Figure 1 of the extremum may be explained by occurrence of resonance phenomena at optimal frequency of the charge in the pool volume. One should expect that in case of change of the welding mode parameters and thermophysical properties of the materials being welded maximum effect from such EMA will be achieved at other CMF frequencies.

It is established that in addition to solidification processes, investigated EMA on the pool melt cause change of the weld formation parameters (Figure 3). It is explained by the fact that in the course of experiments the inductor was located above the weld, due to which generated by it axial CMF created pulse force action on the melt, directed to the pool bottom. In the tail part horizontal component is directed opposite the forces, which move the melt from the head part of the pool to the solidification front. As a result during pulses of the magnetic field, repeated with frequency up to 200 Hz, either retardation or suspension of mentioned flows occurs, accompanied by accumulation of the melt volume under the arc and on

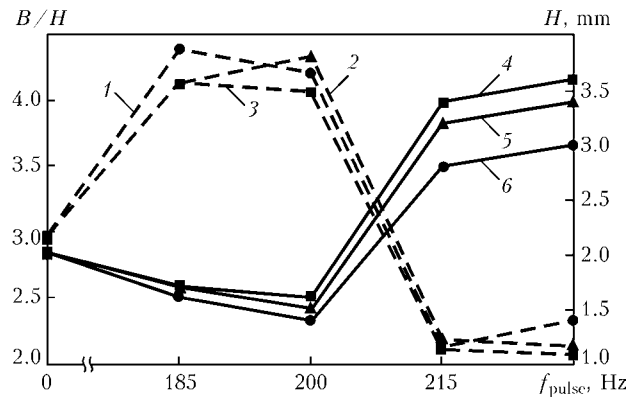


Figure 3. Dependence of penetration depth H (solid curves) and weld shape factor B/H (dash lines) upon frequency of CMF pulses: 1, 6 — distance from ferromagnetic nozzle end to pool surface plane of $h = 5$ mm; 2, 5 — $h = 4$ mm; 3, 4 — $h = 3$ mm

front wall of the pool. It causes reduction of penetration capacity of the arc and partial melting of side walls of the pool, which explains reduction of the penetration depth H and increase of the weld width B at f_{pulse} up to 200 Hz. Further increase of the magnetic field pulse frequency, and therefore EMA intensity, causes periodic formation of the melt flows in direction of head part of the pool. Whereby width of the welds continuous to increase, and depth of penetration increases due to reduction of liquid interlayer thickness under the arc (this explains presence of extremum in the dependence of the weld shape factor B/H upon f_{pulse} (Figure 3)). In the course of experiments EMA intensity was also regulated by change of the distance between the ferromagnetic nozzle end and the pool surface plane. It is established that in all cases to its reduction corresponds certain increase of B and H ; however, in practical implementation of pulse EMA decisive significance belongs not to the amplitude, but to dynamic characteristics of CMF.

So, for controlling processes of weld formation and solidification in the arc welding the EMA are efficient, which are implemented not just by means of low-frequency alternating-sign CMF, but also by pulse ones. Optimization of their characteristics has to be performed allowing for thermophysical properties of the materials to be welded and energy parameters of the welding mode.

1. Ryzhov, R.N., Kuznetsov, V.D. (2006) External electromagnetic effects in the processes of arc welding and surfacing (Review). *The Paton Welding J.*, **10**, 29–35.
2. Brodyagina, I.V., Chernyshov, G.G. (1998) Arc welding of aluminium alloys using the magnetic fields. *Svarochn. Proizvodstvo*, **9**, 48–51.
3. Ryzhov, R.N., Semenyuk, V.S., Titov, A.A. (2004) Peculiarities of formation and crystallization of welds in TIG welding with magnetic arc deflection. *The Paton Welding J.*, **4**, 14–17.
4. Tarasov, N.M., Kapustin, S.S. (1982) Application of high-frequency electromagnetic field for batched transfer of electrode metal drops. *Avtomatich. Svarka*, **8**, 10–12.
5. Ryzhov, R.N., Kuznetsov, V.D. (2005) Choice of optimal parameters of external electromagnetic action in arc methods of welding. *The Paton Welding J.*, **6**, 24–27.



THESIS FOR SCIENTIFIC DEGREE



E.O. Paton Electric Welding Institute, NASU, Ukraine

On January 24, 2007 **A.G. Bryzgalin** (PWI) defended the thesis of Candidate of Sci. (Eng.) on the subject of «Reducing Residual Welding Stresses in Circumferential Welds of Pipelines by Explosion Treatment».

In this work it is shown that residual welding stresses are the energy basis of initiation and development of crack type defects, and their relieving in circumferential pipe welds can be regarded as one of the principal measures for ensuring the fatigue life of pipelines for different purposes, including those that are exposed to aggressive medium in service. Technology of explosion treatment (ET), developed at PWI, is significantly superior to other currently-available technologies in terms of cost-effectiveness and immediacy of application for reducing residual stresses in circumferential welds of the pipes that allows considering it as the most promising.

Existing approaches to calculating ET parameters imply involvement of designer-specialists. The problem of developing engineering methods for determination of ET parameters and efficient methods of treatment result control that could be used under the conditions of wide industrial application of ET by specialists of different branches without participation of technology developers is quite urgent. Its solution will allow presentation of the ET technology as a product, ready for sale to outside organizations.

The aim of the work was to develop an engineering method for determination of effective modes of ET of pipeline circumferential welds without carrying out experimental investigations, improve the technology of residual stress lowering by ET, and improve the methods of efficient non-destructive testing of stressed state of metal structures, including that after ET.

Original method of parameter calculation for ET of pipe circumferential welds was worked out to ensure lowering of residual welding stresses, based on application of rather accurate results of analysis of elastic shell behaviour under static loading to solution of the dynamic problem of shell wall deformation. The procedure of treatment mode determination was developed on the basis of this method. Presence of an approximate linear dependence between residual stress level in a circumferential weld and the value of their change as a result of ET by the modes, specified in accordance with the developed procedure was determined. Presence of such dependence enables predicting the treatment results and correcting the treatment parameters, if required. The schematic of preliminary ET of pipe edges before welding to decrease residual stresses in circumferential welds was developed for the first time. The method of non-destructive magnetoelastic strain measurement was improved, this allowing an essential increase of the accuracy and simplifying the procedure of carrying out the measurements. It was experimentally shown that the resistance of pipe circumferential welds to hydrogen sulfide damage after ET exceeds this parameter for untreated welds, or those subjected to higher pressure testing, and is not lower than that of heat-treated welds. ET does not impair the sulphide cracking resistance of pipe base metal exposed to the impact of pulse loading at blasting of the explosive charge.

The results of studies carried out in this work and the found engineering solutions were the basis for development and industrial application of technologies of ET of circumferential welds in Taas-Tumus-Yakutsk gas pipeline, water pipelines of Tashlyk pumped-storage plant, and were used for evaluation of the stressed state of oil storage tank wall of OJSC «Eksimnefteprodukt», and tank walls in a nickel plant in Punta Gorda (Cuba).

JUBILEE CONFERENCE «WELDING DAYS 2006» IN GERMANY

On November 22–23, 2006 the International Conference «Welding Days 2006», dedicated to 50th anniversary of GRSS, was held in Geestacht (Germany) at GRSS Research Center. More than 80 scientists and specialists from Germany, Poland, Romania, Brazil, China, Lithuania, Ukraine and other countries took part in the Conference. The Conference was held with the support of the German Welding Society (DVS), GDA and «Aluminium» journal.

Most of the paper themes were devoted to solid phase welding and joining processes, including the following subjects:

- friction welding (traditional process and friction stir welding);
- ultrasonic welding of metallic materials and plastics;
- diffusion welding of different materials;
- magnetic-pulse welding and treatment;
- surfacing and surface modification;
- spot welding and riveting of metallic materials and plastics by friction.

Prof. N. Huber delivered a welcome address to the Conference participants on behalf of the Institute of Metals Research (GRSS subdivision). He briefly described GRSS structure and the main directions of the Institute's activity. The GRSS has a staff of 741 persons, the company funding, mainly from federal budget, amounting to EUR 72.4 mln per year.

The activity of the Institute is aimed at studying such materials as magnesium, aluminium and titanium, designing new structures, coating and surface modification processes, making permanent joints by solid phase and laser welding, as well as using them to develop new materials, which can be competitive in aircraft construction and automotive industry.

Prof. W. Schweigert spoke on behalf of DVS. He highly appreciated GRSS achievements in the field of material studies, development of technologies and ensuring fruitful activity for the participants of the conducted scientific conference.

On behalf of the Conference organizers Dr. J.F. dos Santos invited all those present to take part in two seminars that are planned to be conducted next year: in April 2007 on spot friction welding and spot friction stir welding, as well as in November on friction stir welding.

23 papers were presented during the two work days, and the latest achievements were demonstrated in the field of welding, surface modification and in other related processes where friction heating is used.

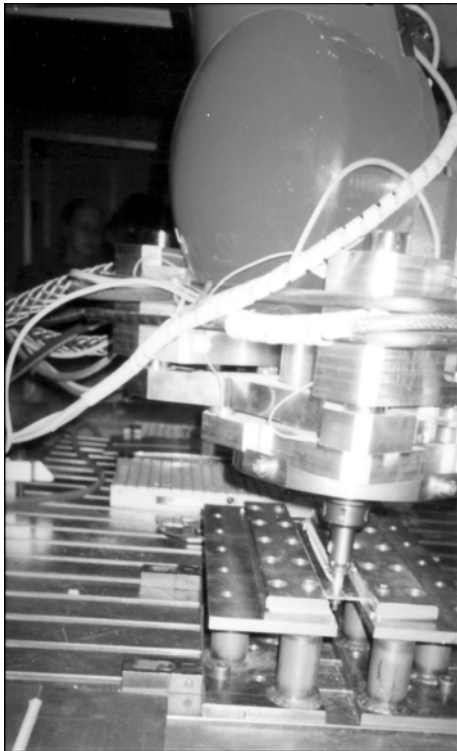


Figure 1. TriceptTR805 robot and bobbin tool



Figure 2. Installation (a) and process (b) for surface treatment and surfacing by friction



The greatest interest was created by demonstration of friction stir welding of sheet blanks from aluminum alloy 2024 using TriceptTR805 robot and bobbin tool (Figure 1), of surface treatment and surfacing by friction (Figure 2), as well as the use of friction hydro pillar processing (Figure 3) for repair applications, which allows filling the defective sections with metal without melting the blank metal. New technology of polymer materials joining with application of friction, so called friction riveting, was also demonstrated.

The most interesting of the papers presented at the Conference were the following:

New Joining Techniques with Utilization of Dimensional Effects (J. Wilden et al.); Friction Stir Welding of Aluminum Die Castings (Sh. Sheikhi et al.); High-Dynamic Process of Collision in Magnetic-Pulse Welding (E. Uhlmann et al.); Precision Friction Welding and its New Applications (H. Goldau, Ch. Behrend); High-Speed Friction Welding of Metal Joints (F. Luidhardt); Friction Surfacing of Metallic Materials --- Process and Application (M. Bayer, J.F. dos Santos); Friction Welding of Cast Iron with Spherical Graphite (W. Hauke); Friction Spot Welding of Aluminum Alloys (H. Knoll et al.); Contribution to Development of a New Method of Joining Plastics and Light Alloys (S. Amancio et al.); Strategy of Improving the Functionality of Parts by Diffusion Welding (J. Wilden et al.).



Figure 3. Friction Hydro Pillar Processing

More detailed information on the Conference «Welding Days 2006» is available in PWI library.

Dr. N.G. Tretyak, PWI

ALL RUSSIAN SCIENTIFIC AND ENGINEERING CONFERENCE «RAPIDLY-QUENCHED MATERIALS AND COATINGS»



The 5th All Russian Scientific and Engineering Conference «Rapidly-Quenched Materials and Coatings» with international participation, organized by the Federal Agency on Education, OJSC «Moscow Committee on Science and Technology», and the K.E. Tsiolkovsky Russian State University of Technology MATI, was held on December 12–13, 2006 at MATI.

Jubilee scientific and engineering seminar «Diffusion Welding and its Role in Modern Engineering», dedicated to the centenary of the birth of Prof. Nikolaj F. Kazakov, Doctor of Sci. (Eng.), famous Russian inventor and scientist, Lenin Prize laureate, honored inventor of USSR, honored worker of science and engineering of RSFSR, founder of diffusion welding, was held in the framework of the Conference.

About 70 specialists from the Russian Federation and Ukraine took part in the work of the Conference. More than 40 presentations in the following fields were made at the Conference: diffusion welding, rapidly-quenched materials, methods of deposition and investigation of coatings, beam and ion-plasma methods of surface modification. Proceedings were published by the start of the Conference (Moscow: MATI, 423 pp.), which presented the materials of 75 papers of specialists in the research areas discussed at the Conference.

The papers by Prof. G.V. Konyushkov, Dr. of Sci. Eng. (SSTU, Saratov) and V.V. Peshkov (VSTU, Voronezh) on the role of diffusion welding in modern engineering, were made in the plenary session. Prof. V.V. Sleptsov, Dr. of Sci. (Eng.) (MATI, Moscow) and V.V. Kudinov also addressed the plenary session, speaking about ion-plasma technologies of surface nanostructuring and strengthening of composite materials treated by low-temperature plasma. When the plenary session was over, the participants of the



seminar visited the cemetery and laid flowers to N.F. Kazakov monument.

Papers and information by Prof. V.V. Kvasnitsky, Dr. of Sci. (Eng.) (NUK, Nikolaev), M.V. Bolshakov (NU «Lvivska Politekhnik», Lvov), Prof. O.A. Barabanova, Dr. of Sci. (Eng.) (MATI, Moscow), Prof. G.K. Kharchenko, Dr. of Sci. (Eng.) (PWI, Kiev), Prof. S.D. Shlepin, Dr. of Sci. (Eng.) (MATI, Moscow) and other specialists on welding and allied technologies were presented in the next sessions of the seminar. In addition to oral presentations, also poster papers were presented during the seminar.

Two papers that showed the efficiency and expediency of diffusion welding application should be specially noted.

The paper by S.D. Shlyapin and K.S. Senkevich (MATI, Moscow) «Producing Porous Items for Medical Purposes by Applying Diffusion Welding», described production of porous endoprostheses for human vertebrae from titanium wire of VT-1-0 grade. The possibility is shown of diffusion welding application for manufacturing a porous endoprosthesis, which is a structure in the form of a spiral wound

from a single piece of titanium wire, welded layer by layer.

The efficiency of diffusion welding application when manufacturing special electrodes for resistance welding of rocket and space engineering products was shown in the paper by G.A. Menshikov (MATI, Moscow) on «Diffusion Welding and its Role in Increasing the Efficiency of Resistance Welding». It is shown that in welding parts of unequal thicknesses from light alloys, an improvement of electrode working part wear resistance is achieved by applying diffusion welding at reinforcement of electrode surface by molybdenum net or Al_2O_3 whisker threads. Application of such welding electrodes for resistance spot welding increases the efficiency several times.

Interesting work was reported in the session «Methods of Coating Deposition and Investigation». Microarc oxidation technologies, plasma spraying, air ion-plasma and arc treatment, chemico-thermal and electromechanical treatment of different material surfaces were considered.

Prof. G.K. Kharchenko, PWI



OUR CONGRATULATIONS

The staff of the E.O. Paton Electric Welding Institute of NASU, Editorial Board and staff of «Автоматическая Сварка» journal are extending the heartiest congratulations to PWI leading staff members Oleg K. Nazarenko, Volodymyr M. Nesterenkov,

Vasyl V. Gumovsky, Victor V. Galushka, Volodymyr O. Troitsky, Anatoly Ya. Nedoseka, Vyacheslav A. Pivtorak on receiving the State Prize of Ukraine in the field of Science and Technology for 2006



Left to right: V.M. Nesterenkov, O.K. Nazarenko, V.V. Gumovsky, V.V. Galushka



Left to right: V.A. Pivtorak, V.O. Troitsky, A.Ya. Nedoseka, L.N. Devin

DECREE OF THE PRESIDENT OF UKRAINE

on Awarding the State Prizes of Ukraine
in the field of science and technology in 2006

Based on application by the Committee for State Prizes of Ukraine in the field
of science and technology, I hereby decree:

1. To award the State Prizes of Ukraine in the field of science and technology in the 2006:

– for the development of innovative model-oriented control based electron beam welding units to:
NAZARENKO Oleg K. – Corresponding Member of the National Academy of Sciences of Ukraine, Head of Department at the E.O. Paton Electric Welding Institute of the NAS of Ukraine
NESTERENKOV Volodymyr M. – Doctor of Technical Sciences, Deputy Head of Department at the E.O. Paton Electric Welding Institute of the NAS of Ukraine
GUMOVSKY Vasyl V. – Leading Engineer of the E.O. Paton Electric Welding Institute of the NAS of Ukraine
GALUSHKA Viktor V. – Leading Electronic Engineer of the E.O. Paton Electric Welding Institute of the NAS of Ukraine;

– for the development and application of means and technologies for non-destructive testing and technical diagnostics of durable machine-building and oil-and-gas equipment to:
TROITSKY Volodymyr O. – Doctor of Technical Sciences, Head of Department at the E.O. Paton Electric Welding Institute of the NAS of Ukraine
NEDOSEKA Anatoly Ya. – Doctor of Technical Sciences, Head of Department at the E.O. Paton Electric Welding Institute of the NAS of Ukraine
PIVTORAK Vyacheslav A. – Candidate of Physical-Mathematical Sciences, Leading Staff Scientist of the E.O. Paton Electric Welding Institute of the NAS of Ukraine

President of Ukraine
Kyiv, 20 December 2006
№ 1103/2006

V. YUSHCHENKO